

DEPARTMENT OF MECHANICAL AND AEROSPACE ENGINEERING

# Panel-Method Aerodynamic Simulation and Thermal Analysis

---

A Low Fidelity Model for Aerodynamics and Aerothermodynamics from Subsonic to Hypersonic Regimes

BEN PARSONAGE

MORRIS KELLY

EUAN KERR

Supervisors: Dr M Fossati, Dr E Minisci

2018

Project website: <https://pastastrath.wordpress.com/>

Group E



## Abstract

The concept feasibility and preliminary design phases during the development of a reusable space access vehicle are largely dependent on accurate aerodynamic and aerothermodynamic simulation. Numerous high and low fidelity simulation methods exist, but all contain significant caveats including, but not limited to, prohibitive computational cost, restricted access and limited usability.

This report details the development of PASTA (Panel method Aerodynamic Simulation and Thermal Analysis), a low fidelity, open source, aerodynamic and aerothermodynamic simulation tool, designed to allow accurate, computationally inexpensive and accessible estimation of aerodynamic and aerothermodynamic characteristics of any predefined geometry during subsonic, supersonic or hypersonic flight.

PASTA has been validated against DSMC, CFD, experimental data, flight data and alternative low-fidelity simulation results.

PASTA has been shown to offer a good degree of accuracy for supersonic and hypersonic flow conditions over a distinct geometric profile.

## Acknowledgements

The authors would like to thank Dr Marco Fossati and Dr Edmondo Minisci of the Mechanical and Aerospace Engineering Department, University of Strathclyde, for their continued support and advice throughout the duration of this project.

The authors would additionally like to thank their family and friends who have consistently delivered unequivocal support, and demonstrated prodigious perseverance.

# PANEL METHOD AERODYNAMIC SIMULATION AND THERMAL ANALYSIS

BEN PARSONAGE

MORRIS KELLY

EUAN KERR

[blank]

## Contents

|  |    |
|--|----|
| Abstract.....                                | i  |
| Acknowledgements.....                        | i  |
| Nomenclature .....                           | v  |
| 1 Introduction .....                         | 1  |
| 1.1 Background .....                         | 1  |
| 1.2 Motivation.....                          | 2  |
| 1.3 Management.....                          | 4  |
| 1.3.1 Initial Project Specification .....    | 4  |
| 1.3.2 Team Structure .....                   | 6  |
| 1.3.3 Project Schedule .....                 | 7  |
| 1.3.4 Resources .....                        | 7  |
| 1.3.5 Progress Management.....               | 8  |
| 1.3.6 Risk Assessment .....                  | 9  |
| 2 Background .....                           | 14 |
| 2.1 Space Access Vehicles .....              | 14 |
| 2.1.1 History.....                           | 14 |
| 2.1.2 Current development.....               | 16 |
| 2.2 Simulation Methods.....                  | 18 |
| 2.2.1 Wind Tunnel.....                       | 18 |
| 2.2.2 Computational Fluid Dynamics .....     | 18 |
| 2.2.3 Direct Simulation Monte Carlo .....    | 19 |
| 2.2.4 Hybrid DSMC/CFD .....                  | 20 |
| 2.2.5 Local Surface Inclination Methods..... | 20 |
| 2.3 Existing Simulation Software .....       | 22 |
| 2.3.1 ORSAT.....                             | 22 |
| 2.3.2 DRAMA.....                             | 24 |
| 2.3.3 SCARAB.....                            | 24 |
| 2.3.4 FOSTRAD .....                          | 26 |
| 2.3.5 X-FOIL.....                            | 27 |
| 2.3.6 APAME .....                            | 27 |
| 3 Code Structure .....                       | 28 |
| 3.1 Language and development.....            | 28 |
| 3.2 Description.....                         | 29 |
| 3.3 Performance .....                        | 30 |
| 4 Input Module .....                         | 32 |

|        |   |    |
|--------|---|----|
| 5      | Atmosphere Module .....                       | 33 |
| 5.1    | Introduction.....                             | 33 |
| 5.2    | US 1976 .....                                 | 34 |
| 5.3    | NRLMSISE-00 .....                             | 34 |
| 5.4    | Comparison between US76 and NRLMSISE-00 ..... | 35 |
| 6      | Geometry Module .....                         | 40 |
| 6.1    | Reading.....                                  | 40 |
| 6.1.1  | ASCII Support.....                            | 41 |
| 6.1.2  | Binary Support.....                           | 41 |
| 6.1.3  | Geometry Calculations .....                   | 42 |
| 6.2    | Back-Face Culling/Hidden Surface Removal..... | 42 |
| 6.2.1  | Front-end culling .....                       | 43 |
| 6.2.2  | Ray tracer .....                              | 44 |
| 6.2.3  | Results .....                                 | 47 |
| 7      | Hypersonic Module .....                       | 48 |
| 7.1    | Aerodynamics.....                             | 48 |
| 7.1.1  | Continuum.....                                | 48 |
| 7.1.2  | Free-Molecular .....                          | 49 |
| 7.1.3  | Transitional.....                             | 50 |
| 7.2    | Aerothermodynamics.....                       | 51 |
| 7.2.1  | Continuum.....                                | 51 |
| 7.2.2  | Free-Molecular .....                          | 52 |
| 7.2.3  | Transitional.....                             | 52 |
| 8      | Supersonic Module.....                        | 53 |
| 8.1    | Aerodynamics.....                             | 53 |
| 9      | Sub-Sonic Module.....                         | 57 |
| 9.1    | Aerodynamics.....                             | 57 |
| 10     | Output Module.....                            | 62 |
| 11     | Validation .....                              | 63 |
| 11.1   | Hypersonic.....                               | 63 |
| 11.1.1 | Aerodynamics.....                             | 63 |
| 11.1.2 | Aerothermodynamics.....                       | 71 |
| 11.2   | Supersonic .....                              | 75 |
| 12     | Applications .....                            | 78 |
| 12.1   | CFASTT-1.....                                 | 78 |
| 13     | Release Distribution .....                    | 82 |

|        |                               |    |
|--------|-------------------------------|----|
| 14     | Conclusions .....             | 82 |
| 14.1   | Summary .....                 | 82 |
| 14.2   | Discussion.....               | 83 |
| 14.3   | Future work.....              | 85 |
| 14.3.1 | Subsonic Implementation ..... | 86 |
| 15     | References .....              | 91 |

## Nomenclature

| Symbol       | Explanation                        | Units           | Subscripts |                               |
|--------------|------------------------------------|-----------------|------------|-------------------------------|
| $\nabla$     | Gradient                           | -               | $O$        | Total (Pressure, Temperature) |
| $A$          | Area                               | $m^2$           | $1,2$      | Upstream/Downstream           |
| $C$          | Force Coefficient                  | -               | $\infty$   | Free Stream                   |
| $c$          | Speed of Sound                     | $m/s$           | $cont$     | Continuum                     |
| $Kn$         | Knudsen Number                     | -               | $cp$       | Collocation Point             |
| $M$          | Mach Number                        | -               | $D$        | Drag                          |
| $\mathbf{n}$ | Normal Vector                      | -               | $fm$       | Free Molecular                |
| $P$          | Pressure                           | $Pa$ or $N/m^2$ | $i$        | Influenced Point              |
| $Q$          | Heat Transfer flux                 | $W/m^2$         | $in$       | Internal                      |
| $\dot{Q}$    | Heat Transfer Rate                 | $W$             | $j$        | Influencing Point             |
| $R$          | Universal Gas Constant             | $J/kgK$         | $L$        | Lift                          |
| $Re$         | Reynolds Number                    | -               | $N$        | Normal                        |
| $S$          | Reference Area                     | $m^2$           | $ref$      | Reference                     |
| $St$         | Stanton Number                     | -               | $S$        | Side                          |
| $t$          | Time                               | $s$             | $T$        | Tangential                    |
| $T$          | Temperature                        | $K$ or $C$      | $trans$    | Transitional                  |
| $v$          | Velocity                           | $m/s$           | $w$        | Wall                          |
| $\mathbf{v}$ | Velocity Vector                    | $m/s$           | $\tau$     | Shear                         |
| $\alpha$     | Angle of Attack                    | degrees         |            |                               |
| $\beta$      | Shock Wave angle                   | degrees         |            |                               |
| $\gamma$     | Ratio of Specific Heats            | -               |            |                               |
| $\delta$     | Panel Inclination                  | degrees         |            |                               |
| $\vartheta$  | Angle                              | degrees         |            |                               |
| $\mu$        | Dynamic Viscosity                  | $Ns/m^2$        |            |                               |
| $\rho$       | Density                            | $kg/m^3$        |            |                               |
| $\sigma$     | Momentum Accommodation Coefficient | -               |            |                               |
| $\psi$       | Angle of Yaw                       | degrees         |            |                               |

# **PANEL METHOD AERODYNAMIC SIMULATION AND THERMAL ANALYSIS**

BEN PARSONAGE

MORRIS KELLY

EUAN KERR



# 1 Introduction

## 1.1 Background

Global space industry is on the cusp of a revolution. For the first time since the ‘Space Race’ of the mid 1900s, global industry (now including private companies in addition to government organisations) are competing to secure their share of a new space age of technological and economic development, to be realised by the inevitable emergence of low cost space access.

Space access has long been hindered by the exceptionally high launch costs, between \$20,000 and \$30,000 per kilogram of payload for conventional vertical expendable launch vehicles (ELVs). One concept for reducing this cost, pioneered by private companies such as SpaceX, Virgin Galactic and reaction engines, is the use of Reusable Launch Vehicles (RLVs).

There are numerous benefits of RLV use. The primary incentives include the significantly reduced launch costs, due to the reduced mass of fuel used and the recovery of integral vehicle components, and the relatively quick turnover times between launches. Additional benefits stem from the expansion of the space sector into new markets, such as space tourism and dedicated small payload deployment, to meet increasing demand from space derived services (telecommunications, navigation, remote-sensing, weather etc).

Notable examples of this new emergence of RLV technology include the ‘Falcon’ series of vertically launched rockets produced by SpaceX. Founded by Elon Musk, SpaceX currently operates government and commercial contracts to deliver payload to Low Earth Orbit (LEO), including resupply missions to the ISS. SpaceX offers a greatly reduced launch cost per kilogram by autonomously landing the 1<sup>st</sup> stage rocket boosters used during launch. These boosters are then subject to a brief period of maintenance and inspection, before being cleared for reuse. The ultimate goal, envisioned by Musk, is to achieve launch costs of “\$500 per pound (\$1,100/kg) or less”.

Another example demonstrates the applicability of RLV technology to expand the commercial space market through the introduction of ‘Space Tourism’. Virgin Galactic, founded by entrepreneur Richard Branson, offers to carry human passengers and/or science missions on air launched, sub-orbital trajectories as early as 2018. This goal has prompted the development of numerous other commercially driven spacecraft ventures, intent on securing portions of this new market.

One concept attracting increasing international commitment and research is the fully reusable Spaceplane. A spaceplane is defined as a lifting body space access vehicle capable of launching horizontally, accelerating to orbital velocities and altitudes, performing controlled re-entry into the Earth's atmosphere and completing a return flight as a conventional aircraft, to land at a designated landing site.

Examples of development in this field include British based Reaction Engines, who recently completed an integral SABRE engine test for their spaceplane concept, Skylon, discussed further in *section 2.1.2*.

To support the increasing incentive to develop RLVs, new methods of concept design, analysis and evaluation are required. By nature, the concept of reusable launch vehicles requires a significant departure from traditional space access technology. Inclusion of a low speed, low altitude flight configuration, non-ablation based thermal protection systems and single stage to orbit (SSTO) operational constraints will inevitably result in a new breed of hypersonic aircraft to pioneer this emergence of a new space age.

## 1.2 Motivation

A critical aspect of launch vehicle design, is the correct estimation of the aerodynamic and aerothermodynamic conditions likely to be encountered during nominal and abort trajectories. This activity forms a significant part of the preliminary design phase and concept evaluation phase of any hypersonic vehicle, as well as the more detailed design specification stages. However, these simulations can prove to be very impractical, and difficult to achieve.

Aerodynamic and aerothermodynamic simulation can be an extremely complicated process for a number of reasons. The interaction between an inviscid flow field, downstream of a shockwave, and a viscous boundary layer attached to the wall of the vehicle, the need for a non-ideal gas atmospheric representation, and difficulties handling the uncertainty within the transitional flow regime (where the flow field can no longer be considered as a continuous material, not can the particulate nature of the gas be neglected), all contribute to this complexity. However, one of the most difficult aspects of aerodynamic/aerothermodynamic is the large computational time required by most modern applications.

High fidelity simulations, such as Direct Simulation Monte Carlo (DSMC) and Computational Fluid Dynamics (CFD), can accurately simulate complex flow characteristics, and as such

represent a valuable tool necessary for the development of any hypersonic capable vehicle. However, the computational cost associated with these techniques, often ranging from hours to days for just one single point along a vehicles trajectory, can often render them completely impractical for the preliminary design stage of vehicle development.

The problem, therefore, is to achieve an acceptable level of fidelity for use in a preliminary design stage, while maintaining a non-prohibitive computational cost.

Several programs currently exist that fit this description (described in *section 2.3*). However, all contain significant caveats that could cause practical difficulty. For example, the majority are not open-source, or freely available. Therefore, the source code cannot be inspected, and mathematical operations/implementations cannot be checked, evaluated or altered. This can cause results to be very difficult to validate or compare. Secondly, many of these programs are useable only for specific problems, such as a certain flow regime, or a specific geometry.

The aims of this project can therefore be summarised:

- Develop a low fidelity computational program to evaluate the coefficients of Lift, Drag and Moment, and the distributions of Pressure coefficient, Heat Transfer coefficient and Total Heat Transfer acting on a user specified geometry, within the sub-sonic, supersonic and hypersonic regimes.
- Operate in a universal programming language, such as Python or C++, allowing for free public access.
- Allow the upload of any standard 3D geometry STL file.
- Evaluate the specified coefficients at a significantly lower computational cost to that of any existing higher fidelity simulation.
- Validate against existing high-fidelity simulations to ensure maximum retainable accuracy.
- Distribute all source codes and documentation via a file sharing repository, such as GitHub.
- Compatible with, at minimum, Windows and Linux operating systems.

### 1.3 Management

To effectively achieve these aims, numerous project management strategies were implemented. This section details the extent of the project management included during the completion of this project.

The project team was selected by the Mechanical and Aerospace Engineering (MAE) department of the University of Strathclyde, based on an availability directory compiled by the ME525 course directors.

The project was supervised by Dr Marco Fossati and Dr Edmondo Minisci of the MAE department, assuming the responsibilities of the ‘stakeholders’ of the project. Dr Fossati acted as the primary contact for all matters regarding the completion of the project. Dr Minisci acted as a technical advisor, due to his past experience in developing the Free Open Source Tool for Reentry of Asteroids and Debris (FOSTRAD), a low fidelity, local surface inclination based program, which would provide the basis for this projects development.

#### 1.3.1 Initial Project Specification

A formal ‘kick-off’ meeting was held with the project team and all stakeholders in October 2017. This meeting formally summarised the aims and requirements of the project, including the set of deliverables expected by the stakeholders, and the suggested meeting schedule to span the length of the project from commencement to completion. Additionally, the required initial resources required by the team were discussed, and it was agreed to allow the team full access to an operational version of the FOSTRAD code, presented within the MATLAB programming environment.

The project deliverables, including set completion dates and additional requirements as decided in the initial ‘kick-off’ meeting, are summarised in *table 1*.

| Deliverable           | Completion Date | Requirements   |
|-----------------------|-----------------|--|
| Interim report        | 17.11.17        | Submitted in both paper and electronic formats, detailing the complete structure and progress of the work at the time of submission, in no more than 20 pages. |
| Interim presentation  | 8.1.18          | Maximum 10 minutes, covering the content of the Interim report, followed by 15 minutes of questions.   |
| Final report          | 23.3.18         | Submitted in both paper and electronic formats.  |
| Final presentation    | 20.4.18         | Maximum 25 minutes, covering the entire project workflow and outcome(s), followed by 35 minutes of questions.  |
| Completed program     | 20.4.18         | The completed program is required to adequately meet the project aims as stated in <i>section 1.2</i> .  |
| Program documentation | 20.4.18         | Present clear steps for the use of the final program. All documentation and source code is to be distributed via a file sharing repository, such as GitHub.    |
| Project Website       | 23.3.18         | Present a clear summary of the project, split into meaningful subsections.   |

*Table 1 - Project deliverables*

On the conclusion of the initial ‘kick-off’ meeting, the full scope of the project, including all deliverables and requirements of the new program, was set out in the Statement of Purpose by the project team. This document was signed by all active team members and stakeholders of the project and submitted to the MAE department on 13th October 2017.

### 1.3.2 Team Structure

Within the Statement of Work, the respective roles within the project team were discussed and allocated, based upon the personality traits of each team member [1]. The team structure was decided as follows:

- **PROJECT MANAGER**

Morris Kelly was chosen to assume full responsibility of the workload management throughout the completion of the work defined in the Statement of Work. Additionally, Morris was chosen to be responsible for the development of all aspects of the developed program relating to supersonic flow, and the final release distribution, including separate program versions for use with Linux operating systems.

Morris was seen to be ideally suited to assume these responsibilities, due to previous experience managing group projects, including the design and construction of a model aircraft in 2014, and previous experience with programming in MATLAB and mathematical modelling, including the simulation of the SABRE supersonic engine in 2016

- **TECHNICAL SUPERVISOR**

Ben Parsonage was allocated the role of technical supervisor, which included creating the overall program framework, developing the hypersonic section, integrating the additional sections completed by the remaining team members, and dealing with the Windows release of the program. Ben also assumed responsibility of all 'master' copies of documents and source code, including backups, and ensured the effective distribution to the team as required. This was achieved primarily using online filesharing systems.

Ben was chosen for these responsibilities due to his level of prior experience with coding. This allowed Ben to immediately begin developing the program framework on the commencement of the project, to be ready for efficient and timely integration of the remaining team members' contributions into the overall framework. Ben had proved himself to be organised, and able to manage group settings for other project and class work.

#### - RESEARCHER

Euan Kerr took the role of researcher within the project, responsible for all aspect of the code relating to subsonic aerodynamic simulation, as well as any other tasks required during the project at the discretion of the project manager.

Euan had little previous experience with code development and structuring, but a large past experience of aerodynamics that could be applied to a subsonic flow on a body as necessary.

### 1.3.3 Project Schedule

Within the Statement of Purpose was an agreed meeting schedule for the entire duration of the project. Each meeting involved a short progress report from each team member to the project stakeholders and could include the opportunity for questions and concerns to be raised by all parties present.

Meetings were set on a bi-weekly basis throughout the duration of the project, with additional meetings as required during the run up to milestones.

Project milestones were defined as the individual deliverables, specified in *table 1*, and were 'hard set' deadlines with no slack.

### 1.3.4 Resources

The primary resource to be spent during the completion of this project was time. The project specification allowed for approximately 400 hours of effort per person to be allocated throughout the project. With the project running for 23 weeks from beginning to end, an average of 20 hours per week per person of effort was expected, subject to numerous risks, discussed in *section 1.3.6*.

In terms of finances, a £100 budget was available for each member of the team to spend if necessary. However, due to the largely computer based requirement of the work, this budget was never largely utilised. The extent of the project expenditure is encapsulated in the website hosting price of £36 for a year.

### 1.3.5 Progress Management

The initial means of project scheduling was the use of Microsoft Project, on which a department run workshop was held before the allocation of projects. Whilst in industry, this is a standard method for controlling a project, it was found to be overcomplicated with respect to the team's requirements, and as such was replaced with a Gantt chart, and GitHub based project management system.

The initial Gantt chart (*figure 3a*) was compiled and updated with less frequency, but regularly referred to, ensuring that the project was on track. The initial Gantt chart represented a high-level overview of the project sub-sections due for completion. If tasks were found to have slipped behind the planned schedule, they would be compensated for either with extra work or modifications to the Gantt chart as the project progressed. The final iteration of the project Gantt chart is shown in *figure 3b*.

The purpose of GitHub is to facilitate software development as easily as possible. Therefore, the GitHub project management environment was chosen to be the primary method of progress management due to the software based nature of the required work. The management section of the team's area within the supervisor's GitHub repository was populated with more detailed sub-tasks related to each primary task listed in the Gantt chart. Sub-tasks were in turn marked as completed when necessary, allowing for accurate progress visualisation available to all team members and stakeholders.

In addition to the online record of completed work, each team member kept a log book of their work and all meetings. This would ensure that all notes and work would be available as a hard paper copy should anything happen to the online services. These logbooks also formed the basis of the creation of the final report.

The 'critical path', the fundamental summary of the workflow at a non-flexible, chronological, task-based level, could be determined from the Gantt chart and listed milestones. The project 'critical path', showing the limiting factors on project completion, is shown in *figure 1*. With this path defined, the importance Gantt chart accuracy was clear.

Any unlisted subtasks were treated as flexible, with potential for 'slack time', and could be completed according to the schedules of the team members.



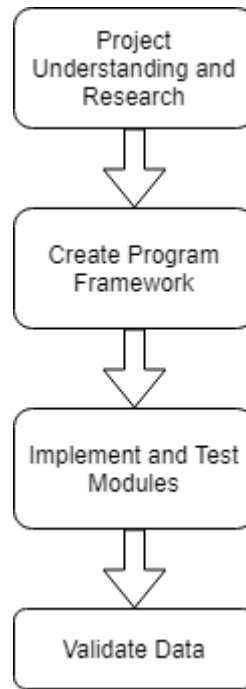


Figure 1 - Project Critical Path

### 1.3.6 Risk Assessment

Prior to beginning work on the project, steps were taken to first identify potential risks and their effect on the project. With these in mind, mitigation was planned, to be used if necessary should the potential risk materialise during the completion of the project.

The process for risk management is shown in *figure 2*. [2]

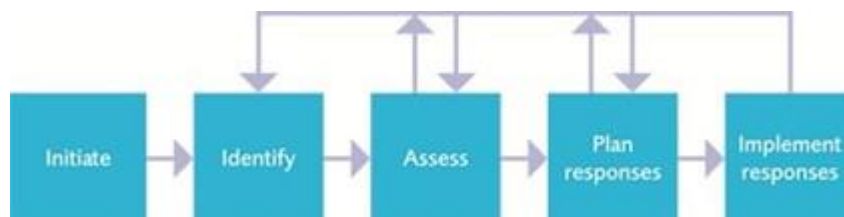


Figure 2 - Risk Analysis Process

The identified risks are listed below. Steps for risk mitigation and neutralisation are included for each identified risk.

### **1. Loss of Data**

With the project being largely computational, the risk of losing work due to machine failure, or human error, was considered to be of extreme importance. This was mitigated using an online filesharing system, ensuring that backup copies for each important document or directory. While the impact would be large, the likelihood of a complete loss of work was therefore negligible.

### **2. Loss of Man Hours**

The project was completed alongside numerous other commitments to separate classes. There was therefore a risk that progress could be impacted by additional end of term assessments required from each team member. This had the potential to be a significant problem. Therefore, appropriate planning was carried out to ensure certain sub-tasks were completed by certain dates, and that workload was effectively shared amongst the team members, especially during busy periods. Where this strategy failed, extra work was scheduled over the Christmas break to compensate for progress lost prior to the semester 1 examinations.

### **3. Incomplete or Inaccurate Results**

The work potentially could not be delivered as a complete, accurate, fully verified program. This would be mitigated by validating the program piece by piece to ensure functionality as intended. This would reduce the possibility of programming 'bugs' and ensure a more complete, accurate code.

### **4. Differences of Opinion**

Prior to the commencement of the project, the three allocated team members had no experience working with each other. There was therefore a concern that differences of opinion and strong personalities may affect the progress of the group when decisions had to be made regarding the direction in which to take the project. Due to the group size, it was initially assumed that almost all aspects could be voted on democratically, should there not be an academic argument for one method over another. Ultimately, this was reasonably successful, with early decisions being made as a group, but fell apart towards the later stages of the project as the group became slightly fragmented.

## **5. Communication Breakdown**

The final risk, potentially following on from the previous concern, was the possibility that the group would fall apart during the completion of the project and thus fail to generate the required deliverables. This risk was mitigated by ensuring constant communication lines within the group. I.e. regular progress updates and discussion of each weekly schedule of sub-tasks, up to date and accessible file-sharing, research area suggestions and general workflow advice. However, this risk was ultimately realised, as one member of the project team failed to satisfactorily complete their section of the project. This is further discussed in *section 14.2*.

# PANEL METHOD AERODYNAMIC SIMULATION AND THERMAL ANALYSIS

BEN PARSONAGE

MORRIS KELLY

EUAN KERR

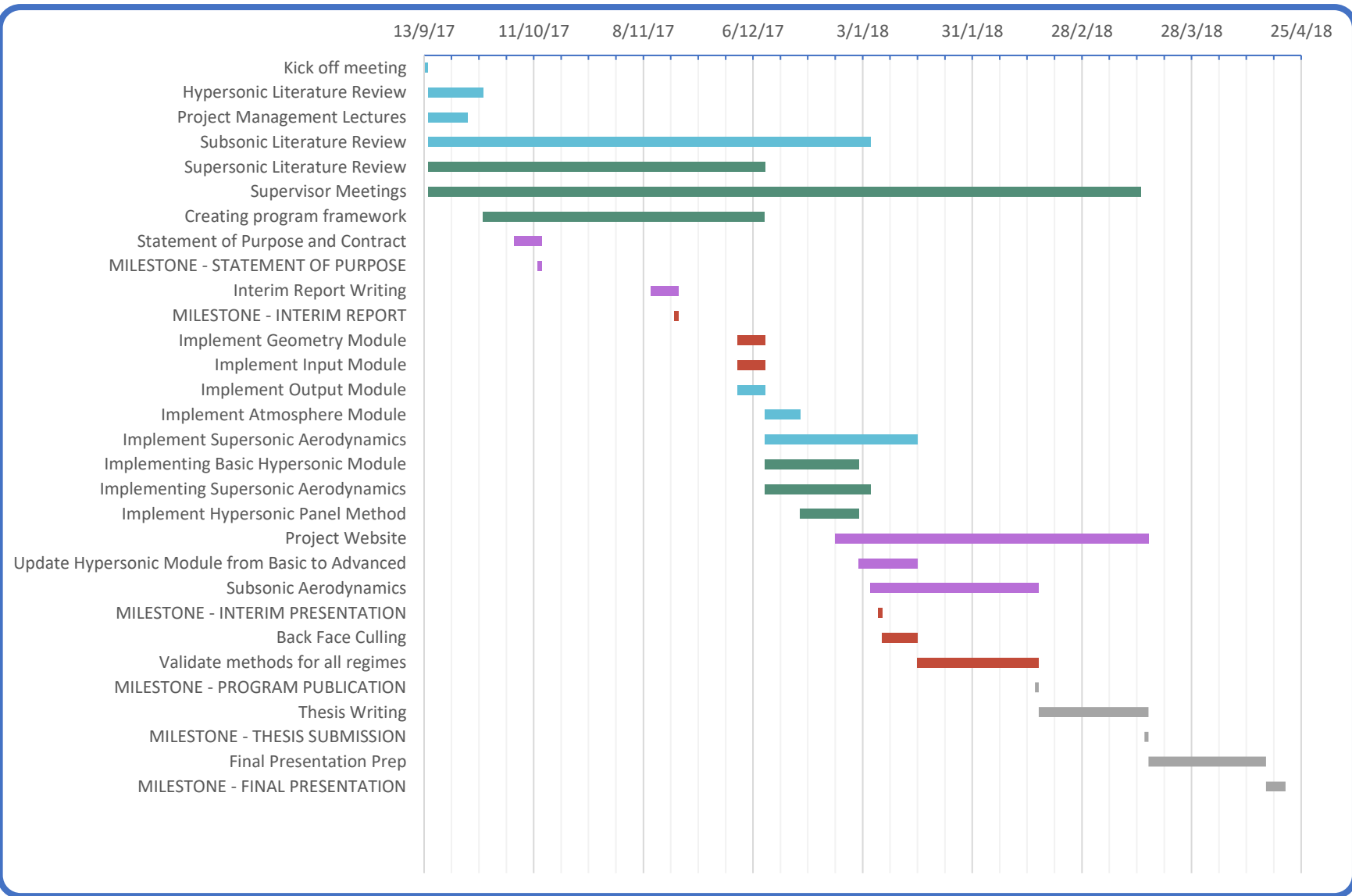


Figure 3 a – Initial Project Gantt Chart

# PANEL METHOD AERODYNAMIC SIMULATION AND THERMAL ANALYSIS

BEN PARSONAGE

MORRIS KELLY

EUAN KERR

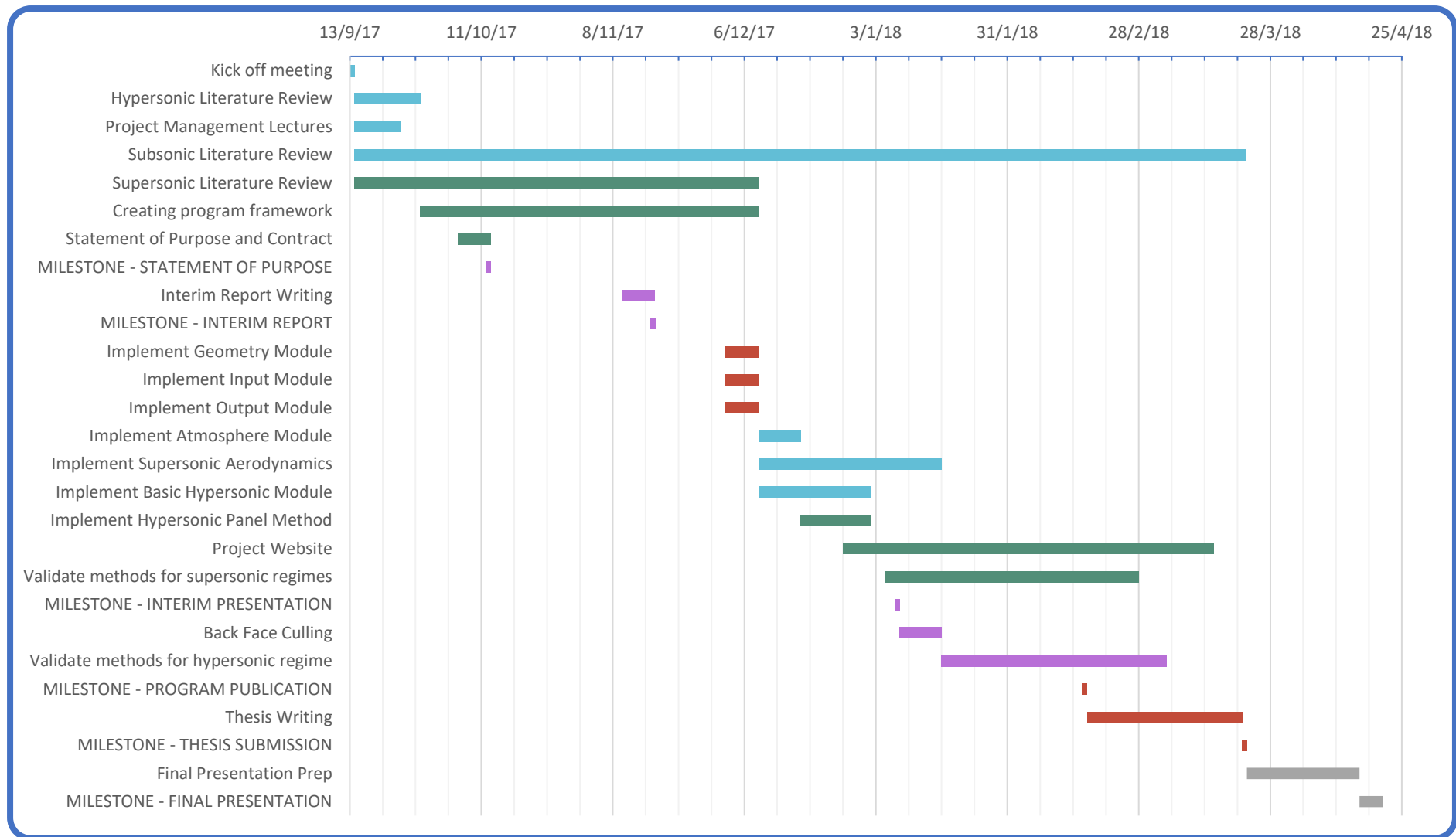


Figure 3b - Final Project Gantt Chart

## 2 Background

This section briefly describes the background to the project in terms of the historical development and current trends of high speed space access vehicles, and the supporting methods of simulation and modelling.

### 2.1 Space Access Vehicles

#### 2.1.1 History

One of the first known examples of a feasible Spaceplane design was the *Silbervogel*, envisaged by Austrian scientist Dr Eugen Sanger and his wife, mathematician Irene Bredt [3]. Sangers concept, shown in *figure 4*, was designed as a cross continental bomber, to be launched from a mountain-side sled, accelerate to near orbital velocities, and perform a series of ‘jumps’ across the surface of the atmosphere, in order to reach a desired location, before gliding back to the German launch site. The design was one of the first to advocate the use of wings for extending the flight time and range of ballistic missiles, as well as the novel inclusion of a regeneratively cooled liquid oxygen engine and a near ‘lifting body’ surface geometry, similar to that of the STS Orbiter. As such, the design is considered to be the precursor to the entire development of reusable space access vehicles.

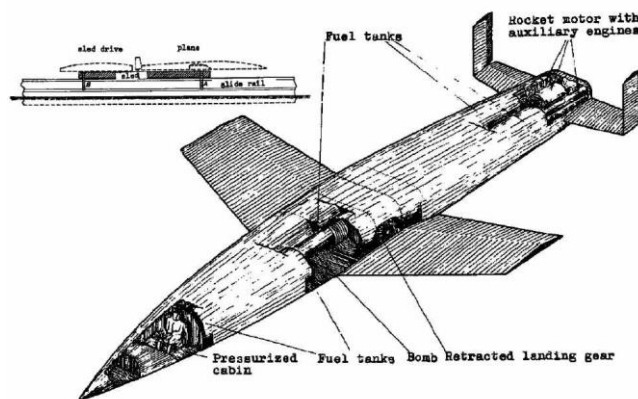


Figure 4 - *Silbervogel*

After World War II, national organisations such as the National Advisory Committee for Aeronautics (NACA) concentrated their attention on the development of supersonic aircraft. After numerous worldwide failures, the Bell X-1 became the first manned aircraft to achieve supersonic speeds in 1947. This flight, and the worldwide acclaim achieved by the NACA, heralded the commencement of the X-Plane program, a series of experimental aircraft developed by the NACA designed to expand the known limits of aerospace operations.

The X-Plane program produced many significant advancements in aerospace technology and concepts through the latter half of the 20<sup>th</sup> century. These included the North American X-15, an air launched rocket powered vehicle which became the first manned aircraft to achieve sub-orbital flight, the Boeing X20 'Dyna-Soar' concept (*figure 5*), designed to achieve orbital speeds using an expendable rocket booster before completing an unpowered atmospheric re-entry (cancelled before construction could begin) and the Martin Marietta X24 series of lifting body aircraft, which provided valuable research data used for the development of the Space Shuttle.



*Figure 5 - Artistic representation of the X20 'Dyna-Soar'*

This interest in a reusable space vehicle culminated in the 1970's with the development of the Space Transportation System (STS) as part of the NASA Space Shuttle program. The Space Shuttle was a vertically launched, partially reusable spacecraft, which completed a total of 135 missions from its introduction in 1985 to its retirement in 2011. Missions included the installation of the Hubble Space Telescope and resupply/maintenance of the International Space Station (ISS). To date, the Space Shuttle is the most successful implementation of a partially reusable spaceplane.

The success of the Space Shuttle partly re-ignited a worldwide effort to produce a fully reusable space access vehicle. Notable designs include the Rockwell X-30, also known as the National Aero-Space Plane (NASP), the British developed Horizontal Take-Off and Landing (HOTOL), the French *Hermes* concept, and the German *Sanger II*. Each design met with cancellation before any operational model could be constructed, but all provided significant technological insights into the operational constraints and development strategies when considering such projects.

### 2.1.2 Current development

Current trends in the space industry has seen further emphasis shift to the need for the affordable space access offered by RLVs .

Continuing from the British HOTOL development from the 1990's, Oxfordshire based Reaction Engines are currently developing a single stage to orbit (SSTO) lifting body space access vehicle known as Skylon. Skylon utilises a novel hybrid air-breathing/rocket propulsion integrated engine system, SABRE (Synergetic Air-Breathing Rocket Engine). Currently predicted to commence unmanned flight testing by 2025, Skylon is hoped to be capable of 200 flights per vehicle, with only two days designated for inspection and maintenance between flights.



Figure 6 - Left to right: CFASTT-1, Skylon, STS Orbiter

In 2004, the Ansari X-Prize was awarded to Mojave Aerospace Ventures for the development of *SpaceShipOne*, which successfully completed two sub orbital flight within two weeks, prompting the future involvement of international entrepreneur Richard Branson, and the development of Virgin Galactic. As previously mentioned in *section 1.1*, Virgin Galactic aims to offer commercial access to space for paying customers, either for tourism or dedicated science missions. The flagship of Virgin Galactic is currently known as *SpaceShipTwo*, a continuation of the previous successfully flown concept. *SpaceShipTwo* is air launched by a carrier aircraft, *WhiteKnightTwo*.





*Figure 7 - SpaceShipTwo supported by White Knight Two*

*Dreamchaser* is an unmanned ISS resupply vehicle under development by Sierra-Nevada Corporation (SNC) Space Systems. Designed to be launched vertically on a liquid fuelled rocket booster, *Dreamchaser* can complete atmospheric reentry and perform a traditional low speed, low altitude flight to land conventional runway.

This increasing emergence of feasible concepts, with many approaching actuality, signals the increasing need for a flexible and usable simulation tool to be used during the concept evaluation and preliminary design phases of such vehicles. Accurate simulation and estimation of aerodynamic and aerothermodynamic conditions during the early stage of a vehicles development can lead to a much more fluid design process, and effectively mitigate any serious design flaws with little risk of failure.

## 2.2 Simulation Methods

The global emergence of the computer in the 1950's and 60's allowed the development of computational simulation methods for aerospace applications. This section describes the current state of computational aerodynamic and aerothermodynamic simulations, as well as the empirical methods required to initially derive them.

### 2.2.1 Wind Tunnel

The first method for estimating aerodynamic and aerothermodynamic characteristics involved the use of wind tunnels. Wind tunnels have been in some form of practical use since the late 1800s, and formed the basis for most of the analyses performed by the Wright brothers during the development of the *Wright Flyer* [4]. Since then, Wind Tunnels have formed the initial research methods for numerous aerodynamic problems and designs, from subsonic to supersonic regimes. Wind Tunnels typically use a high-powered fan to accelerate air through a choke point, with a scaled geometric model placed further downstream. Measuring the behaviour of this scale model, in terms of lift, drag, sideslip and moment coefficients, allows the prediction of these characteristics when considering the full-scale aircraft, with the use of various non-dimensional numbers, such as the Reynolds number.

While these models are suitable for lower speeds, simulations of re-entry conditions are extremely difficult to run, due to the extreme nature of the flow conditions present during hypersonic re-entry.

### 2.2.2 Computational Fluid Dynamics

CFD is a well-developed method of simulating aerodynamic and aerothermodynamic flow characteristics by numerically solving the Navier-Stokes equations [5]:

- Continuity

$$\frac{\partial \rho}{\partial t} + \nabla \cdot (\rho \mathbf{v}) = 0 \quad (2)$$

- X – Momentum

$$\rho \frac{Du}{Dt} = \frac{\partial(\rho u)}{\partial t} + \frac{\partial(\rho u^2)}{\partial x} + \frac{\partial(\rho uv)}{\partial y} + \frac{\partial(\rho uw)}{\partial z} \quad (3a)$$

- Y – Momentum

$$\rho \frac{Dv}{Dt} = \frac{\partial(\rho v)}{\partial t} + \frac{\partial(\rho uv)}{\partial x} + \frac{\partial(\rho v^2)}{\partial y} + \frac{\partial(\rho vw)}{\partial z} \quad (3b)$$

- Z – Momentum

$$\rho \frac{Dw}{Dt} = \frac{\partial(\rho w)}{\partial t} + \frac{\partial(\rho uw)}{\partial x} + \frac{\partial(\rho vw)}{\partial y} + \frac{\partial(\rho w^2)}{\partial z} \quad (3c)$$

- Energy

$$\rho \frac{D\left(e + \frac{v^2}{2}\right)}{Dt} = \frac{\partial(E_T)}{\partial t} + \frac{\partial(uE_T)}{\partial x} + \frac{\partial(vE_T)}{\partial y} + \frac{\partial(wE_T)}{\partial z} \quad (4)$$

As the Navier-Stokes have no general analytical solution, several CFD solution techniques have been developed to allow evaluate flow characteristics at every point over a geometry. The flow is assumed to viscous at every point, and as such can provide information concerning shocks, skin friction, heat transfer, lift, drag and moment coefficients.

The Navier-Stokes equation become invalid when macroscopic average quantities can no longer be evaluated due to progressive flow rarefication. CFD is therefore generally used as the most appropriate high fidelity simulation method for continuum and low transitional flows.

### 2.2.3 Direct Simulation Monte Carlo

Developed in the 1960's, the DSMC method estimates free-molecular and high transitional aerodynamics and aerothermodynamics by simulating dilute gas flows at the molecular level [6]. Each individual gas molecule is modelled in terms of position, velocity and state throughout the duration of the simulation. The molecular model is based on the Boltzmann equation:

$$\frac{\partial f}{\partial t} = \left(\frac{\partial f}{\partial t}\right)_{force} + \left(\frac{\partial f}{\partial t}\right)_{diff} + \left(\frac{\partial f}{\partial t}\right)_{coll} \quad (1)$$

Where  $f(\mathbf{r}, \mathbf{p}, t)$  is the probability density function, dependant on the particle position vector  $\mathbf{r}$ , momentum vector  $\mathbf{p}$  and time  $t$ . The Boltzmann equation includes the effects of forces exerted on each particle by an external influence, the diffusion of particles and the forces of collisions between particles.

The simulation of each individual particle in a control volume of fluid is an extremely computationally expensive task. To mitigate this difficulty, DSMC simulates only a select number of particles in a fluid flow, each represented by a translational, rotational and

vibrational energy time dependant variable. Collisions between particles are modelled using a probabilistic approach [7].

While the Boltzmann equation is valid for all hypersonic flow regimes, the computational cost of evaluating each fluid particle becomes significantly prohibitive when considering continuum flows [8]. For this reason, the DSMC method is primarily considered the most appropriate high fidelity method for simulating free molecular and highly transitional flows, although advanced in modern parallel processing technology may allow for the expanding of its applicability [9].

#### 2.2.4 Hybrid DSMC/CFD

Hybris DSMC-CFD simulation involves bridging free molecular and continuum simulations with hybrid functions, to allow for decreased computational cost while maintaining accuracy. [10]

The most significant decisions to be made within such solver methods include the choice of distribution function of the incoming fluid particles (either the Maxwell-Boltzmann or Chapman-Enskog models), the correct determination of the interface location between rarefied and continuum flow regions, and the correct delivery of interfacial information between the DSMC and CFD solved portions. [11]

#### 2.2.5 Local Surface Inclination Methods

Local inclination methods, including most Panel methods, are based on the evaluation of the pressure coefficient for each 'panel', or 'facet' of a discretized geometry, where the pressure coefficient is only dependant on the local deflection angle of the surface (i.e. the angle between the local surface normal and the free stream velocity vector) [12].

LSI methods for aerodynamics include the well known Modified Newtonian theory (*figure 8*), proposed by Lees [12] as an update to behaviour predicted by Isaac Newton, which states that a fluid particle loses all momentum normal to the surface at the first point of contact. Additional methods are the Tangent-Wedge method (a.k.a Hypersonic wedge method), which involves the estimation of the local pressure coefficient by modelling a symmetrical wedge tangent to a given surface point in a two-dimensional flow field, and the Tangent-Cone method, based on a three-dimensional extension of the Tangent-Wedge method.

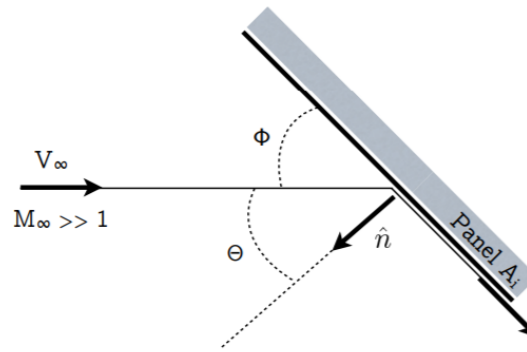


Figure 8 - Newtonian Theory for Hypersonic Flow

LSI methods can be sub-divided into two separate classes:

### 1) Object Oriented

Considers a series of individual constituent parts of a geometry, each with a simple geometric shape and assigned mass/material. Primarily used for modelling the trajectory, demise altitude or landed mass of individual components of a full spacecraft, assumed to have decomposed at a certain altitude. These methods are incapable of modelling the aerodynamics and aerothermodynamics of the entire spacecraft.

### 2) Spacecraft Orientated

Considers the entire spacecraft, modelled using either an unstructured volumetric or surface triangulated mesh. These methods can predict the aerodynamics and aerothermodynamics characteristics of any complex geometry.

## 2.3 Existing Simulation Software

### 2.3.1 ORSAT

Developed by the NASA Lyndon B. Johnson Space Centre in 1993, the Object Re-entry Survival Analysis Tool is an object orientated computational code used to simulate the survivability of satellite and upper stage components re-entering the atmosphere [13] [14]. ORSAT includes 3DOF trajectory, atmosphere, aerodynamic, aerothermodynamic and thermal/ablation modelling for various basic object shapes, in either spinning or tumbling motion, from hypersonic to subsonic speeds. A summary of the included object geometry and relative body motions is shown in *table 2*.

| Object Shape | Motion  |
|--------------|---|
| Sphere       | Spinning<br>Not spinning  |
| Cylinder     | Broadside and spinning<br>Random tumbling and spinning<br>End-on and spinning<br>End-over-end tumbling and spinning |
| Box          | Not tumbling and normal to the flow<br>Tumbling   |
| Flat Plate   | Not tumbling and normal to the flow<br>Tumbling   |

*Table 2 - ORSAT geometry and relative motion*

ORSAT calculates thermal heating parameters based on the lumped mass approach or one-dimensional heat conduction, considering one of 80 user-selectable materials.

ORSAT is limited to only consider ballistic re-entry of non-lifting bodies. As such, the aerodynamic analysis extends only to calculate the drag coefficient of the body along its re-entry trajectory.

Transitional region drag coefficients and thermal heating are approximated using Knudsen number dependant bridging functions.

$$C_{D_{trans}} = C_{D_{cont}} + (C_{D_{cont}} - C_{D_{fm}}) * [\sin(\pi[0.5 + 0.25 \ln Kn])]^3 \quad (5)$$

Where  $C_{D_{cont}}$  and  $C_{D_{fm}}$  are shape and motion dependant.

Transitional heat transfer is approximated using shape dependant bridging functions, described in *table 3*:

| Object Shape          | Bridging Function   |
|-----------------------|---|
| Spheres and cylinders | Logarithmic Stanton number bridging for $0.001 < Kn < 10$<br>Cheng's Theory [15], presented by Cropp [16], Stanton number calculation for $0.01 < Kn < 10$  |
| Flat plates and boxes | Exponential bridging function:<br>$\dot{Q}_{trans} = \dot{Q}_{cont} \left[ 1 - \exp \left( - \frac{\dot{Q}_{fm}}{\dot{Q}_{cont}} \right) \right] \quad (6)$ |

Table 3 - ORSAT Transitional Formulations

Where:

$$\dot{Q}_{st_{cont}} = \frac{110285}{\sqrt{R}} \left( \frac{\rho_{\infty}}{\rho_{sl}} \right) \left( \frac{V_{\infty}}{V_{circ}} \right)^{3.15} \quad (7)$$

$$\dot{Q}_{st_{fm}} = \frac{\alpha_T \rho_{\infty} V_{\infty}^3}{2} \quad (8)$$

$\alpha_T$  is the thermal accommodation coefficient, fixed at 0.9.

ORSAT uses either the US Standard Atmosphere model of 1976, or the Mass Spectrometer Incoherent Scattering Extended – 1990 model for atmospheric calculations.

ORSAT is not currently freely available to non-US citizens.

### 2.3.2 DRAMA

The Debris Risk Assessment and Mitigation Analysis (DRAMA) is another object-orientated simulation tool, developed to be a supporting application for the European Space Debris Mitigation Standard (EDMS) [14]. DRAMA estimates the mass, cross section, velocity, incident angle and impact location of surviving object fragments upon completing atmospheric re-entry from either direct re-entry or orbital decay.

DRAMA shares the same aerodynamic and aerothermodynamic models as ORSAT, with a number of key differences:

- Only random tumbling and spinning is considered for the same list of geometric shapes.
- Only uses the lumped thermal mass model, but with continuing melting.
- Does not consider oxidation heating.
- Subsonic drag coefficient is estimated as 50% of the hypersonic continuum drag coefficient.
- Simplified transitional stagnation heat transfer bridging formula:

$$St_{trans} = \frac{St_{cont}}{1 + \frac{St_{cont}}{St_{fm}}} \quad (9)$$

### 2.3.3 SCARAB

The Spacecraft Atmospheric Re-Entry and Aerothermal Break Up (SCARAB) computational tool is a spacecraft orientated code developed by Hypersonic Technology Gottingen (HTG) since 1995 [17] [14]. SCARAB implements aerodynamic, aerothermodynamic, 6DOF flight dynamics, heat conduction, destruction by melting or fracture and fragment tracking models for any spacecraft geometry composed of a combination of simple geometric shapes, shown in *figure 9*.



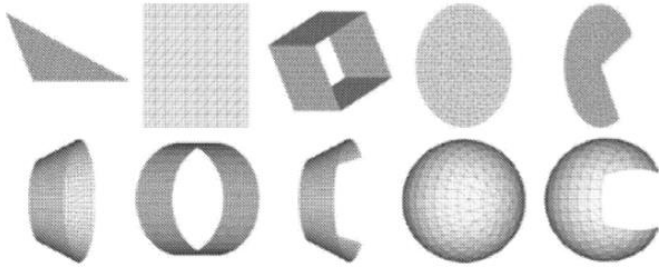


Figure 10 - SCARAB geometry library

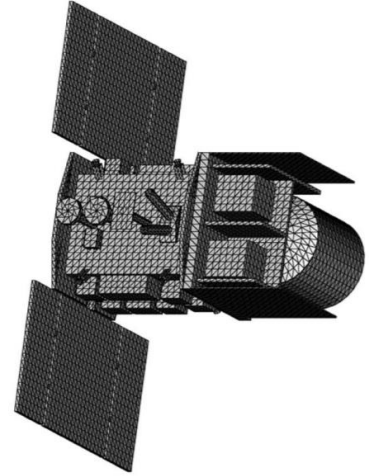


Figure 9 - Complex geometry created by SCARAB

SCARAB uses several different atmospheric models, including the USSA 1976, NRLMSISE-90 and NRLMSISE-00, in addition to the following hypersonic approximations for aerodynamic and aerothermodynamic parameter estimation through each hypersonic flow regime:

| Flow Regime           | Aerodynamic Model   | Aerothermodynamic Model   |
|-----------------------|---|---|
| <b>Free Molecular</b> | Free molecular integral method with Nocilla or Schaaf-Chambre accommodation coefficients [18]. No catalysis or chemical reactions (inert wall). |   |
| <b>Transition</b>     | Knudsen number and local flow inclination dependant bridging.   | General bridging formula:<br>$\dot{q} = \frac{\dot{q}_{cont}}{\sqrt{1 + \left(\frac{\dot{q}_{cont}}{\dot{q}_{fm}}\right)^2}} \quad (10)$                    |
| <b>Continuum</b>      | Modified Newtonian theory (function of Mach number, specific heat ratio and local flow inclination).  | Modified Lees theory [12]<br>$St = \frac{2.1}{\sqrt{Re_\infty}} (0.1 + 0.9 \cos \theta) \quad (12)$ <p>Assumed viscosity law:</p> $\mu(T) \propto T^{0.78}$ |

Table 4 - SCARAB Hypersonic Formulation

### 2.3.4 FOSTRAD

The Free Open Source Tool for Re-Entry of Asteroids and Debris (FOSTRAD) is an LSI based approach under development at the University of Strathclyde [19]. Initially designed specifically for simple shapes representative of space debris or asteroids, FOSTRAD can now be used to simulate the aerodynamics and aerothermodynamics of any uploaded 3D geometry across the continuum, transitional and free-molecular hypersonic flow regimes.

Continuum and Free Molecular aerodynamic computations are performed using Modified Newtonian Theory and the Schaaf and Chambre analytical model respectively.

FOSTRAD employs a number of models for computing continuum regime aerothermodynamics, including the Detra-Kemp-Riddell model (as used in SCARAB), the Van Driest model and the Fay-Riddell model. Free Molecular aerothermodynamics are computed using the free molecular analytical model.

FOSTRAD computes transition region values using a newly developed bridging function based on the 5PL least squares regression method proposed by Baud [20].

FOSTRAD presents as an output scalar values of the coefficients of lift, drag, sideslip, pitching moment, rolling moment and yaw moment, average surface heat transfer and heat transfer coefficient. Additionally, vector quantities of surface heat transfer flux, coefficient of heat transfer and total heat transfer are included to allow the visualisation of parameters across the simulated geometry. An example of this is shown in *figure 11* [21].

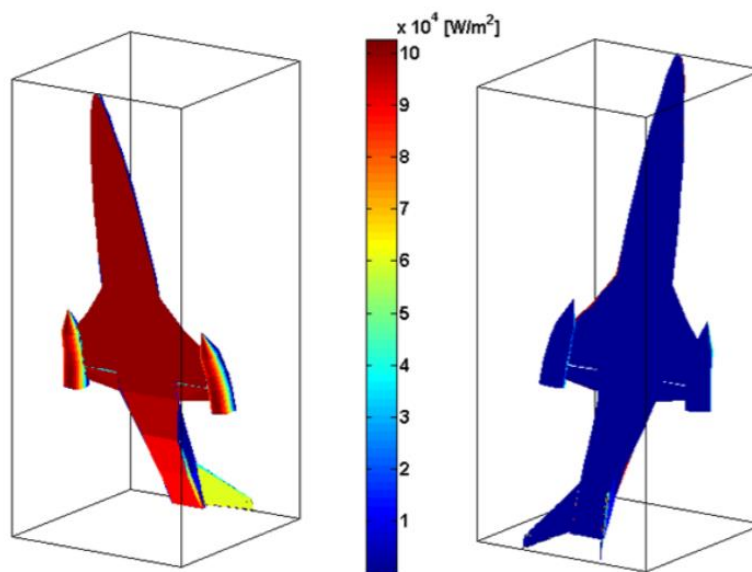


Figure 11 - Heat transfer flux ( $\text{W/m}^2$ ) of CFASTT-1 computed using FOSTRAD 2.0

### 2.3.5 X-FOIL

X-FOIL, developed by the Massachusetts Institute of Technology (MIT), is an early computer panel method implementation for subcritical aerofoils [22]. X-FOIL is a 2D, open source and FORTRAN based program that uses an inviscid, linear-vorticity panel method solved with the Newton method. This program has been continuously updated since June 2013, but has not increased in functionality beyond a 2D aerofoil simulation tool.

### 2.3.6 APAME

The Aircraft Panel Method (APAME), produced by Daniel Filkovic from the University of Zagreb in Croatia, 2008, is a 'potential flow' simulation for subsonic aircraft. The program is well documented and maintained. APAME discretises a 3D geometry into a series of square panels in order to implement an influence coefficient method solution [23]. This program is validated against ANSYS FLUENT for an entire aircraft body. In general, APAME shows some promise in delivering accurate results, but can display errors of up to 40% compared to higher fidelity solutions. These issues should be considered if APAME is to be used as a base for the future program development.

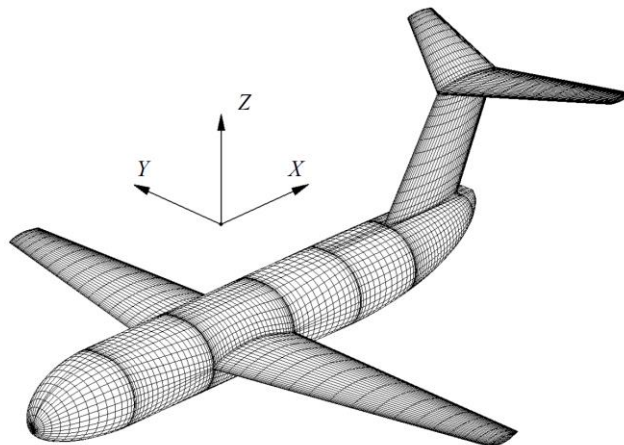


*Figure 12 - APAME Mesh Formulation*

## 3 Code Structure

### 3.1 Language and development

One primary project requirement is for the complete program to be open source. The use of the commercial software, MATLAB (the programming environment within which FOSTRAD, the code which provides the basis for the hypersonic module of PASTA 1.2, exists), would therefore prohibit this.

A number of programming languages were considered for use within this project. Programming languages such as Fortran are rapidly becoming obsolete with the development of modern languages and methods. C# is a lower level, more user-friendly language, but in general much more suited to the .NET framework on Windows, which would make cross platform functionality difficult to achieve.

The choice was therefore narrowed to C++ or Python. Each language offers multiple benefits when used to carry out certain tasks [24]. It has been found that in almost all cases, C++ is the more efficient language in terms of computational load, despite being less user friendly or intuitive. C++ is a 'compiled' language, while Python is generally run as an 'interpreted' language.

This means that C++ has the ability to allocate RAM and CPU power more effectively than Python, as Python must execute the source code line by line through an 'interpreter', a requirement for the CPU to 'read' instructions. This proved to be a major factor, primarily due to the large memory requirement necessitated by the vectors formed from importing STL file data.

C++ contains a number of additional benefits. C++ is an 'object-oriented' programming language and includes classes, inheritance, polymorphism, data abstraction and encapsulation.

As one fundamental aim of this project necessitated maximum computational performance, C++ was chosen as the operating language for the code. C++ includes a large number of standard function libraries. This allowed the workflow of PASTA 1.2 to be constructed as near to its theoretical operation within MATLAB, the programming environment each member of the team had significantly more experience with, as closely as possible. Finally, C++ offers the potential for cross-platform functionality. This is further discussed in *section 13*.

The code was developed using the Microsoft Visual Studio Integrated Developing Environment (IDE) by first creating the overall framework of the program. Namely, the input and output modules. This was coupled with the ability to run the original FOSTRAD 2.0 code using the MATLAB engine called from within the C++ programming environment. This allowed the output of the simulation to be continuously validated and modified throughout the process of gradually integrating the additional C++ modules in turn.

### 3.2 Description

PASTA 1.2 has been designed as a series of individual standalone ‘modules’. This allows both for the efficient location of errors, easier code modification and testing, as well as greater usability with respect to future updates. Modules can be easily separated from the main code and replaced with updated versions.

A summary of the modules included within PASTA 1.2, and the overall code structure, are shown in *table 5* and *figure 13* respectively.

| MODULE            | DESCRIPTION  |
|-------------------|--|
| <b>Input</b>      | Reads a local text file and geometry STL file, extracts relevant data  |
| <b>Geometry</b>   | Processes geometry information to obtain facet areas, incentres, centre of gravity, and HSR matrix   |
| <b>Atmosphere</b> | Evaluates atmospheric conditions based on operational inputs   |
| <b>Hypersonic</b> | Estimates aerodynamics and aerothermodynamics across continuum, transitional or free molecular flow  |
| <b>Supersonic</b> | Estimates supersonic aerodynamics  |
| <b>Subsonic</b>   | Estimates subsonic aerodynamics  |
| <b>Output</b>     | Creates a text file displaying scalar data, a VTK file displaying distribution data, and prints scalar data to the console screen, along with run-time information |

*Table 5 - PASTA 1.2 Module Descriptions*

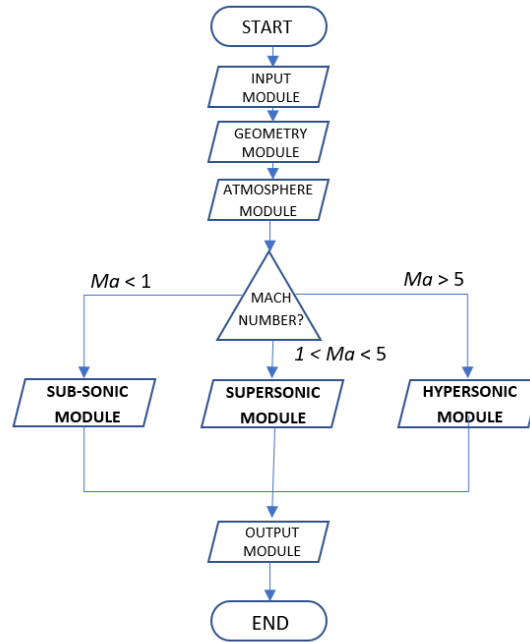


Figure 13 - PASTA Module Flow Hierarchy

### 3.3 Performance

To justify the use of a low fidelity model, the model must deliver results of reasonable accuracy, while significantly out-performing any higher fidelity method in terms of computational cost.

The computational cost of PASTA 1.2, similarly to higher fidelity methods, is primarily dictated by the number of individual facets used to describe the geometry selected for simulation. PASTA 1.2 has been compared to DSMC and CFD high fidelity simulations, as well as the LSI method FOSTRAD code. Details of DSMC and CFD computational costs, presented by Lofthouse, can be seen in *table 6* [25].

| DSMC  |        |                      |            |                     |                     |
|-------|--------|----------------------|------------|---------------------|---------------------|
| Kn    | Cells  | Particles            | Time Steps | CPUs                | Total CPU Time (hr) |
| 0.002 | 394250 | 287x10 <sup>6</sup>  | 1050000    | 128                 | 57186               |
| 0.01  | 68497  | 26.8x10 <sup>6</sup> | 430000     | 32                  | 1827                |
| 0.05  | 18818  | 7.1x10 <sup>6</sup>  | 430000     | 32                  | 499                 |
| 0.25  | 24452  | 8.2x10 <sup>6</sup>  | 290000     | 32                  | 387                 |
| CFD   |        |                      |            |                     |                     |
| Kn    | Cells  | Iterations           | CPUs       | Total CPU Time (hr) |                     |
| 0.002 | 80000  | 25000                | 8          | 150                 |                     |
| 0.01  | 40000  | 25000                | 8          | 75                  |                     |
| 0.05  | 40000  | 25000                | 8          | 75                  |                     |
| 0.25  | 40000  | 25000                | 8          | 75                  |                     |

Table 6 - DSMC/CFD Computational Cost

Figure 14 shows the comparison in run time between PASTA 1.2 and FOSTRAD 2.0 relative to the number of facets in each simulation. It should be noted that while PASTA 1.2 appears to out-perform FOSTRAD 2.0 in this metric, FOSTRAD 2.0 is operated within the MATLAB programming environment, and as such exists as a pre-compiled code. This therefore limits the computational speed that can be expected.

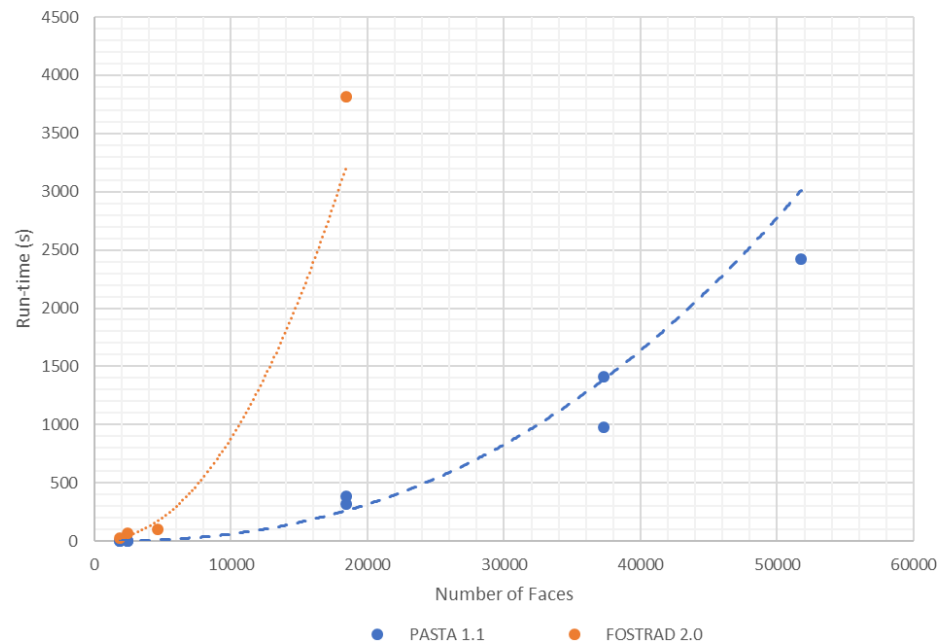


Figure 14 - Run-time Comparison

This demonstration of the computational load expected from PASTA 1.2 validates its potential as a preliminary design tool, offering an order of magnitude saving on time compared to DSMC/CFD simulations.

## 4 Input Module

The PASTA 1.2 input module works by reading input data from a dedicated configuration file, located within the main root directory. This input file is split into multiple sections, each displaying a different class of input. The definitions of each input section are shown in *table 7*.

| INPUT TYPE             | DEFINITION   | INCLUDED PARAMETERS  |
|------------------------|--|--|
| <b>Initialisation</b>  | System level definitions needed for code execution               | Main Directory<br>Geometry Directory<br>STL File Name                                  |
| <b>Operational</b>     | Input relating to the specific physical situation to be analysed | Altitude<br>Velocity<br>Angle of Attack<br>Angle of Sideslip<br>Fixed Wall Temperature |
| <b>Design</b>          | Inputs describing the geometry being analysed                    | Reference Length<br>Reference Cross Section<br>Nose Radius                             |
| <b>Model Selection</b> | User selectable models   | USSA 1976<br>NRLMSISE-00   |

*Table 7 - PASTA 1.2 Input Criteria*

This module has been designed to facilitate any future changes to the required input parameters. For example, users could modify the input file to include a aerothermodynamic model selection or include more detailed parameters relating to the geometry, or the desired operational test case.

Additionally, the format of the input module should allow the conversion of the code to run as a callable function to be relatively simple to implement. This could be the subject of future work.



## 5 Atmosphere Module

### 5.1 Introduction

The atmosphere is a series of gaseous layers (*figure 15*) held to the earth's surface by gravity. Although the generally accepted boundary between the earth's atmosphere and space (the Karman Line) is taken as 100km, an 'atmosphere' exists in some form up to heights of 2000km from the earth's surface.

Atmospheric models are generally formulated as either global or local, static or non-static. Global models describe mean latitude conditions (45°N), typically for an average time period between solar minima and solar maxima. Conversely, local models are designed to be only applicable to certain locations, such as a runway, launch site, or country. This approach can result in more accurate simulation of atmospheric properties if the proposed flight is confined to that specified region. Static models assume that atmospheric conditions do not change with time and take no account of fluctuations in solar activity or horizontal wind currents. More advanced models include both spatial and temporal variations of global atmospheric conditions.

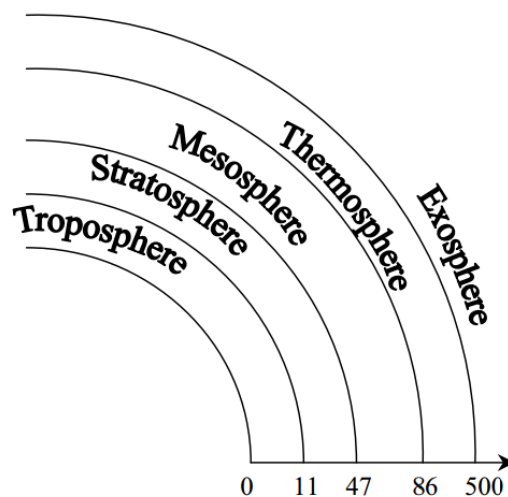


Figure 15 - Atmospheric Layering (km)

## 5.2 US 1976

The US Standard Atmosphere of 1976 [26] [27] is an idealized, global and static representation of the Earth's atmospheric conditions from ground level to 1000km altitude. USSA 76 is a major revision of the 1962 standard, developed by COESA. Pressure, Temperature, Density, speed of sound, molecular weight, mean free path, thermal conductivity, dynamic and kinematic viscosity are modelled assuming mid latitude (45° North), mean conditions over the diurnal cycle, semi-annual variation and the range of conditions from active to quiet geomagnetic and sunspot conditions.

This model is largely based on increased rocket data for the mesosphere and lower thermosphere, as well as a large collection of satellite measurements of the thermosphere recorder over the period of 1 complete solar cycle of 11 years.

Typical uses of the USSA 76 include aircraft and rocket design and performance analysis, pressure altimeter calibration, ballistic tables and meteorological diagrams. This is due primarily to the model's inherent simplicity, allowing for ease of integration into more advanced simulation procedures.

## 5.3 NRLMSISE-00

The Naval Research Laboratory Mass Spectrometer Incoherent Scatter Radar Extended Model of 2000 (NRLMSISE 00) is a global, non-static, empirical model of the atmosphere from sea level to 1400km altitude [28]. This model is a major revision of the MSISE 90 model, taking into account numerous new primary data sets, including total mass density measurements from satellite accelerometers and orbit determination, incoherent scatter radar temperature measurements from 1981 to 1997, and solar ultraviolet occultation measurements of the number density of molecular oxygen.

NRLMSISE-00 estimates atmospheric temperature and gas constituent number densities as functions of altitude, latitude, longitude, year, time of day, local apparent solar time and daily magnetic index.

NRLMSISE 00 assumes diffusive equilibrium above 200km, approximate hydrostatic equilibrium between 100 and 200km, and hydrostatic equilibrium below 100km.

## 5.4 Comparison between US76 and NRLMSISE-00

This section presents the comparisons between the USSA 76 and NRLMSISE-00 models used within PASTA 1.2. The NRLMSISE 00 model is computed for a period of average solar activity, taken as January 1<sup>st</sup> 2000 at 45° Latitude and 55° longitude.

### TEMPERATURE

The US Standard Atmosphere of 1976 calculates the atmospheric temperature using a series of distinct layers. Below 86km, seven layers describing a linear variation of *molecular* scale temperature are used. Above 86km, the molecular weight of the gaseous constituents of the air can no longer be considered constant, primarily due to molecular dissociation and diffusive separation. USSA 76 therefore models *kinetic* temperature as four distinct layers incorporating non-linear variation with altitude. USSA 76 asymptotically tends to an assumed exospheric temperature of 1000K.

NRLMSISE 00 calculates temperature in the thermosphere ( $> 120\text{km}$ ) as a function of the exospheric temperature (Bates profile), determined from solar and geomagnetic activity. Below 120km, a series of cubic splines are used to calculate the neutral atmospheric temperature.

Atmospheric temperatures from 0-1000km and 0-100km altitude, calculated using both USSA 76 and NRLMSISE 00, are shown in *figure 16*.

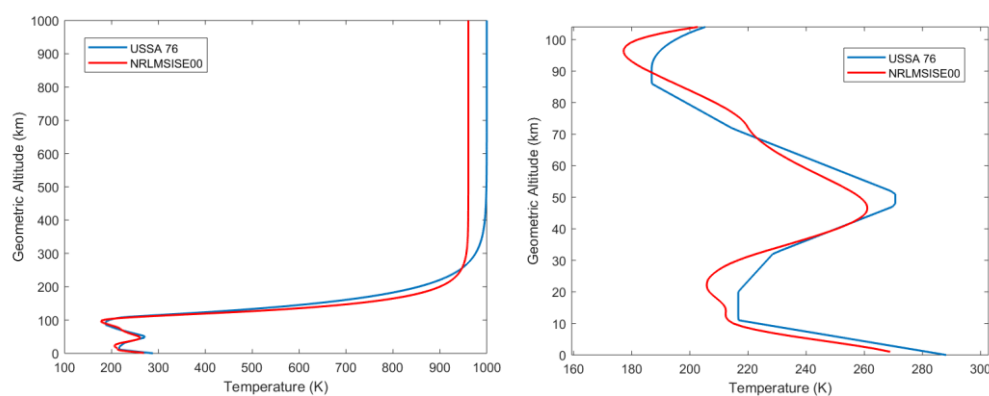


Figure 16 - Atmospheric Temperature

## GAS COMPOSITION

USSA 76 calculates the number density for each primary gas constituent using a series of empirical equations, species dependant and altitude dependant coefficients.

NRLMSISE 00 calculates the number density for each gas species using a functions of reference density value, mixing ratio, turbopause height and dynamic flow/chemistry corrections.

Figures 17 and 18 show the vertical variation of gas species number density calculated using the USSA 76 and NRLMSISE 00 models.

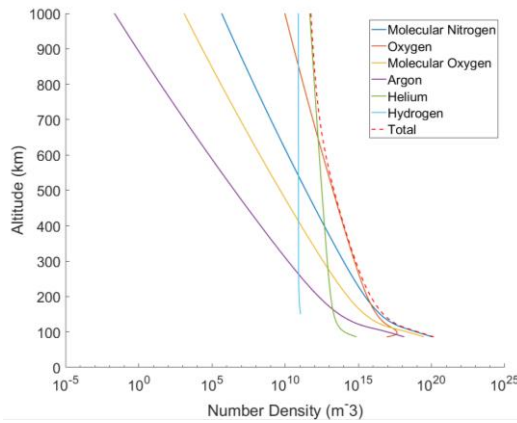


Figure 17 - USSA 76 gas number density (>86km)

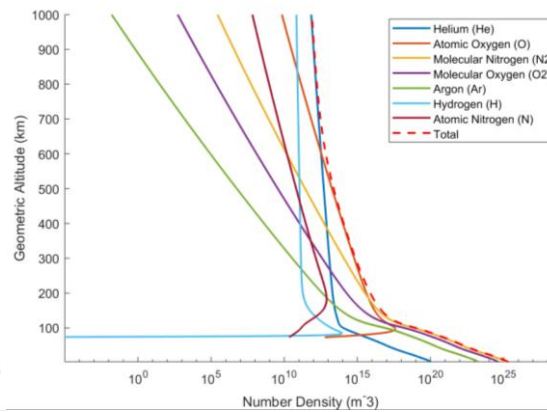


Figure 18 - NRLMSISE 00 number density (0-1000km)

## PRESSURE

USSA 76 calculates atmospheric pressure again by considering a set of distinct layers. Below 86km, air is considered to be a homogenous mixture of several constituents in hydrostatic equilibrium. Pressure in this region is calculated using two expressions derived from the equation of state and the definition of the linear distribution of the molecular scale temperature at each temperature layer. Above 86km, USSA calculates atmospheric pressure as the sum of individual partial pressures for each gas species present at that altitude.

NRLMSISE 00 calculates atmospheric pressure based on the equation of state, using the total air density calculated using the individual gas species number density values.

Atmospheric pressure from 0-1000km altitude, calculated using both USSA 76 and NRLMSISE 00 is shown in *figure 19*.

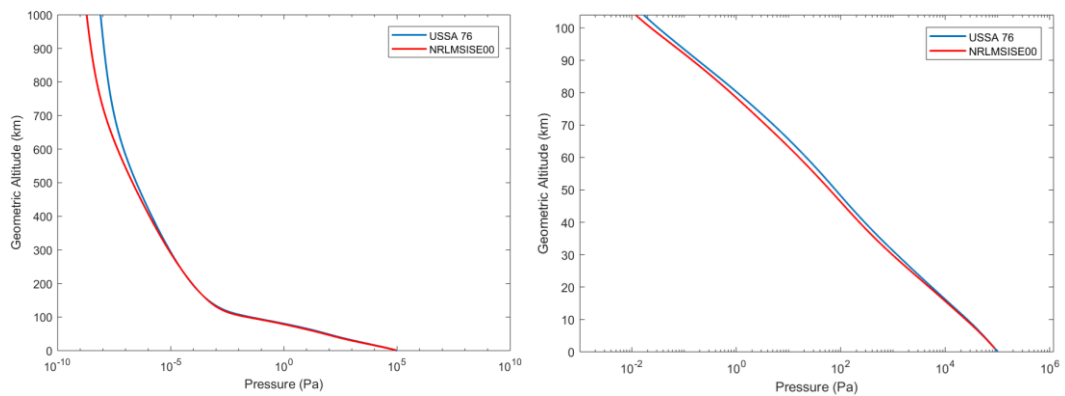


Figure 19 - Atmospheric Pressure

## DENSITY

USSA 76 calculates density according to the equation of state.

NRLMSISE 00 calculates atmospheric density using the sum of each gas species number density.

Atmospheric pressures from 0-1000km and 0-100km altitude, calculated using both USSA 76 and NRLMSISE 00, are shown in *figure 20*.

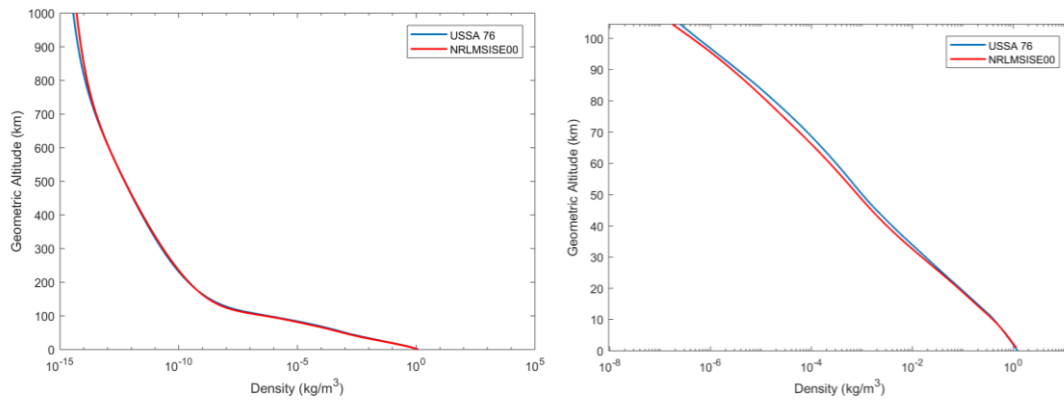


Figure 20 - Atmospheric Density (0 - 1000km)

## SPEED OF SOUND

The speed of sound is calculated using the standard function:

$$c = \sqrt{\gamma RT} \quad (13)$$

The speed of sound from 0-1000km and 0-100km altitude, calculated using both USSA 76 and NRLMSISE 00, is shown in *figure 21*.

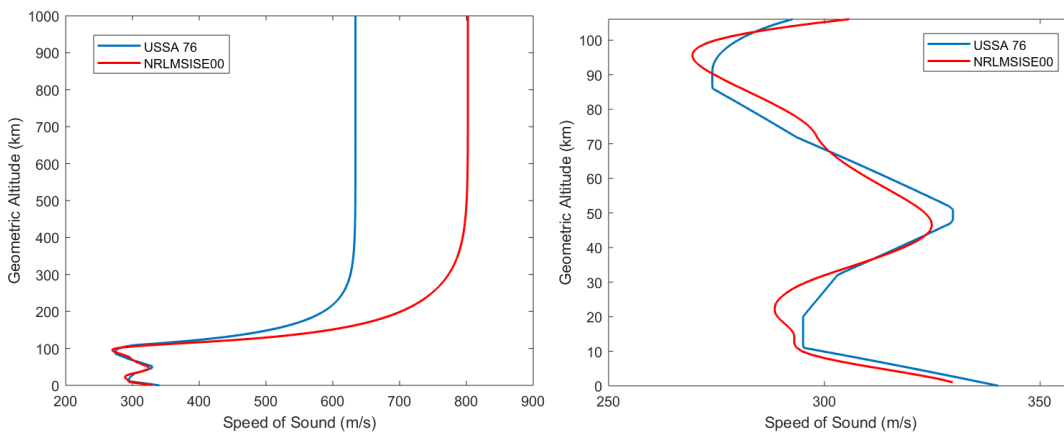


Figure 21 - Speed of Sound

## DYNAMIC VISCOSITY

Dynamic viscosity is calculated in both the USSA 76 and NRLMSISE 00 models using the following semi-empirical formulation based on kinetic theory, where  $\beta = 1.458 \times 10^{-6} \text{ kg/(s m K}^{\frac{1}{2}})$ , and the Sutherland constant  $S = 110.4 \text{ K}$ .

$$\mu = \frac{\beta T^{\frac{3}{2}}}{T + S} \quad (14)$$

Dynamic viscosity from 0-1000km and 0-100km altitude, calculated using both USSA 76 and NRLMSISE 00, is shown in *figure 22*.

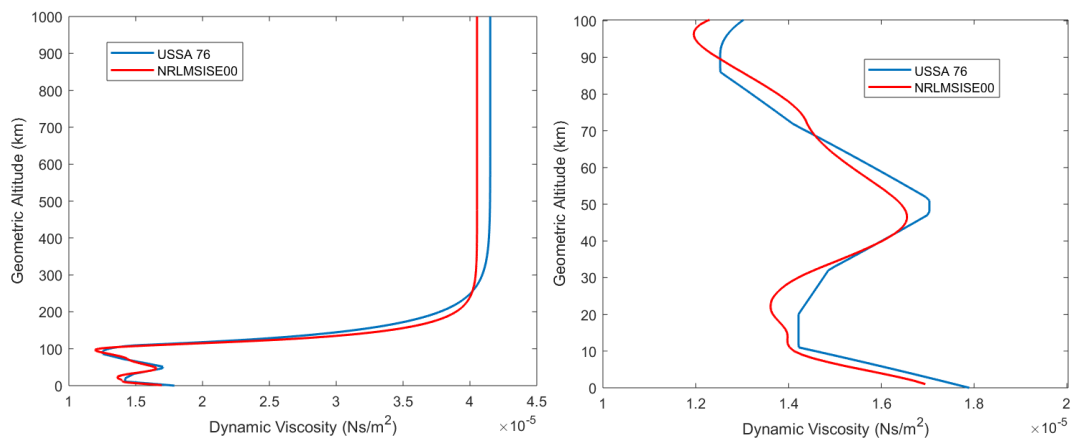


Figure 22 - Dynamic Viscosity

## 6 Geometry Module

The geometry module of PASTA 1.2 reads and processes a user specified geometry model. Front end culling and Ray tracing techniques are used to reduce the total number of mesh triangles included in the computation, to both reduce computational load and improve the accuracy of aerodynamic and aerothermodynamic characteristics estimation.

### 6.1 Reading

PASTA 1.2 uploads geometry information by reading a user defined Binary or ASCII STL file. An STL, short for stereolithographic, file describes an unstructured triangulated surface by expressing the unit normals and vertices (ordered by the right-hand rule) of the triangles using a 3D Cartesian coordinate system.

The STL file format was chosen due to the large prevalence of STL support present in modern CAD software.

The geometry selected for simulation must conform to the axes specifications shown in *figure 23*. The geometry must face in the negative  $X$  direction, have the top surface facing the positive  $Z$  direction, and the starboard side face the positive  $Y$  direction.

The CAD model represented by the STL must have been generated using meters as the default dimension.

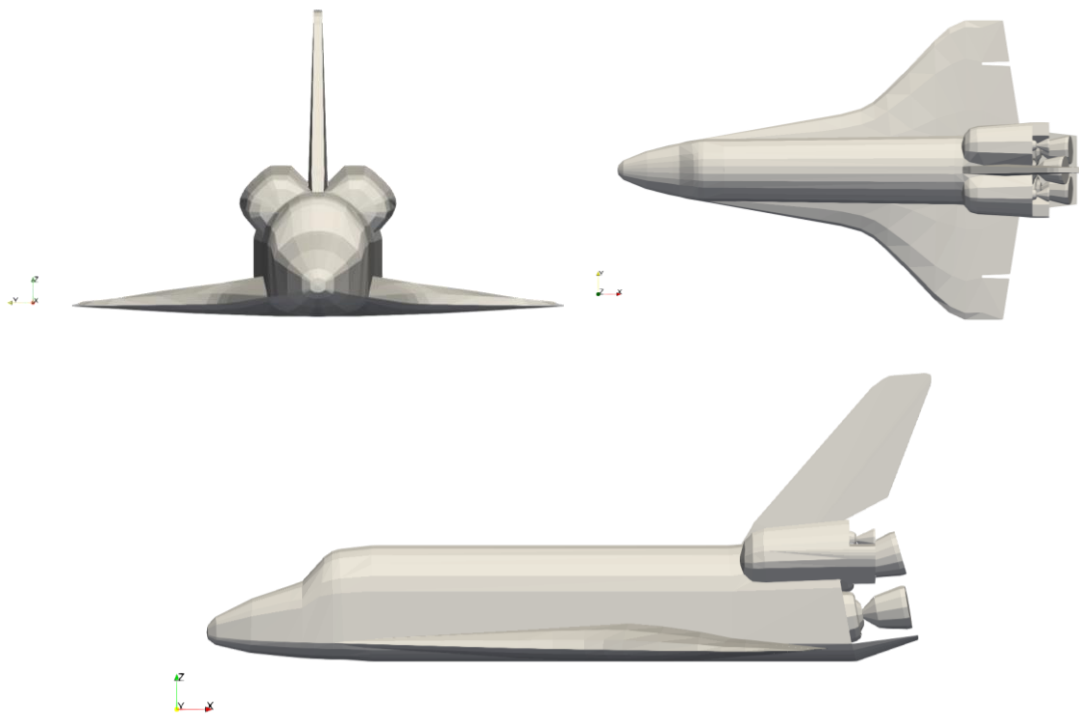


Figure 23 - STL Axes Orientation



### 6.1.1 ASCII Support

PASTA 1.2 will read any ASCII STL file conforming to the following general format:

```
solid name
facet normal  $n_i$   $n_j$   $n_k$ 
  outer loop
    vertex  $v1_x$   $v1_y$   $v1_z$ 
    vertex  $v2_x$   $v2_y$   $v2_z$ 
    vertex  $v3_x$   $v3_y$   $v3_z$ 
  endloop
endfacet
endsolid name
```

As of March 2018, numerical values within the ASCII STL file must be represented by decimal values, rather than scientific notation. This limitation will be removed before the release of the completed program.

### 6.1.2 Binary Support

PASTA 1.2 will read any Binary STL file conforming to the following general format:

```
UINT8[80] - Header
UINT32 - Number of triangles

foreach triangle
  REAL32[3] - Normal vector
  REAL32[3] - Vertex 1
  REAL32[3] - Vertex 2
  REAL32[3] - Vertex 3
  UINT16 - Attribute byte count
end
```

### 6.1.3 Geometry Calculations

#### INCENTRES

Individual facet incentre coordinates are calculated as:

$$\begin{bmatrix} O_x \\ O_y \\ O_z \end{bmatrix} = \begin{bmatrix} A_x & B_x & C_x \\ A_y & B_y & C_y \\ A_z & B_z & C_z \end{bmatrix} \begin{bmatrix} a \\ b \\ c \end{bmatrix} * \frac{1}{p} \quad (15)$$

Where  $a$ ,  $b$  and  $c$  represent the side lengths opposite vertex  $A$ ,  $B$  and  $C$  respectively, and  $p$  is the perimeter of the facet triangle.

#### CENTRE OF GRAVITY

The centre of each facet is calculated as the average  $x$ ,  $y$  and  $z$  coordinates between each vertex.

The centre of gravity of the entire geometry is similarly taken as the average  $x$ ,  $y$  and  $z$  coordinate of the facet incentres.

#### AREAS

The area of each facet is calculated using a stabilized Heron formula [29]:

$$A = \frac{1}{4} \sqrt{(a + (b + c)) * (c - (a - b)) * (c + (a - b)) * (a + (b - c))} \quad (16)$$

Where facet edges  $a$ ,  $b$  and  $c$  are organised as:

$$a \geq b \geq c$$

## 6.2 Back-Face Culling/Hidden Surface Removal

It is well known that according to Newtonian theory, the geometry of an object traveling at hypersonic speeds can shield parts of the surface from the oncoming flow. This is primarily due to flow particles losing all momentum normal to the surface at the first point of contact with the considered geometry. For complex geometry, this effect can significantly alter the predicted aerodynamics. Therefore, any LSI simulation method must include a shading analysis of the simulated geometry, to determine the portion of the surface not visible to the oncoming flow.

Back face culling is a graphical pre-processing phase to determine which faces of a geometry are visible, and which are hidden. PASTA 1.2 uses a combination of two back-face culling techniques:

### 6.2.1 Front-end culling

Front end culling involves the removal of all facets that face away from the viewing vector. This is performed within PASTA 1.2 by first calculating the dot product of the surface normal of each facet with the free stream velocity vector  $V_\infty$ . If

$$V_\infty \cdot \hat{n} \leq 0 \quad (17)$$

is true, the corresponding facet is marked as 'seen', and can be included in the simulation.

This method is suitable for any convex geometry. However, any complicated geometry consisting of concave components cannot be fully processed using this method. *Figure 24* shows a 3D stereolithographic model of the STS orbiter, processed using the front-end culling algorithm within PASTA 1.2.

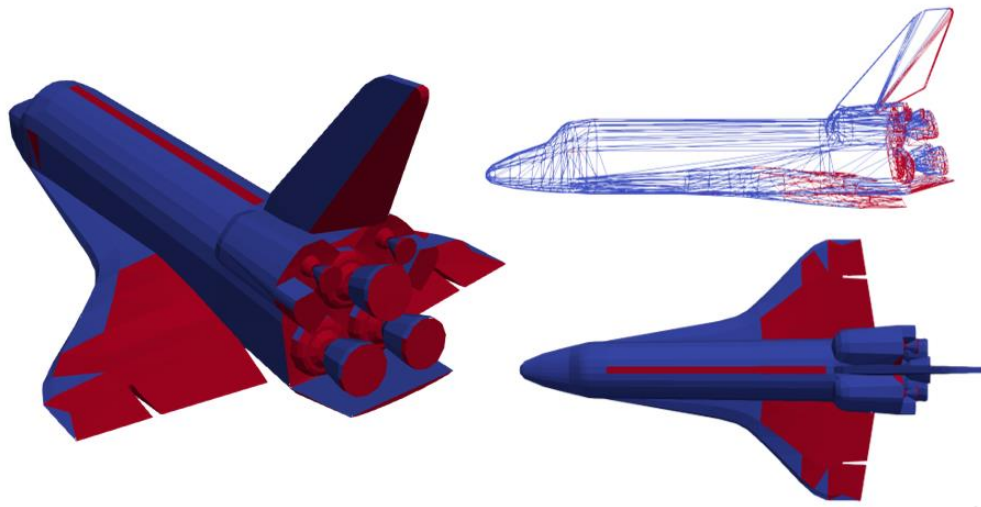


Figure 24 - Front End Culling

It can be seen that while this method removes the majority of unseen facets, there remain some occlusions, particularly around the RS25 engine bells at the rear of the model.

### 6.2.2 Ray tracer

A more advanced technique for Hidden Surface Removal is Ray Tracing. Ray Tracing involves simulating a series of straight lines emitted from a source upstream of the body. Each ray is tested for intersection against each facet. The first facet that a single ray intersects is marked as 'seen' and included in the simulation. Assuming an appropriate number of rays relative to the total number of facets in a particular geometry, this method effectively occludes all hidden surfaces, at the cost of computational time.

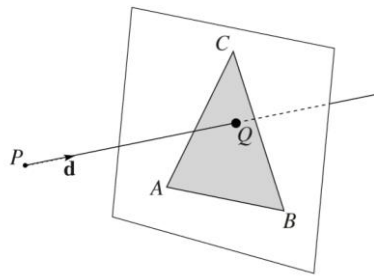


Figure 25 - Simple Ray Tracer

To determine whether a ray intersects a particular facet, two steps must be followed:

1. Calculate the point of intersection of the ray with origin  $P$  and direction vector  $\mathbf{d}$ , with the facet plane at point  $Q$
2. Determine whether  $Q$  lies within the facet  $ABC$

The supporting plane of a facet is calculated using the well-known equation for a 3D plane:

$$ax + by + cz = d \quad (18)$$

Coefficients  $a$ ,  $b$  and  $c$  form the normal vector of the plane:

$$\mathbf{n} = [a \ b \ c]^T$$

The plane equation can therefore be rewritten as:

$$\mathbf{n} \cdot \mathbf{x} = d$$

Where  $\mathbf{x} = [x \ y \ z]^T$

Considering the ray with origin at point  $P$ , distance  $t$  and direction vector  $\mathbf{d}$ :

$$R(t) = P + t\mathbf{d} \quad (19)$$

Equating coordinate  $R(t)$  with the  $\mathbf{x}$  vector in the plane equation allows the distance between the ray origin and the plane intersection to be calculated:

$$\mathbf{n} \cdot R(t) = d$$

$$\mathbf{n} \cdot [P + t\mathbf{d}] = d$$

$$\mathbf{n} \cdot P + t\mathbf{n} \cdot \mathbf{d} = d$$

$$t = \frac{d - \mathbf{n} \cdot P}{\mathbf{n} \cdot \mathbf{d}}$$

Note that direction vector  $\mathbf{d}$  is parallel to the plane if  $\mathbf{n} \cdot \mathbf{d} = 0$ , and therefore does not register as an intersection. In PASTA 1.2, this special case is checked for, and used to evaluate parallel facets as ‘seen’.

Intersection point  $Q$  can therefore be found by substituting  $t$  into the ray equation:

$$Q = P + \frac{d - \mathbf{n} \cdot P}{\mathbf{n} \cdot \mathbf{d}} \mathbf{d}$$

Where  $d$  is calculated by noticing that any vertex of the facet in question must therefore lie on the supporting plane, thus satisfying  $\mathbf{n} \cdot \mathbf{x} = d$ . For example, using vertex  $A$ :

$$d = \mathbf{n} \cdot A$$

To compute whether the intersection point  $Q$  lies within triangle  $ABC$ ,  $Q$  is tested against each edge of  $ABC$ :

$$[(B - A) * (Q - A)] \cdot \mathbf{n} \geq 0 \quad (20)$$

$$[(C - B) * (Q - B)] \cdot \mathbf{n} \geq 0$$

$$[(A - C) * (Q - C)] \cdot \mathbf{n} \geq 0$$

If each of these cases is true,  $Q$  lies within triangle  $ABC$ .

PASTA 1.2 implements this technique by creating a number of rays equal to the number of facets included in the geometry, with  $y$  and  $z$  coordinates equal to those of the centre point of each particular facet, and an  $x$  coordinate equal to the lowest value  $x$  coordinate of the entire geometry. The direction vector of each ray is equivalent to the free stream velocity vector. A simple representation of this procedure is shown in *figure 26*, where the red coloured sections represent the ‘hidden’ facets.

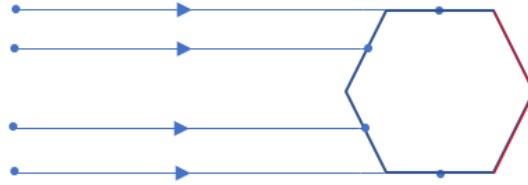


Figure 26 - PASTA 1.2 Ray Tracing

Each ray is then tested for intersection with each facet. In the cases where a ray intersects multiple facets, the facet closest to the origin of the ray is marked as 'seen'. The resulting face culling is shown in *figure 27*.

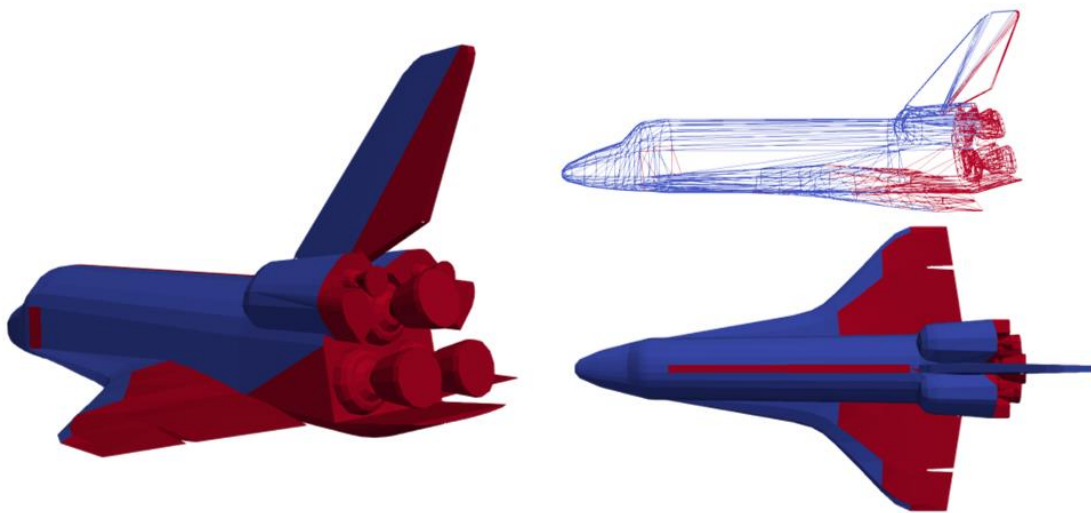


Figure 27 – 'Ray Tracer' Hidden Surface Removal

### 6.2.3 Results

To decrease the computational load of the Hidden Surface Removal within PASTA 1.2, the Ray tracing algorithm is only applied using faces not previously removed by the front-end culling technique.

The advantages of this pre-processing of the geometry is detailed by Benedetti [21]. Geometry pre-processing gives both a more efficient execution of the code, in addition to an overall more accurate final implementation, with respect to higher fidelity simulations.

It should be noted that this Ray Tracing technique is largely sensitive to mesh resolution. Too coarse a mesh will provide largely inaccurate facet culling, and too fine a mesh will require an exponentially increased computational cost.

The ray tracing algorithm implemented in PASTA 1.2 is the most computationally expensive aspect of the simulation. Future work could involve improving the efficiency of this implementation or developing an entirely different method. For example, FOSTRAD 2.0 incorporates a *rasterizing* technique in order to avoid the need to implement a ray tracing algorithm. This method involves the assignment of a unique RGB colour to each face remaining after front end culling. An image of the coloured geometry facing directly into the flow direction is then saved and analysed per pixel line. Any colour present in both the original assignment of colours and the analysed raster image allows the corresponding face to be marked as 'seen'. In general, this technique has been shown to outperform the ray tracing method in terms of computational cost, but can depend on the screen resolution of the system running the implementation [30].

## 7 Hypersonic Module

This chapter presents the formulations of the hypersonic aerodynamic and aerothermodynamic modules used within PASTA 1.2. The flow is categorized into three distinct regimes, based on the value of the flow Knudsen number, which relates the molecular mean free path of the flow to the characteristic length of the simulated geometry. The continuum regime is assumed for  $Kn \leq 1 \times 10^{-4}$ , the free molecular regime is assumed for  $Kn \geq 10$  [19] [31] and the transitional regime is taken to lie between the two boundaries.

### 7.1 Aerodynamics

#### 7.1.1 Continuum

Continuum regime aerodynamics are calculated using the modified Newtonian Theory for blunt nosed bodies proposed by Lees [12]. The local pressure coefficient of each facet is calculated using:

$$C_p = C_{p_{max}} \sin^2 \theta \quad \theta \geq 90^\circ \quad (21)$$

Where  $C_p$  and  $C_{p_{max}}$  are the local and stagnation point pressure coefficients, and  $\theta$  is the local flow inclination angle of the facet. Shear contribution is assumed to be 0. The stagnation point pressure coefficient,  $C_{p_{max}}$ , is evaluated using:

$$C_{p_{max}} = \frac{p_{02} - p_1}{\frac{1}{2} \gamma p_1 M_1^2} = \frac{2}{\gamma M_1^2} \left( \frac{p_{02}}{p_1} - 1 \right) \quad (22)$$

Where  $p_{02}$  and  $p_1$  are the stagnation pressure (after normal shock wave) and the free stream static pressure,  $\gamma$  is the ratio of specific heats for air and  $Ma$  is the Mach number of the body.

The normal local pressure coefficient is then calculated, again for each facet, using:

$$C_{pn} = \hat{n} * C_p * \frac{A}{A_{ref}} \quad (23)$$

Where  $\hat{n}$  is the normal vector of the particular facet,  $A$  is the facet area and  $A_{ref}$  is the input reference area.



The Coefficients of Lift, Drag and Sideslip are computed by performing a dot product between the sum of all normal local pressure coefficients, and the Body to Wind rotation matrix, to accommodate the coordinate transformation of a vector in a body reference frame to a vector in a wind reference frame.

$$\begin{bmatrix} C_D \\ C_S \\ C_L \end{bmatrix} = C_{Pn} \cdot B2W = C_{Pn} \cdot \begin{bmatrix} \cos \alpha \cos \beta & \sin \beta & \sin \alpha \cos \beta \\ -\cos \alpha \sin \beta & \cos \beta & -\sin \alpha \sin \beta \\ -\sin \alpha & 0 & \cos \alpha \end{bmatrix} \quad (24)$$

Shear contribution in the continuum region is taken as zero [19].

### 7.1.2 Free-Molecular

Free molecular aerodynamics are approximated using a Schaaf and Chambers analytic model based formulation [32], which accounts for both pressure and shear contributions [33] :

$$C_p = \frac{1}{s^2} \left[ \left( \frac{2 - \sigma_N}{\sqrt{\pi}} s \sin \theta + \frac{\sigma_N}{2} \sqrt{\frac{T_w}{T_\infty}} \right) e^{-(s \sin \theta)^2} + \left\{ (2 - \sigma_N) \left( (s \sin \theta)^2 + \frac{1}{2} \right) + \frac{\sigma_N}{2} \sqrt{\frac{\pi T_w}{T_\infty}} s \sin \theta \right\} (1 + \operatorname{erf}(s \sin \theta)) \right] \quad (25)$$

$$C_\tau = -\frac{\sigma_T \cos \theta}{s \sqrt{\pi}} \left[ e^{-(s \sin \theta)^2} + \sqrt{\pi} s \sin \theta (1 + \operatorname{erf}(s \sin \theta)) \right] \quad (26)$$

$C_p$  and  $C_\tau$  are the pressure and shear coefficients,  $\sigma_N$  and  $\sigma_T$  are the normal and tangential momentum accommodation coefficients.  $T_w$  is the surface wall temperature,  $T_\infty$  is the free stream translational temperature,  $V_\infty$  is the free stream velocity,  $\operatorname{erf}$  is the error function and  $s$  is the molecular speed ratio, defined as:

$$s = \frac{V_\infty}{\sqrt{2RT_\infty}} \quad (27)$$

The error function is defined as:

$$\operatorname{erf}(x) = \frac{2}{\sqrt{\pi}} \int_0^x e^{-y^2} dy \quad (28)$$

For each facet, the local force coefficient is evaluated using:

$$C_F = C_p * \hat{n} * \frac{A}{A_{ref}} + C_\tau * \hat{t} * \frac{A}{A_{ref}} \quad (29)$$

$$\begin{bmatrix} C_D \\ C_S \\ C_L \end{bmatrix} = C_F \cdot B2W = C_F \cdot \begin{bmatrix} \cos \alpha \cos \beta & \sin \beta & \sin \alpha \cos \beta \\ -\cos \alpha \sin \beta & \cos \beta & -\sin \alpha \sin \beta \\ -\sin \alpha & 0 & \cos \alpha \end{bmatrix} \quad (30)$$

### 7.1.3 Transitional

Transitional regime aerodynamics are generally estimated using a bridging function, requiring the computation of the continuum and free molecular limit conditions, based on some function of the local Knudsen number. PASTA 1.2 uses a bridging technique based on the SPL weighted least squares regression method proposed by Baud [20]. This method involves the estimation of parameters  $A$ ,  $B$ ,  $C$ ,  $D$  and  $E$  of the following general function through a numerical optimisation technique:

$$y = A + \frac{D - A}{\left[ \left( 1 + \left( \frac{x}{C} \right)^B \right) \right]^E} \quad (31)$$

Where:

- $A$  is the minimum asymptote
- $B$  is the Hill's slope, a measure of the steepness of the curve.
- $C$  defines the location of the inflection point
- $D$  is the maximum asymptote
- $E$  is the asymmetry factor

The coefficients  $B$ ,  $C$  and  $E$  were determined through a targeted sensitivity analysis to best fit the DSMC data for the Orion MPCV in the transitional regime (presented in *section 11.1.1*).

The values of coefficients  $A$  and  $D$  are taken as the continuum and free molecular values of the desired coefficient, calculated internally by PASTA 1.2 using reference 'continuum' and 'free-molecular' altitudes of 40km and 220km respectively.

Aerodynamic parameters are then directly calculated:

$$C_{x_{trans}} = C_{x_{cont}} + \frac{(C_{x_{fm}} - C_{x_{cont}})}{\left[ \left( 1 + \left( \frac{Kn}{C} \right)^B \right) \right]^E}$$

This bridging function takes the general form displayed in *figure 28*:

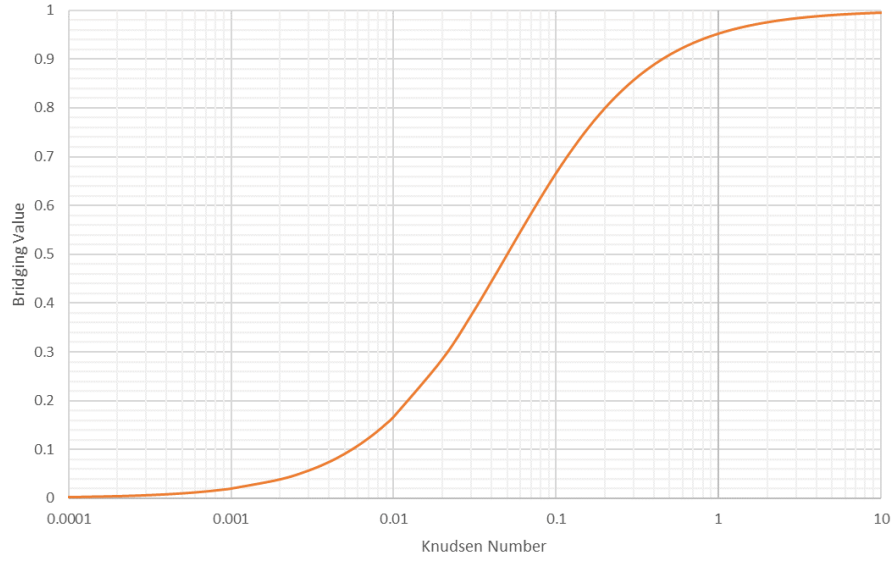


Figure 28 - PASTA 1.2 bridging function (general form)

## 7.2 Aerothermodynamics

This section details the formulation of the continuum, transitional and free molecular models used within PASTA 1.2 to estimate hypersonic aerothermodynamics. All calculations assume an isothermal boundary condition, defined using the ‘fixed wall temperature’ input parameter.

### 7.2.1 Continuum

When considering low fidelity simulation methods, particularly LSI methods, continuum aerothermodynamics are normally computed by estimating the Stanton number using either the modified Lees approach [17]:

$$St = \frac{2.1}{\sqrt{Re_{\infty,0}}} (0.1 + 0.9 \cos \theta) \quad (32)$$

Or the Kemp Rose Detra formulation [34]:

$$St = \frac{2.1}{\sqrt{Re_{\infty,0}}} * \left( \cos \frac{\theta}{2} \right)^{5.27} \quad (33)$$

These methods are primarily chosen due to their simplicity, evaluating the local Stanton number as a function of the flow Reynolds number and the local surface inclination. However, it has been shown [35] [36] that these methods tend to overestimate the resulting

heating rates for different geometries. A correction factor for the modified Lees approach has therefore been developed [37] to increase the usable accuracy of the Kemp Rose Detra formulation.

$$St = C_{corr} \frac{2.1}{\sqrt{Re_{\infty,0}}} (0.1 + 0.9 \cos \theta) \quad (34)$$

Where  $C_{corr} = 0.3476$  has been determined with numerous high fidelity CFD tests across different geometry [37].

Heat transfer rate is therefore computed as:

$$Q = St * \rho * V_{\infty} * Cp * (T_0 - T_w) \quad (35)$$

### 7.2.2 Free-Molecular

Free molecular aerothermodynamic heating is estimated using the Detra-Kemp-Riddell formulation [38].

$$Q = \frac{C_{acc} \rho_{\infty} V_{\infty}^3}{4s^3 \sqrt{\pi}} \left[ \left[ \left( s^2 + \frac{\gamma}{\gamma-1} - \frac{\gamma+1}{2(\gamma-1)} \frac{T_w}{T_{\infty}} \right) \right] \{ e^{-s^2 \sin^2 \theta} + \sqrt{\pi} s \sin \theta [1 + \text{erf}(s \sin \theta)] \} - \frac{1}{2} e^{-s^2 \sin^2 \theta} \right] \quad (36)$$

Where  $C_{acc}$  is the accommodation coefficient and  $\gamma$  is the specific heat ratio.

The Stanton number is therefore calculated as:

$$St_{fm} = \frac{Q_{fm}}{\frac{1}{2} \rho V_{\infty}^3} \quad (37)$$

### 7.2.3 Transitional

Similar to the aerodynamic coefficients, the transition region Stanton number is estimated using the SPL bridging formula described in *section 7.1.3*. Bridging coefficients are again determined from manual sensitivity analyses and comparisons to higher fidelity data.

The resulting Stanton number is used to compute the aerothermodynamic contribution of each non-occluded facet using *equation 31*.

## 8 Supersonic Module

This section describes the methods considered for use within the supersonic model for the calculation of aerodynamic conditions.

### 8.1 Aerodynamics

Supersonic conditions are considered for Mach numbers between one and five, and are characterised by the presence of shockwaves along the simulated geometry.

The first method considered was a shock inclination method. Initially, each geometry facet was assumed to have its own individual shock. With the removal of the unseen panel using the HSR algorithms, the shocks would be either normal shocks in the form of offset bow waves, or oblique shocks. The Rankine–Hugoniot relations were applied to calculate the pressure behind the shock, multiplied by the panel area to determine the force, then split into  $x$ ,  $y$  and  $z$  components.

To determine the type of shock, the maximum possible deflection for an oblique shock was defined. This was calculated using a minor modification of the Public Domain Aeronautical Software (PDAS) Fortran code [39] that calculates the maximum deflection angle,  $\theta$ , as a function of Mach number. A graph of the results of this calculation can be seen in *figure 29*.

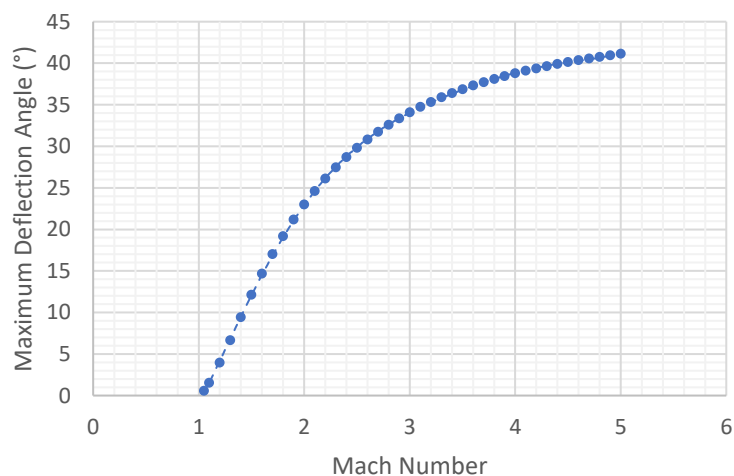


*Figure 29 - Maximum deflection angle against Mach number*

The trendline equation for this graph was used as the maximum value of panel deflection for the oblique shocks, using a 6<sup>th</sup> order best fit polynomial, with an  $R^2$  value of 0.9999.

Following this, the force on an individual panel was determined. The panel inclination was then found using the velocity vectors and the normal of the panel (for all panels not removed by the HSR algorithms).

Three panel inclination conditions were handled separately. For zero inclination (as for a panel completely parallel to the flow) drag, lift and sideslip forces were considered negligible.

If the panel inclination was greater than the maximum deflection angle for the specified flight Mach number, the panel would be subject to an offset bow shock, or normal shock. To, calculate the downstream conditions, the equations detailed by John Anderson [40] for inviscid compressible flow were implemented. Knowing the ratio of specific heats and the Mach number from the Atmospheric module, the post-shock conditions were found using the following relationships:

$$Ma_2 = \sqrt{\frac{1 + \left(\frac{\gamma-1}{2}\right) Ma_1^2}{\gamma Ma_1^2 - \left(\frac{\gamma-1}{2}\right)}} \quad (38)$$

$$\frac{P_2}{P_1} = 1 + \frac{2\gamma}{\gamma+1} (M_1^2 - 1) \quad (39)$$

If the panel inclination was less than the maximum deflection for an oblique shock wave, the panel was considered to be subject to an oblique shock. Using the oblique shock calculations, the shock wave angle, a function of both Mach number and deflection angle, usually read off a  $\theta - \beta - M$  graph, was determined using a numerical method.

There are several iterative and direct methods to calculate the shock wave angle. PASTA 1.2 initially used the formulation proposed by Dou and Teng [41], which approximates the shock wave angle as:

$$\beta = \frac{1}{\sqrt{M_1^2 - 1}} + \frac{\gamma+1}{4} \frac{M_1^2}{4(M_1^2 - 1)^2} \theta + \left(\frac{\gamma+1}{4}\right)^2 \left[ \frac{M_1^8 + 4M_1^6}{(M_1^2 - 1)^{3.5}} \theta^2 \right] \quad (40)$$

The oblique shock relations can then be used to calculate downstream conditions. The normal Mach number is calculated using:

$$M_{1n} = M_1 \sin \beta \quad (41)$$

This is then input to the normal shock equation as before, and the normal component input to the pressure formula, *equations 38 and 39* respectively.

Once the downstream pressure of each type of shock was known, this pressure was translated into a force by multiplying the pressure by the area of each panel.

$$F = PA \quad (42)$$

The location of this force was then assumed, since the panels are generally small, to act as a point on the centre of each panel, parallel to normal vector. This unit vector was reversed, then multiplied by the magnitude of the force.

This vector was then split into its  $x$ ,  $y$  and  $z$  components, for the drag, side and lift forces respectively. The total magnitude of the force in each direction was therefore taken to be the sum of all forces in a particular direction, with the coefficients calculated using *equation 43*.

$$C_F = \frac{F}{\frac{1}{2} \rho V_\infty^2 S_{ref}} \quad (43)$$

This method proved to be suitable for some external shapes but was completely inaccurate when considering any internal geometric features, such as intake ducts on aircraft. Therefore, an alternative method had to be considered.

The second method considered was the Tangent Cone Method. This method works on the assumption of a single shock at the front face of the body, then interpolates this shock based on the angle of the cone [42]. This method was simplified to determine its suitability for use with the test geometries used within this study.

The method chosen to be used within PASTA 1.2 uses the pressure coefficient of each panel rather than the shock assumption to determine aerodynamic conditions. A NASA report on an Improved Tangent Cone method was used as the basis of the method [43]. The two equations used for the pressure coefficient can be seen below. *Equation 44* is the Edwards Corrected Tangent Cone, and *equation 45* is the 2<sup>nd</sup> order Slender Body and Hammitt/Murthy formulation:

$$C_p = \frac{48M_{ns}^2 \sin^2 \theta}{23M_{ns}^2 - 5}, \quad M_{ns} = (0.87M_\infty - 0.544) \sin \theta + 0.53 \quad (44)$$

$$C_p = \frac{P_\infty}{\frac{1}{2} \rho_\infty V_\infty^2} \left[ \frac{\left( \frac{2\gamma}{\gamma+1} M_\infty^2 \sin^2 \beta - \frac{\gamma-1}{\gamma+1} \right)}{\left( 1 + \frac{\gamma M_\infty^2 (\beta - \theta)^2 \cos^2 \beta}{1 + \frac{\gamma-1}{2} M_\infty^2 \sin^2 \beta} \right)} \right] \quad (45)$$

The trends of both of these equations with Mach number can be compared with several other solutions. It can be seen in *figure 30* that, particularly at lower Mach numbers, the trend is towards an infinite pressure coefficient. As such, a more complicated formulation is needed over the hypersonic solution.

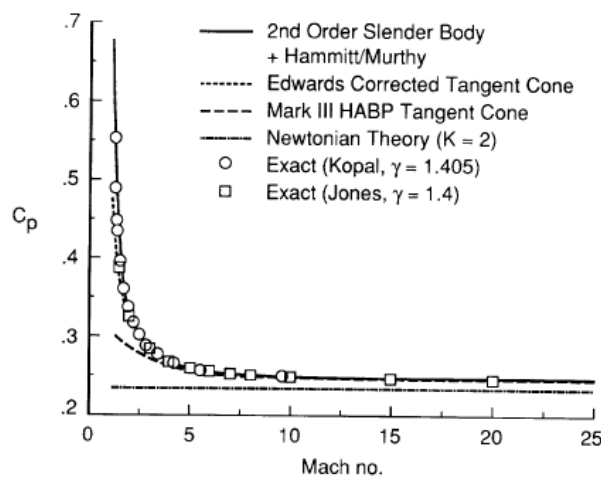


Figure 30 - Pressure coefficient against Mach number

Each of these equations were programmed and used to calculate the lift, drag and side force as in the hypersonic module. Results are displayed in *section 11.2*.



## 9 Sub-Sonic Module

PASTA 1.2 defines subsonic flow where the freestream Mach number is the range 0 to 0.8.

### 9.1 Aerodynamics

The accurately modelling a complex 3D flow field requires significant computational load. To obtain quick, accurate analysis results, the ‘potential flow’ model is used. This model contains four fundamental assumptions to simplify the flow conditions [44]:

1. **The flow is incompressible**
2. **The flow is inviscid**
3. **The flow is irrotational**
4. **The flow is steady**

Using these assumptions, the potential flow equation is derived from the continuity principles [45]:

$$\frac{\partial \rho}{\partial t} + \nabla \cdot \rho \mathbf{v} = 0 \quad (46)$$

Applying the steady flow assumption:

$$\nabla \cdot \rho \mathbf{v} = 0 \quad (47)$$

Equation 47 can be separated into two terms:

$$\mathbf{v} \cdot \nabla \rho + \rho (\nabla \cdot \mathbf{v}) = 0 \quad (48)$$

Applying the incompressible flow assumption, the equation will simplify to:

$$\nabla \cdot \mathbf{v} = 0 \quad (49)$$

The scalar velocity potential function ( $\phi$ ) can be used to represent an irrotational flow. The flow velocity can now be defined as the gradient of the velocity potential function:

$$\mathbf{v} = \nabla \phi \quad (50)$$

The vorticity of the flow is defined as the curl of the flow velocity vector,  $\mathbf{v}$ , mathematically expressed as:

$$\text{curl}(\mathbf{v}) = \nabla \times \mathbf{v} \quad (51)$$

As the flow is irrotational and the vorticity is zero:

$$\text{curl}(v) = \nabla \times \nabla \phi = 0 \quad (52)$$

The curl of a vector gradient is a known vector identity and is always equal to zero. Therefore, the potential flow model can only be valid when the flow is irrotational. This condition also confirms that the potential flow model should be limited to inviscid flow applications, as viscous effects in the model would introduce vorticity into the flow [45].

By combining *equation 49* and *50*, the governing equation for the potential flow model, Laplace's equation, is found:

$$\nabla^2 \phi = 0 \quad (53)$$

As Laplace's equation is linear, the principle of superposition can be applied. Therefore, a flow field can be constructed by combining a number of individual solutions to Laplace's equation [46]. These individual solutions, known as 'singularities' are algebraic functions which satisfy Laplace's equation. The most common singularities are the point source and doublet, shown in *figure 31* [47].

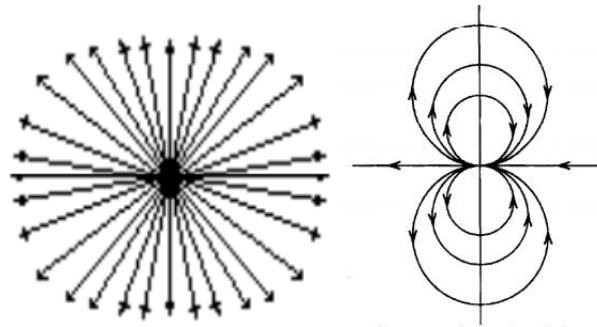


*Figure 31 – Point source (left) and Doublet (right)*

Using panel codes, these singularities can be distributed across the panels on the surface of the body and combined together to accurately model the flow field.

The Boundary Element Method (BEM) is used to compute these flow solutions. The BEM is a numerical method for solving linear partial differential equations which are formulated in the boundary integral form. There are two methods for implementing the Boundary Element Equation, direct and indirect methods. The indirect method, considered here for integration into PASTA 1.2, implements discrete singularity solutions, integrated over the analysis surface. This method is commonly used in the aerospace industry [48]. To apply this method, a Boundary Integral Equation (BIE) must be formulated. The full derivation of the BIE is presented by Katz and Plotkin [49].

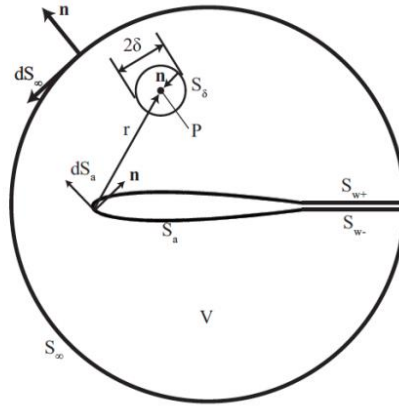


Figure 32 – BIE formulation boundaries

An important part of the derivation of the BIE is the use of Green's theorems to convert volume integrals into surface integrals.

Following through the derivation outlined in Katz and Plotkin, the final form of the BIE is given as [49]:

$$\phi(P) = \frac{1}{4\pi} \int_{S_a} \left[ \frac{1}{r} \nabla(\phi - \phi_{in}) - (\phi - \phi_{in}) \nabla \frac{1}{r} \right] \cdot \mathbf{n} ds - \frac{1}{4\pi} \int_{S_w} \left[ \phi \mathbf{n} \cdot \nabla \frac{1}{r} dS \right] + \phi_{\infty}(P) \quad (54)$$

Using *equation 54* the total potential at any arbitrary point in the domain can now be found by summing the influence of each individual panel.

*Equation 54* provides a value for  $\phi(P)$  as a function of the potential at the boundary and the normal derivative of the potential at the boundary. It follows that to determine a solution for the total potential at point  $P$ , these boundary values must be found. This can be achieved by analysing an arbitrary segment of the boundary  $S_a$  shown in *figure 33*:

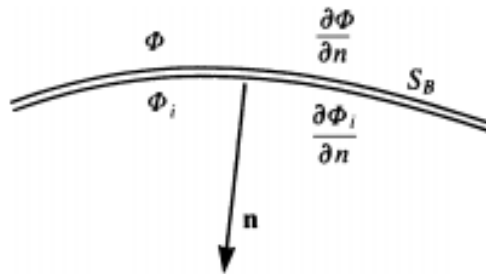


Figure 33 – Velocity potential near the boundary

The difference between the external and internal potential is defined as:

$$-\mu = \phi - \phi_{in} \quad (55)$$

This expression is implemented when considering the ‘doublet’ singularity shown in *figure 31*.

The difference between the normal derivative of the external and internal potentials is defined as:

$$-\sigma = \frac{\partial \phi}{\partial n} - \frac{\partial \phi_{in}}{\partial n} \quad (56)$$

This expression is implemented when considering the ‘point source’ singularity shown in *figure 31*.

The negative sign shown in both equation is a result of the normal vector pointing into the boundary. Using these two equations the BIE can be rewritten as:

$$\phi(P) = \frac{1}{4\pi} \int_{S_a} \left[ -\frac{1}{r} \sigma + \mu \frac{\partial}{\partial \mathbf{n}} \right] dS + \frac{1}{4\pi} \int_{S_w} \left[ \mu \frac{\partial}{\partial \mathbf{n}} \frac{1}{r} \right] dS + \phi_{\infty}(P) \quad (57)$$

The above equation is better expressed in summation terms for the discrete point source and doublet elements.

$$\phi(P) = \frac{1}{4\pi} \left[ \sum_{k=1}^{Pan_d} \mu_k \frac{\partial}{\partial \mathbf{n}} \left( \frac{1}{r_k} \right) - \sum_{l=1}^{Pan_s} \frac{\sigma_l}{r_j} \right] + \phi_{\infty}(P) \quad (58)$$

The individual influence of each point source and doublet element can now be evaluated using *equations 59* and *60* respectively.

$$\phi_{pointsource} = -\frac{\sigma}{4\pi r} \quad (59)$$

Evaluating the doublet singularity influence is more difficult due to the partial derivative term inside the summation. A detailed derivation is outlined in Katz and Plotkin yielding a final solution [49];

$$\phi_{doublet} = -\frac{\mu \cdot r}{4\pi r^3} \quad (60)$$

An influence function can now be generated for any geometric body by integrating these influence terms over the panels on the body to generate an accurate model for the flow field.

To determine the strengths of each singularity element on the surface, a number of boundary conditions must be enforced on the body submerged in the potential flow.

The ‘far field’ boundary condition requires that the perturbed velocity potential be equal to zero as the relative position vector,  $r$ , tends to infinity. This condition is satisfied by the derivation of the singularity elements and does not need to be evaluated numerically [45].

The Dirichlet boundary condition is used for the indirect implementation of the BEM [46]. The velocity at any point inside the boundary  $S_o$  is assumed equal to zero. As shown by Lamb, this condition suggests that the velocity potential inside said boundary must be constant [50]. If this constant value is selected to be equal to the freestream velocity potential, and assuming the collocation points for the panels are placed just inside the boundary surface, *equation 58* simplifies to;

$$\frac{1}{4\pi} \left[ \sum_{k=1}^{Pan_d} \mu_k \frac{\partial}{\partial \mathbf{n}} \left( \frac{1}{r_k} \right) - \sum_{l=1}^{Pan_s} \frac{\sigma_l}{r_l} \right] = 0 \quad (61)$$

To determine a unique solution to *equation 61*, the source strengths are described as

$$\sigma = \mathbf{n} \cdot \mathbf{v}_\infty \quad (62)$$

This method is further detailed in *section 14.3.1*.

The Kutta condition is described as “a body with a sharp trailing edge which is moving through a fluid will create about itself a circulation of sufficient strength to hold the rear stagnation point at the trailing edge” [51]. The stagnation point held at the trailing edge of the body corresponds to the physical reality of attached lifting flow [45]. A visual representation of the Kutta condition is shown in *figure 34*.

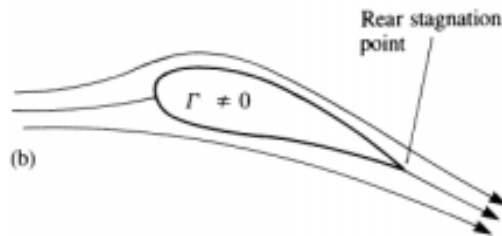


*Figure 34 – Visual representation of the Kutta condition*

A method for calculating the pressure distribution using the potential flow theory described in this section is outlined in *section 14.3.1*.

## 10 Output Module

PASTA 1.2 outputs the simulation results in 3 separate formats:

### 1. Console output

On completion of each simulation, both the primary inputs and outputs are displayed on the console screen. This allows the immediate usage of computed data, as well as the ability to check simulation parameters.

### 2. Text file

Results are additionally saved to the program directory, in the form of a simple text file. The text file includes an input summary as well as the simulation results. The text file is named according to the simulation completion time, and the name of the geometry being analysed, to allow for quick access and automatic file sorting.

### 3. VTK file

Pressure coefficient and heat transfer distribution data is included in a VTK file (an abbreviation of Visualisation ToolKit). VTK files allow for the viewing and postprocessing of distribution data across a geometry, in open source visualisation software such as Paraview [52]. This allows for stagnation points to be located and analysed, areas of maximum heat transfer and pressure coefficient to be viewed with respect to the overall geometry, and the effects of additional complex geometric features to be determined. Aerothermodynamic heating is considered to be negligible below hypersonic speeds, and so are not included in supersonic/subsonic outputs. As for the text file, the VTK output file is named according to the time of simulation completion, and the name of the analysed geometry.

## 11 Validation

To determine the accuracy of the models and formulation used within PASTA 1.2, a number of test cases are presented. The results obtained using PASTA 1.2 are compared against results obtained from a variety of other test methods, including high fidelity CFD and DSMC simulations in addition to recorded experimental flight data.

To compare the performance of PASTA 1.2 with respect to another low-fidelity local surface inclination implementation, results computed using FOSTRAD 2.0 have been included. The FOSTRAD 2.0 code has been provided by the Mechanical and Aerospace Engineering department at the University of Strathclyde.

### 11.1 Hypersonic

#### 11.1.1 Aerodynamics

##### SPHERE

The aerodynamics estimated by PASTA 1.2 are first tested using a simple spherical geometry. The sphere has been analysed by high fidelity DSMC and CFD simulation methods [53], in addition to the lower fidelity LSI implementation presented by FOSTRAD 2.0. Input conditions for the first sphere are shown in *table 8*:

| Input                  | Value           |
|------------------------|-----------------|
| Free Stream Velocity   | 7500m/s         |
| Altitude               | 90-200km        |
| Mach Number            | 10-27           |
| Reference Length       | 1.6m            |
| Reference Area         | $\pi 0.8^2 m^2$ |
| Nose Radius            | 0.8m            |
| Wall Temperature       | 350K            |
| Free Steam Temperature | 200K            |

*Table 8 - Aerodynamic Test Case (Sphere)*

Figure 31 shows the comparison between the DSMC results presented by Dogra et al. [53], the results given by FOSTRAD 2.0, and the results given by PASTA 1.2.

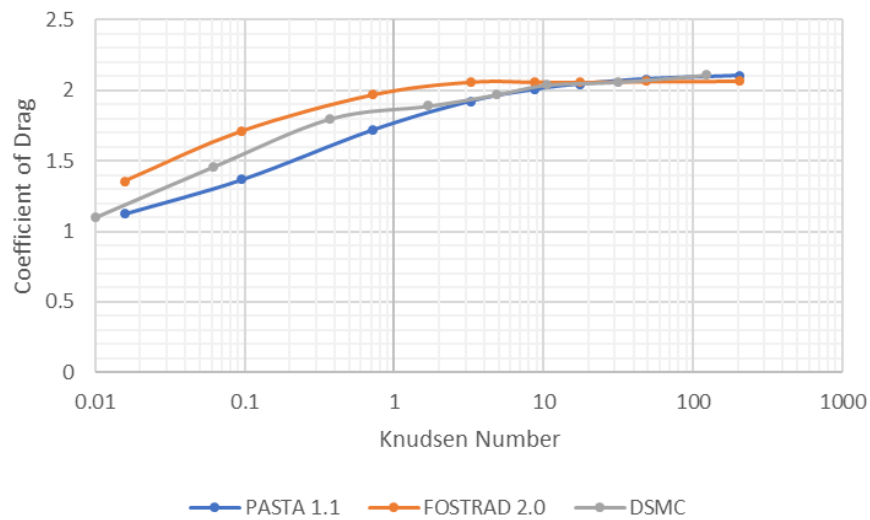


Figure 31 - Aerodynamic Test Case (Sphere)

PASTA 1.2 appears to match the DSMC results well in the free-molecular regime, while maintaining a good degree of accuracy within the high-transitional regime similar to that of FOSTRAD 2.0.

The pressure coefficient surface distribution for the test case at 160km altitude is shown in figure 32:

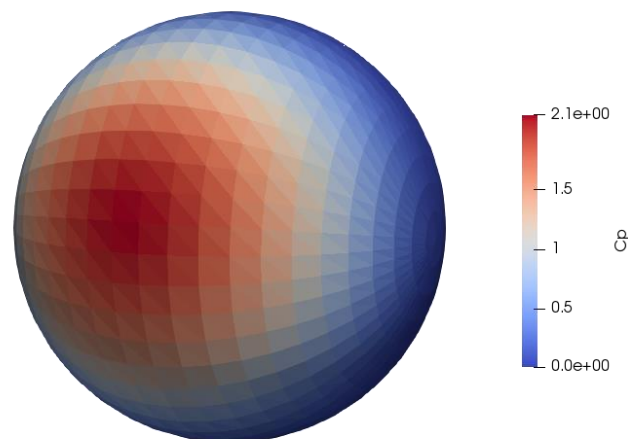


Figure 32 - Aerodynamic Test Case (Sphere -  $C_p$ )



## ORION

The Orion Multi-Purpose Crew Vehicle is the next generation of crewed spacecraft currently under development by NASA [54] [55]. Intended to carry a crew of four astronauts on Low Earth Orbit (LEO), lunar and Mars missions, Orion will launch on board NASA's Space Launch System (SLS), also under development.

Orion has completed one unmanned test flight, Exploration Test Flight 1 (2014), and will begin crewed flight testing in the early 2020s.

The geometry used to simulate the re-entry of the Orion capsule is shown in *figures 33 and 34* [56]. Test case input conditions are shown in *table 9*:

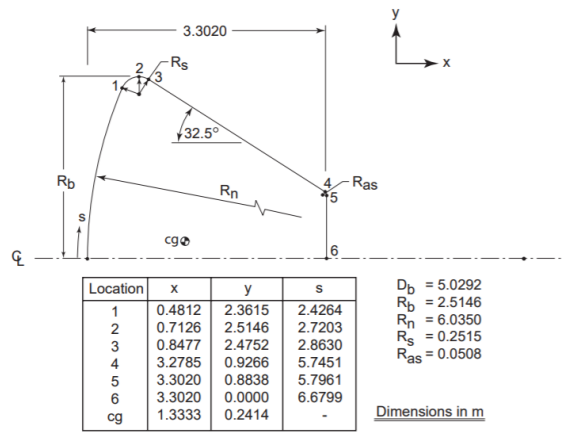


Figure 34 - Orion MPCV Dimensions [56]

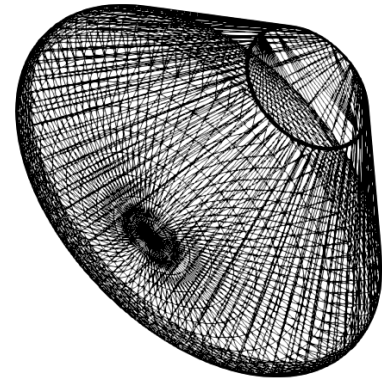


Figure 33 - Orion Stereolithographic model

| Input                | Value                |
|----------------------|----------------------|
| Free Stream Velocity | 7600m/s              |
| Altitude             | 75-250km             |
| Angle of Attack      | -26°                 |
| Reference Length     | 5.0292m              |
| Reference Area       | 19.865m <sup>2</sup> |
| Nose Radius          | 6.035m               |
| Wall Temperature     | 1630 – 144K          |

Table 9 - Aerodynamic Test Case (Orion MPCV)

Orion aerodynamics have been compared with DSMC and CFD data reported by Moss et al. [56], in addition to data obtained using FOSTRAD 2.0.

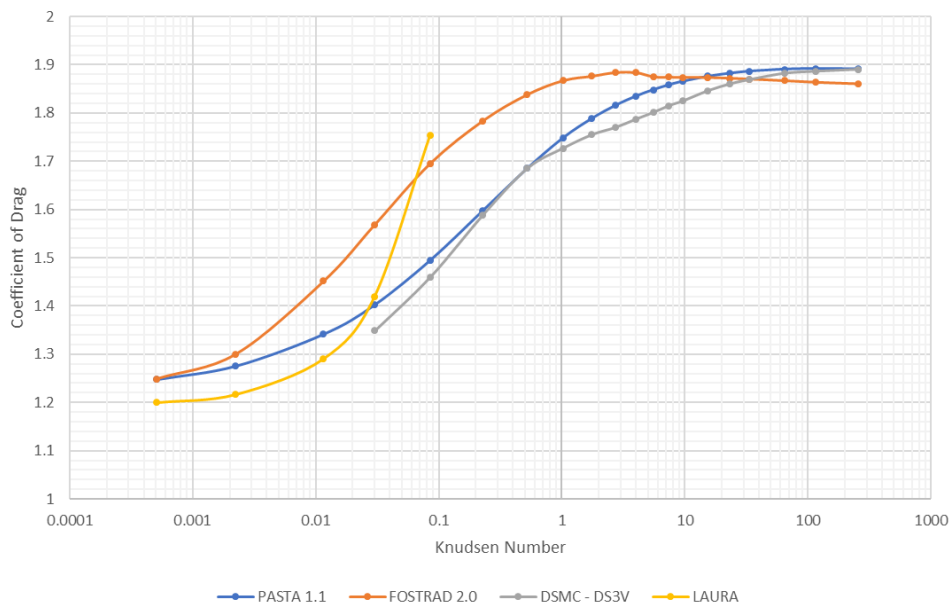


Figure 35 - Aerodynamic Test Case (Orion MPCV - Drag)

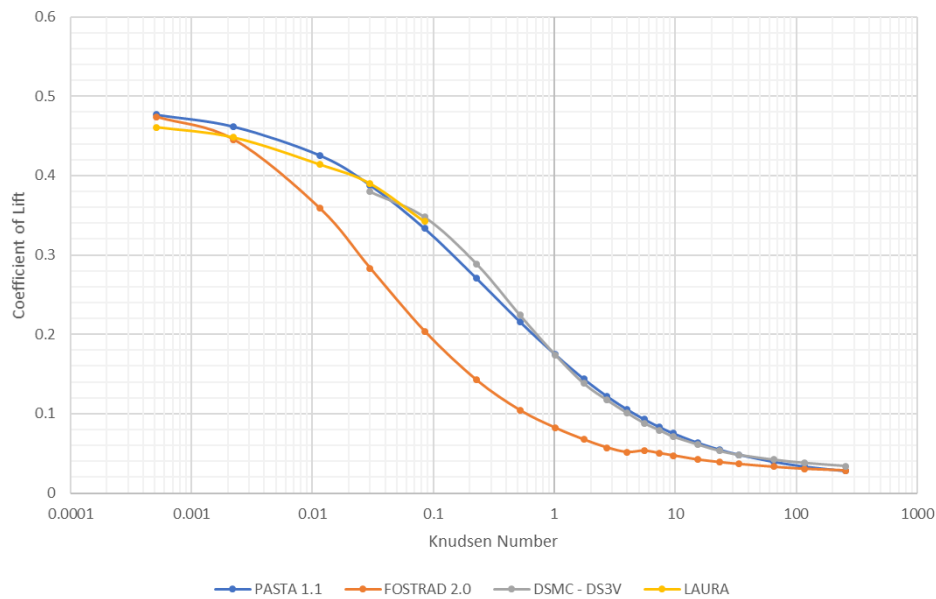


Figure 36 - Aerodynamic Test Case (Orion MPCV - Lift)

PASTA 1.2 can be seen to closely match the DSMC and CFD results from free molecular to low transitional flow regime. This test case shows a significant improvement over the FOSTRAD 2.0 implementation.

Figure 37 shows the surface distribution of the pressure coefficient for the test case at 110km altitude.

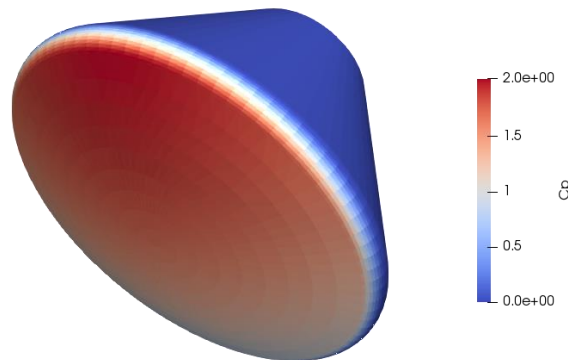


Figure 37 - Aerodynamic Test Case (Orion MPCV - Cp)

## STS ORBITER

The NASA Space Transportation System was a reusable space craft developed as part of the Space Shuttle Program after the conclusion of the Apollo program [57]. Five STS Orbiters were built to complete 135 missions from 1981 to 2011, including the launch of numerous satellites, interplanetary probes, the Hubble Space Telescope and resupply/maintenance to the International Space Station.

The stereolithographic geometry used by PASTA 1.2 to simulate the STS flight conditions on re-entry is shown in *figure 38*:

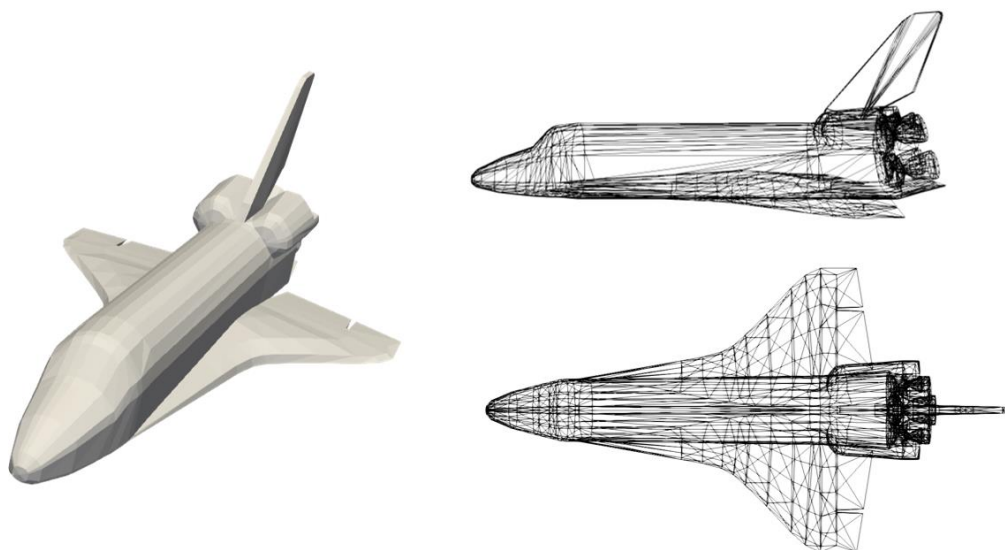


Figure 38 - STS Orbiter Stereolithographic Model

The aerodynamics estimated using PASTA 1.2 is compared to the values obtained using FOSTRAD 2.0, DSMC and wind tunnel simulations, as well as flight data collected from the first 10 STS flights [58] [59] [60].

A summary of the simulation conditions is shown in *table 10*:

| Input                | Value                 |
|----------------------|-----------------------|
| Free Stream Velocity | 7500m/s               |
| Altitude             | 100-170km             |
| Angle of Attack      | 40°                   |
| Reference Length     | 12.06m                |
| Reference Area       | 249.909m <sup>2</sup> |
| Nose Radius          | 0.7196                |
| Wall Temperature     | 300K                  |

Table 10 - Aerodynamic Test Case (STS Orbiter)

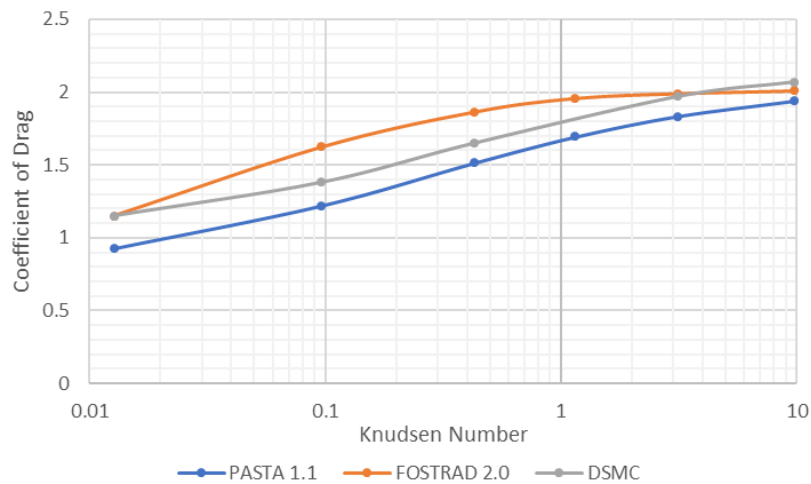


Figure 39 - Aerodynamic Test Case (STS Orbiter - Drag)

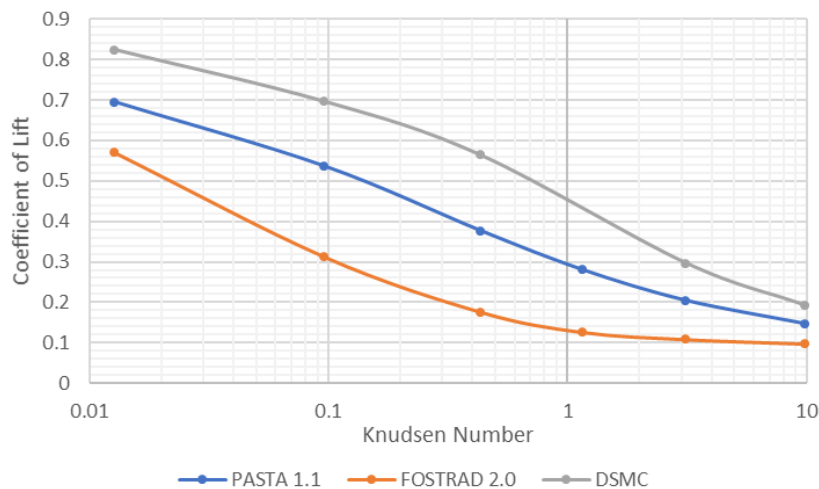


Figure 40 - Aerodynamic Test Case (STS Orbiter - Lift)

Figures 39 and 40 show the coefficients of drag and lift computed by PASTA 1.2 relative to DSMC and FOSTRAD 2.0 data. PASTA 1.2 appears to generally follow the form of the DSMC data but includes an error between 10 and 15% across the range of test cases considered. This error could be attributed to either the low resolution of the STS Orbiter geometry used for the simulation, as local surface inclination methods are known to encounter difficulties when considering a geometry comprised of long, thin facets.

Figure 41 shows the comparison between the Lift/Drag ratio estimated by PASTA 1.2 and FOSTRAD against experimental flight data obtained using HiRAP measurements on board the STS Orbiter during reentry [60].

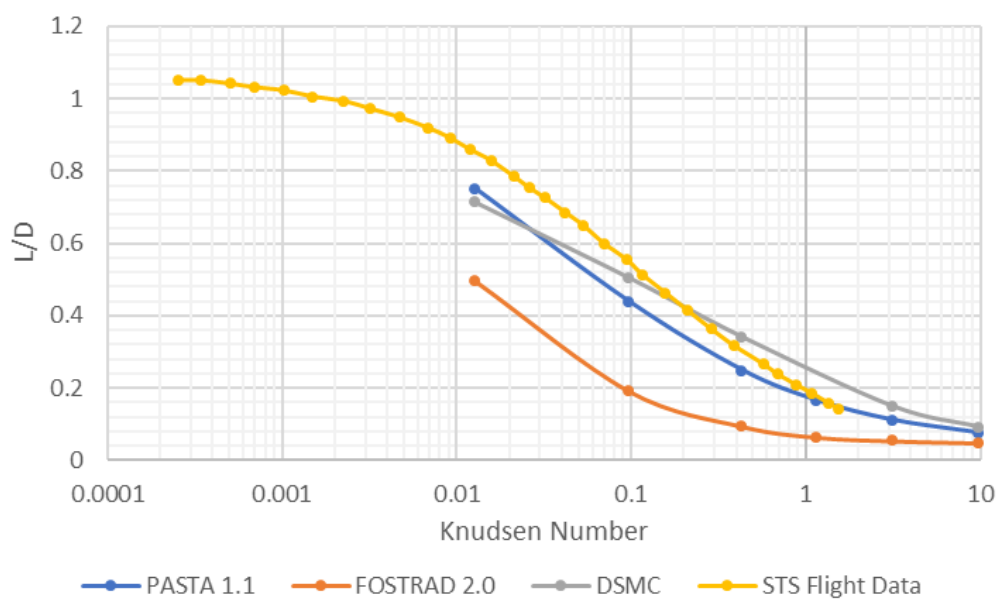


Figure 41 - Aerodynamic Test Case (STS Orbiter - Lift to Drag Ratio)

The surface distribution of pressure coefficient across the Shuttle Orbiter can be compared with the high fidelity DSMC results presented by Rault [58]. Figure 42 shows the comparison between DSMC and PASTA 1.2 for the Shuttle Orbiter at 170km altitude, with the remaining input conditions as listed in table 10. Similarly, figure 43 shows the same comparison between the two simulations at 110km altitude.

The DSMC and PASTA 1.2 results show a pressure concentration around the nosecone and wing leading edge. Both simulations show a strengthening of these concentrations at the lower altitude test case.

## PANEL METHOD AERODYNAMIC SIMULATION AND THERMAL ANALYSIS

BEN PARSONAGE

MORRIS KELLY

EUAN KERR

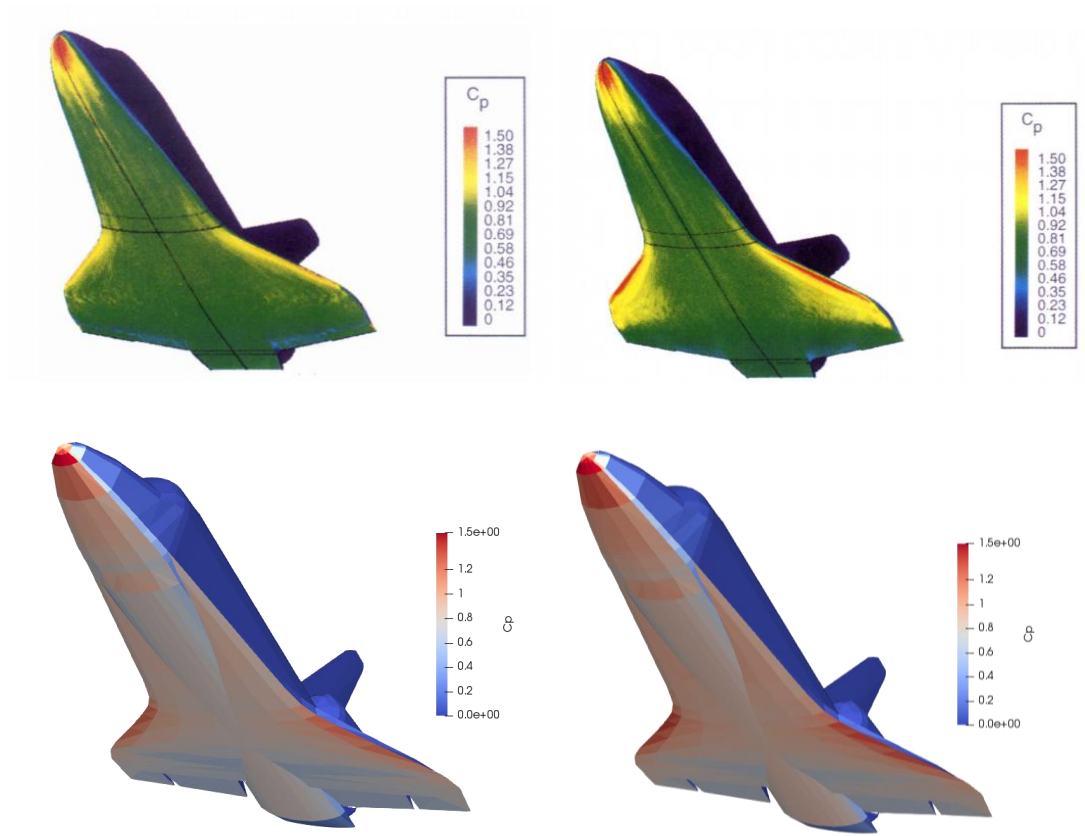


Figure 42 - Aerodynamic Test Case (STS Orbiter-170km) Figure 43 - Aerodynamic Test Case (STS Orbiter-110km)

### 11.1.2 Aerothermodynamics

#### SPHERES

The same spherical geometry as described in *section 11.1.1* is used to validate the aerothermodynamics computed by PASTA 1.2 against the DSMC results reported by Dogra et al [53].

Input conditions for this series of test cases is shown in *table 11*.

| Input                  | Value           |
|------------------------|-----------------|
| Free Stream Velocity   | 7500m/s         |
| Altitude               | 90-150km        |
| Mach Number            | 10-27           |
| Reference Length       | 1.6m            |
| Reference Area         | $\pi 0.8^2 m^2$ |
| Nose Radius            | 0.8m            |
| Wall Temperature       | 350K            |
| Free Steam Temperature | 200K            |

Table 11 - Aerothermodynamic Test Case (Sphere)

Figure 44 shows the heat transfer coefficient at the stagnation point of the geometry. The results show good agreement with DSMC in the free molecular regime but displays some divergence in the transitional regime. PASTA 1.2 seems to follow the general form of the DSMC results in the transitional regime, which suggests that the error results from the values of coefficients used in the transitional bridging function.

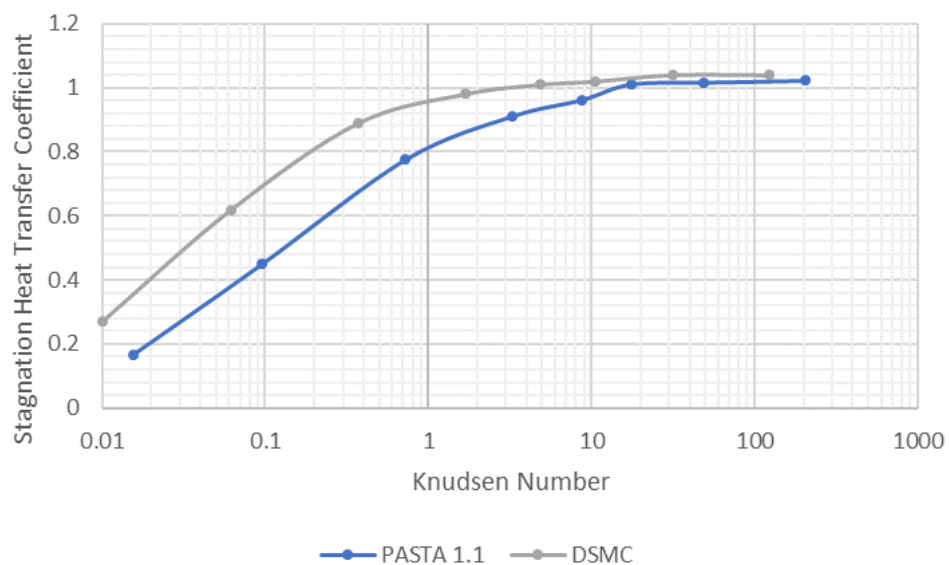


Figure 44 - Aerothermodynamic Test Case (Sphere)

Figure 45 shows the distribution of heat transfer and heat transfer coefficient across the spherical geometry for the free molecular test case at 160km ( $Kn = 48.9$ ).

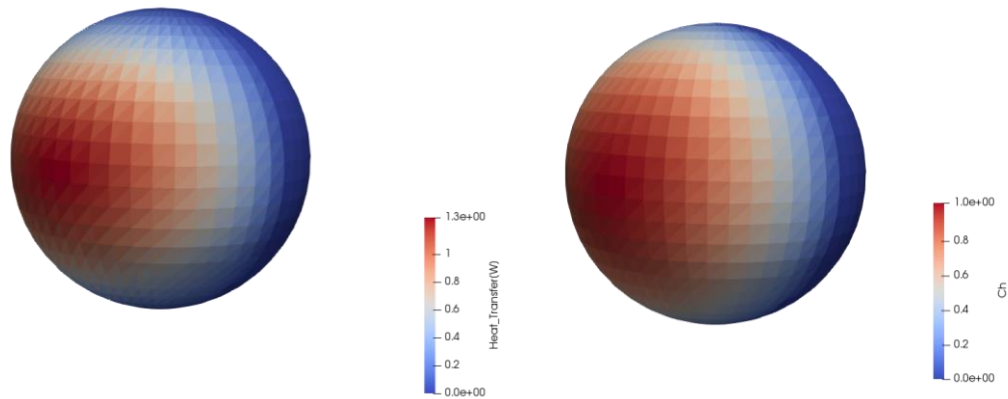


Figure 45 - Aerothermodynamic Test Case (Sphere)

## ORION MPCV

The Orion MPCV is again considered for the validation of PASTA 1.2 aerothermodynamics. In this section, the test cases and DSMC/CFD results are developed and described by Mehta et al [19]. The summarised input conditions for this series of test cases are shown in *table 12*.

| Input                | Value                |
|----------------------|----------------------|
| Free Stream Velocity | 7500m/s              |
| Altitude             | 50-130km             |
| Angle of Attack      | 0°                   |
| Reference Length     | 5.092m               |
| Reference Area       | 19.865m <sup>2</sup> |
| Nose Radius          | 6.035m               |
| Wall Temperature     | 1000                 |

Table 12 - Aerothermodynamic Test Case (Orion MPCV)

Figure 46 displays the results obtained by PASTA 1.2, DSMC and CFD simulations. The CFD and DSCMC simulations consider a chemically reacting gas, while the aerothermodynamic models used within PASTA 1.2 only consider gas dissociation, and not recombination. DSMC simulations assume a non-catalytic wall condition and include the Quantum Kinetic (QK)



method and the Total Collision Energy (TCE) method. The CFD simulations consider both non-catalytic (NC) and catalytic (SC) wall boundary conditions.

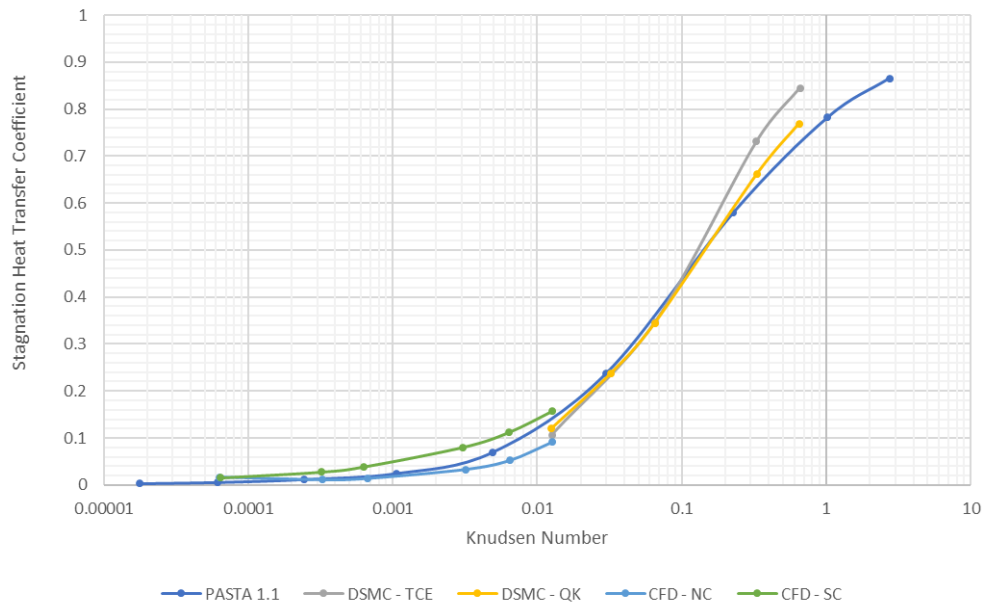


Figure 46 - Aerothermodynamic Test Case (Orion MPCV)

Realistic values for the stagnation point heat transfer coefficient would be expected to lie within the bounds of the catalytic and non-catalytic solutions [19]. It can be seen that this is achieved for the continuum regime, but not for the free molecular regime, and thus additionally for the upper portion of the transitional regime.

Figure 47 shows the distribution of heat transfer and heat transfer coefficient across the Orion MPCV geometry for the continuum regime test case at 60km ( $Kn = 6.18 \times 10^{-5}$ ).

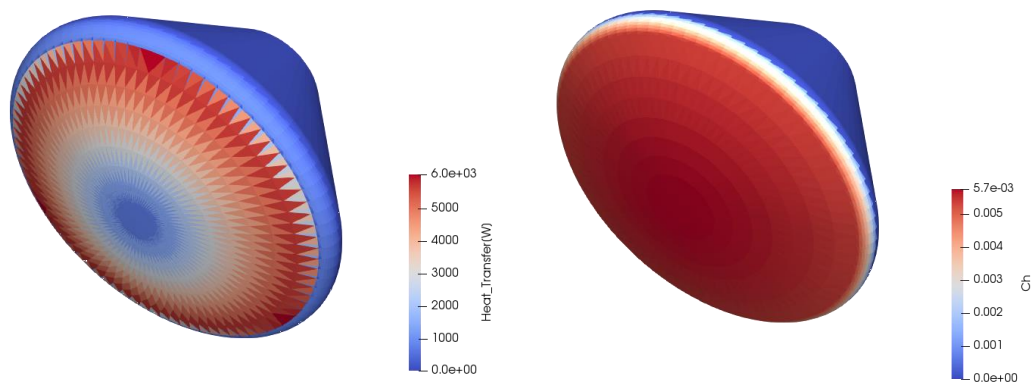


Figure 47 - Aerothermodynamic Test Case (Orion MPCV)

## STS ORBITER

The final aerothermodynamic validation case series involves the comparison between PASTA 1.2 and DSMC data described by Moss and Bird [61]. *Table 13* shows the summary of input conditions included in this test case series.

| Input                | Value                 |
|----------------------|-----------------------|
| Free Stream Velocity | 7500m/s               |
| Altitude             | 92.35-150km           |
| Angle of Attack      | 41.14-42.5°           |
| Reference Length     | 12.06m                |
| Reference Area       | 249.909m <sup>2</sup> |
| Nose Radius          | 1.296-1.362m          |
| Wall Temperature     | 921.5-300K            |

*Table 13 - Aerothermodynamic Test Case (STS Orbiter)*

*Figure 48* displays the stagnation point heat transfer coefficient computed using PASTA 1.2 and DSMC across the test case series. The results show good agreement between the two models, but do not include explicit representation of the continuum regime, other than the implicit agreement suggested by the transitional bridging dependency.

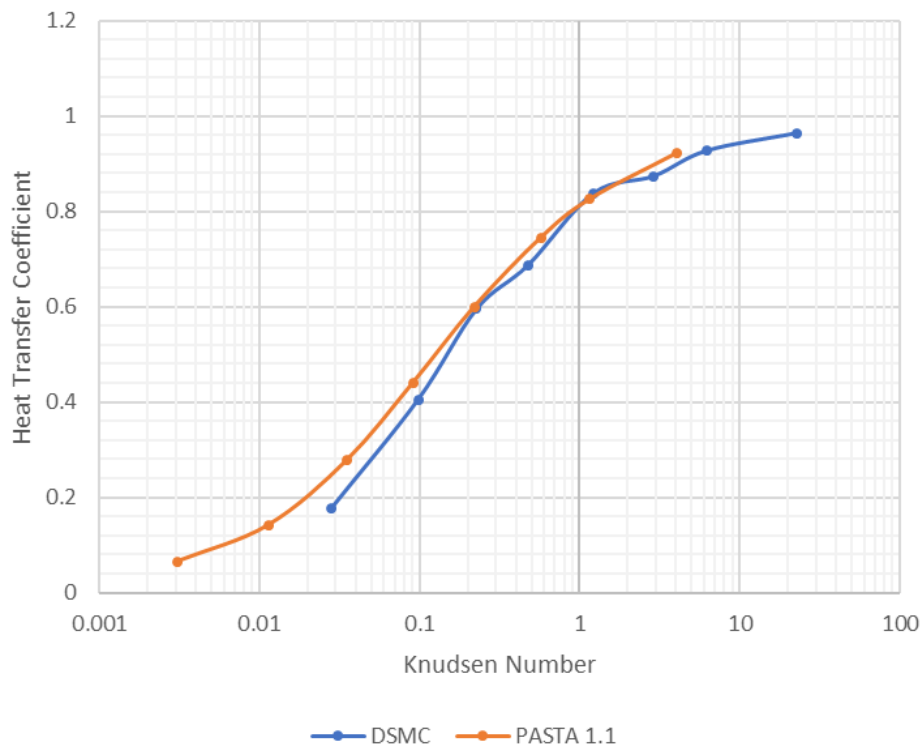


*Figure 48 - Aerothermodynamic test case (STS Orbiter)*

Figure 49 shows the distribution of heat transfer and heat transfer coefficient across the STS Orbiter geometry for the transitional regime test case at 130km ( $Kn = 1.1524$ ,  $T_w = 300K$ ).

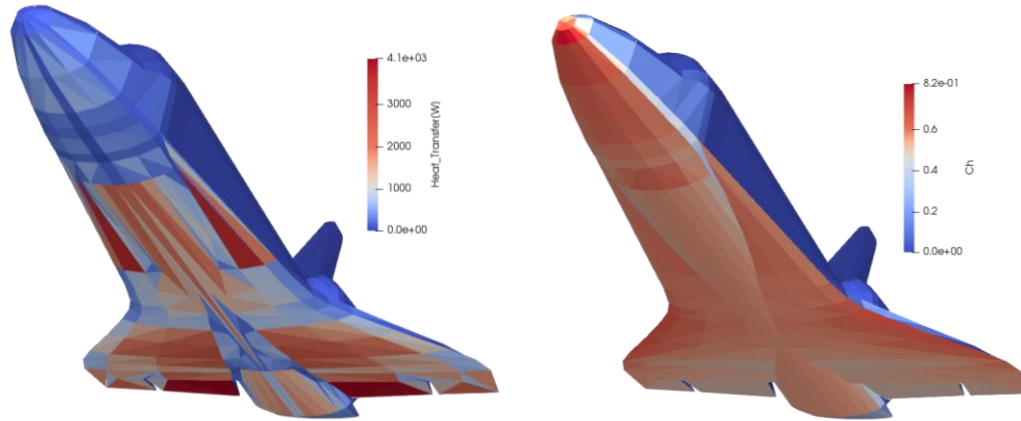


Figure 49 - Aerothermodynamic Test Case (STS Orbiter)

## 11.2 Supersonic

To validate the supersonic module, CFD simulations of a delta wing in were run using SU2. This proved to be problematic, as each simulation would continuously run for up to 5 days without converging to a feasible solution. This method was considered far too computationally expensive to offer feasible validation results within the time constraints of the project. The XB-70 supersonic jet was also attempted for use as a test case, however results appeared to be corrupted due to improperly constructed CAD models, and as such were neglected from consideration.

Validation tests were attempted using a diamond aerofoil, but again proved to be inconclusive due to the quality of CAD models used. Therefore, alternative case studies were chosen.

The first successful validation case covered was a perfectly spherical geometry of 1m diameter in supersonic flow, presented in a wind tunnel study by NASA. [62] The results included in this study, and the results obtained using PASTA 1.2, are shown in *figure 50* for zero angle of attack:

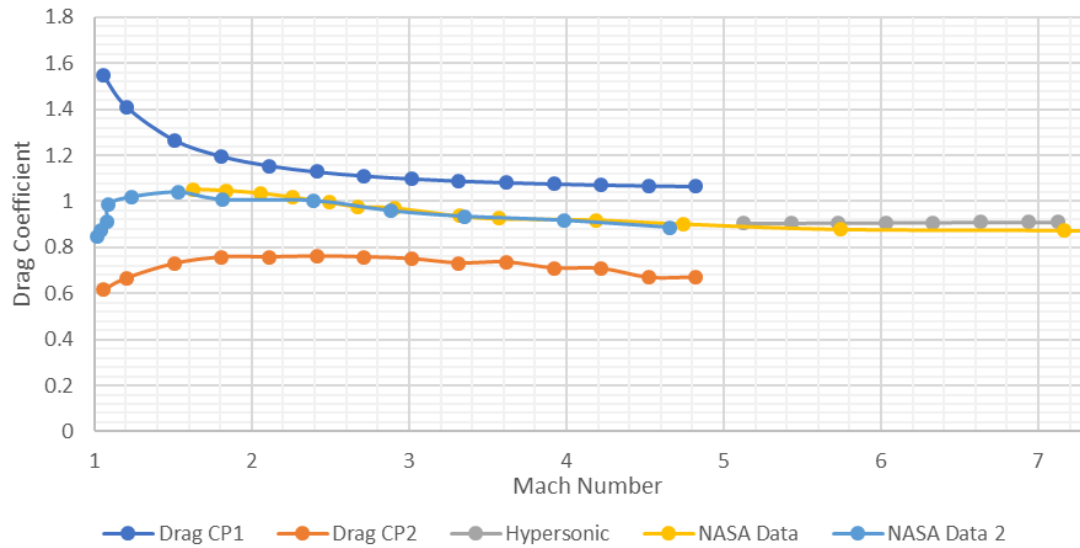


Figure 50 - PASTA 1.2 supersonic test case

In this, a comparison is made between the proposed *equation XX* and *XX* for the supersonic pressure coefficient. Hypersonic results are included for reference at Mach numbers greater than five. The first equation shows closer correlation to the data from around Mach 2 onwards, with the second following the trend better below this speed. Overall, the first formulation shows better agreement with the trend of the Mach number and as such is accepted as the valid formulation used within PASTA 1.2.

The distribution of the pressure coefficient computed using the supersonic module of PASTA 1.2 is shown below.

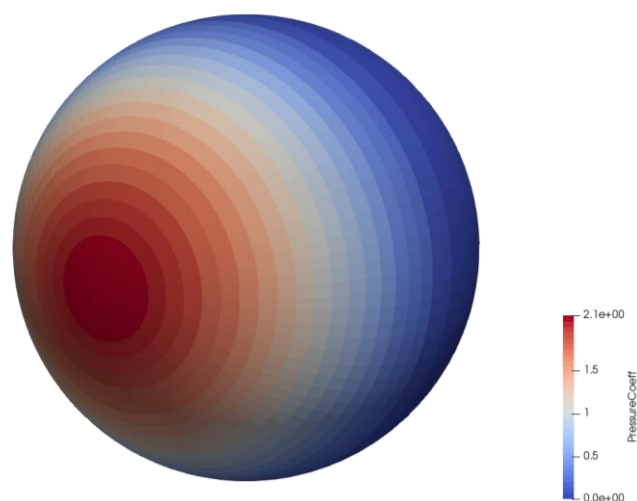


Figure 51 – PASTA 1.2 Supersonic Pressure Coefficient (2m Sphere)

Pressure distribution can also be shown for more complicated geometries, such as the STS Orbiter:

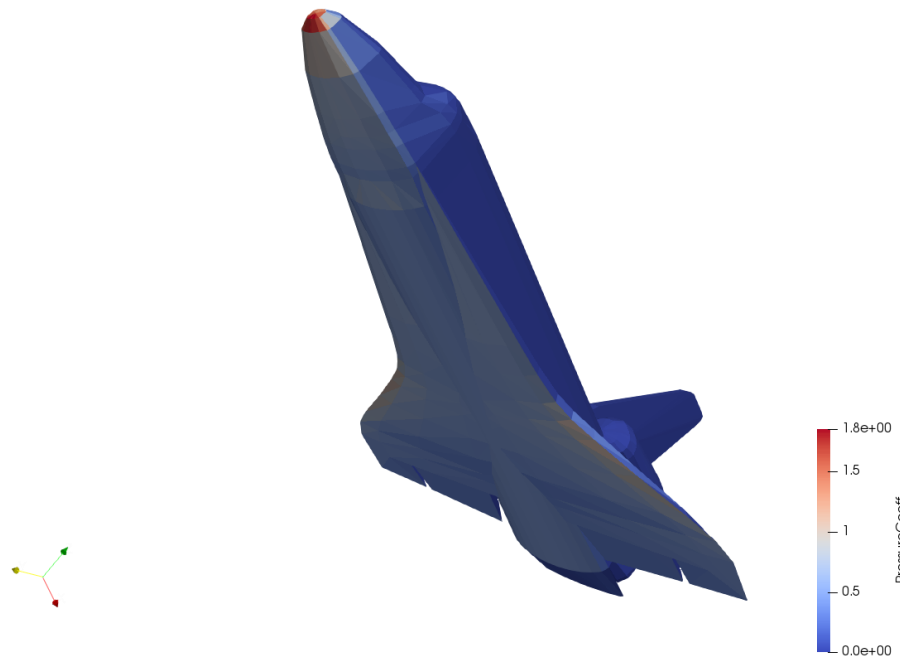


Figure 52 - Shuttle Orbiter Pressure Coefficient

The pressure distribution across the STS Orbiter, namely the concentration of maximum values around the nosecone and the leading edges of the wing section, agree with the results shown for the hypersonic test cases presented in *section 11.1.1*.

Figure 53 shows the relation between the STS orbiter analysed using both the supersonic hypersonic module. It can once again be seen that the supersonic module over-estimates the effect of pressure on surfaces, with a peak in force coefficient around the Mach 1 mark.

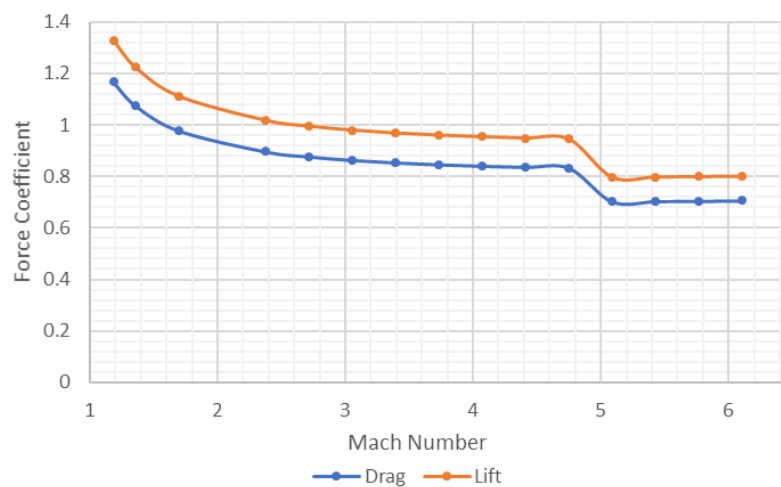


Figure 53 - Aerodynamic Test Case (STS Orbiter)

## 12 Applications

This section presents a demonstration of the usability of PASTA 1.2, by analysing a theoretical descent trajectory of a conceptual lifting body spaceplane.

### 12.1 CFASTT-1

CFASTT-1 is a theoretical spaceplane concept developed by the University of Strathclyde's Centre for Future Air Space Transportation Technology [63]. The concept is based on the Skylon vehicle currently under development at Reaction Engines.

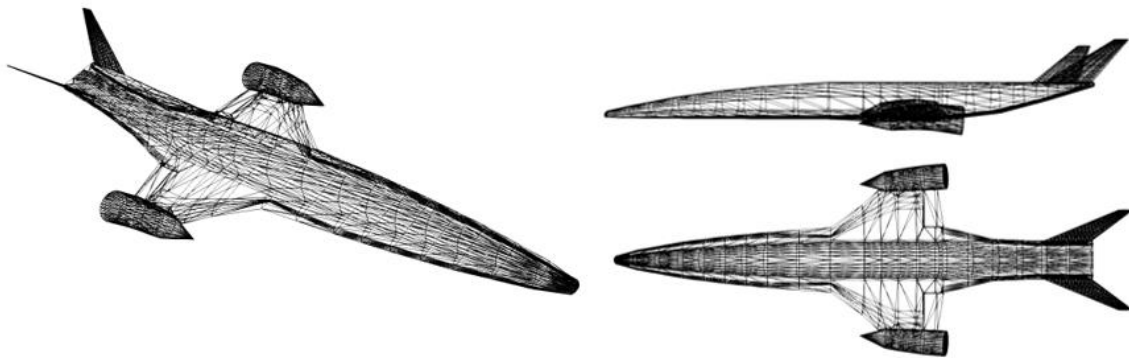


Figure 54 - CFASST-1 Stereolithographic Model

The usability of PASTA 1.2 can be demonstrated by considering a trajectory spanning all three velocity regimes, from subsonic to hypersonic.

The trajectory is established using the results presented by Toso et al [64].

| Time (s) | Altitude (km) | Velocity (m/s) | Angle of Attack (°) | Reference Area (m <sup>2</sup> ) | Wing Temperature (K) | Reference Length (m) | Nose Radius (m) |
|----------|---------------|----------------|---------------------|----------------------------------|----------------------|----------------------|-----------------|
| 0        | 120           | 7300           | 31.45               | 544.772                          | 600                  | 16                   | 1.08            |
| 250      | 82            | 7240           | 43.37               | 721.745                          | 1600                 | 16                   | 1.08            |
| 500      | 79            | 6940           | 48.43               | 786.626                          | 1640                 | 16                   | 1.08            |
| 750      | 79            | 6380           | 45.54               | 750.914                          | 1510                 | 16                   | 1.08            |
| 1000     | 76            | 5460           | 51.51               | 825.182                          | 1460                 | 16                   | 1.08            |
| 1250     | 60            | 2900           | 57.11               | 887.037                          | 1120                 | 16                   | 1.08            |
| 1500     | 34            | 1180           | 60.18               | 918.156                          | 640                  | 16                   | 1.08            |
| 1750     | 23            | 400            | 38.67               | 655.42                           | 285                  | 16                   | 1.08            |
| 2000     | 11            | 180            | 22.23               | 381.92                           | 240                  | 16                   | 1.08            |
| 2250     | 3             | 100            | 7.41                | 151.594                          | 270                  | 16                   | 1.08            |

Table 14 - CFASST - 1 Test Trajectory

# PANEL METHOD AERODYNAMIC SIMULATION AND THERMAL ANALYSIS

BEN PARSONAGE

MORRIS KELLY

EUAN KERR

Figures 55 to 59 show a visualisation of this trajectory in terms of altitude, velocity angle of attack and surface temperature respectively against time.

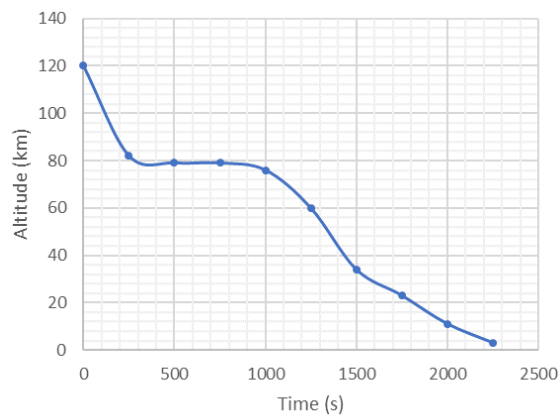


Figure 55 - CFASTT-1 Test Trajectory (Altitude)

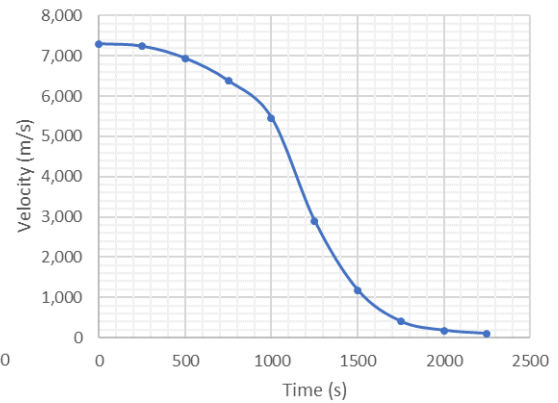


Figure 56 - CFASTT-1 Test Trajectory

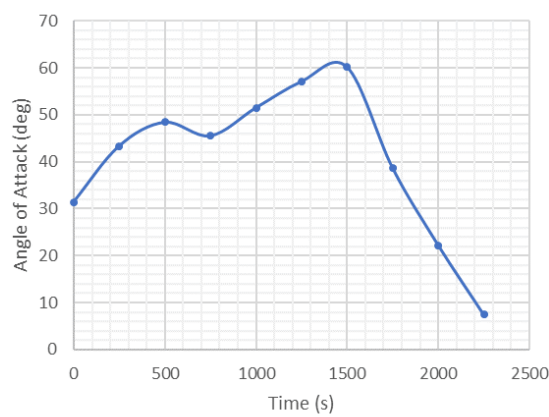


Figure 57 - CFASTT-1 Test Trajectory (Angle of Attack)

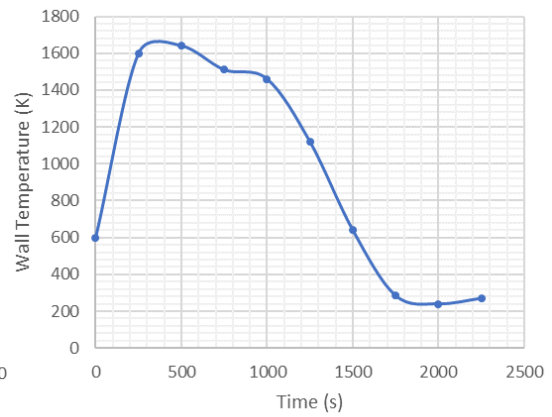


Figure 58 - CFASTT-1 Test Trajectory (Wall Temperature)

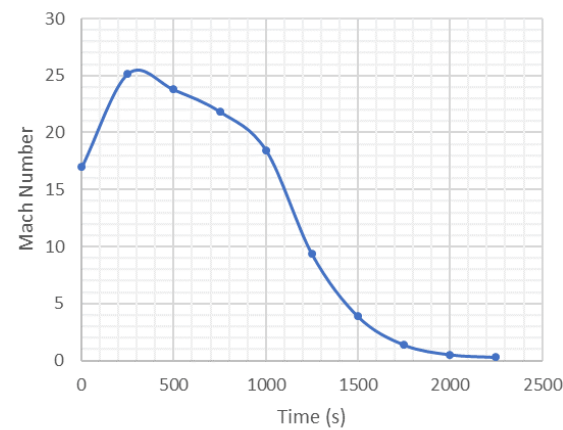


Figure 59 - CFASTT-1 Test Trajectory (Mach Number)

The coefficients of lift and drag through the duration of this trajectory are shown in *figures 60 and 61*. The results show an unsteady increase in coefficient of drag (after an initial decline) and a steady lift coefficient until 1250s. The subsequent decrease of drag coefficient and sharp increase in lift coefficient correspond to the Terminal Area Energy Management (TAEM), the interface between hypersonic re-entry at high angles of attack, and controlled supersonic flight.

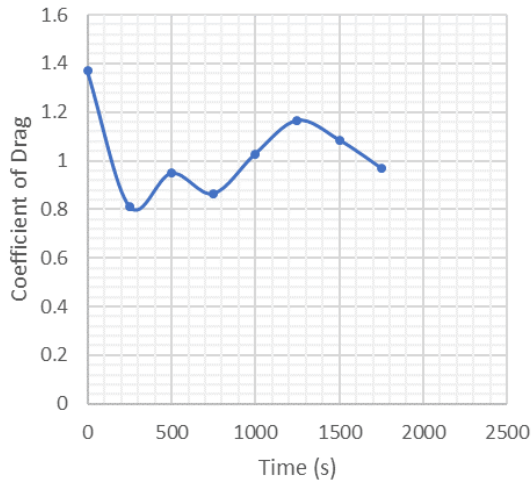


Figure 60 - CFASTT-1 Test Trajectory (Drag Coefficient)

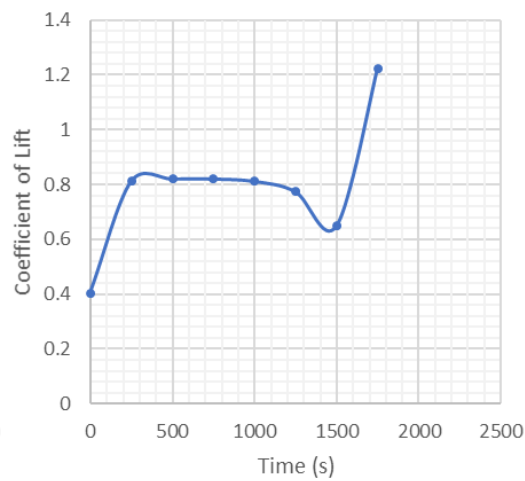


Figure 61 - CFASTT-1 Test Trajectory (Lift Coefficient)

The stagnation point heat transfer, at each time step of the trajectory is shown in *figure 63*. The results show maximum stagnation point heat transfer occurring at 500s, corresponding to the flattening period displayed in the trajectory profile, used to dissipate excessive heat transfer. Heat transfer levels are shown to diminish to negligible levels as the vehicle transitions to controlled supersonic flight.

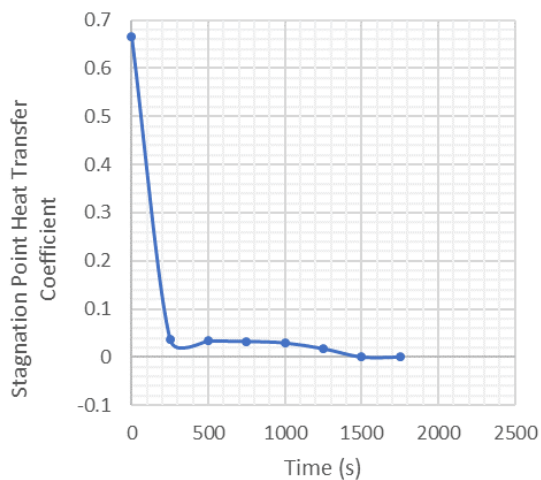


Figure 62 - CFASTT-1 Test Trajectory ( $Ch$ )

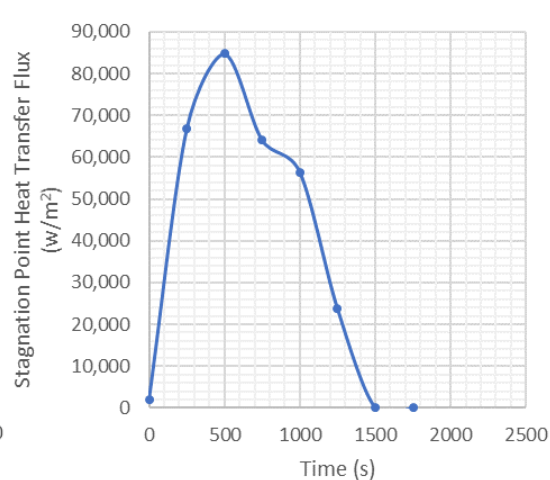


Figure 63 - CFASTT-1 Test Trajectory ( $Q$ )



The distributions of pressure coefficient, heat transfer coefficient and total heat transfer at the point of maximum heating (500s) are shown in *figures 64 to 66*.

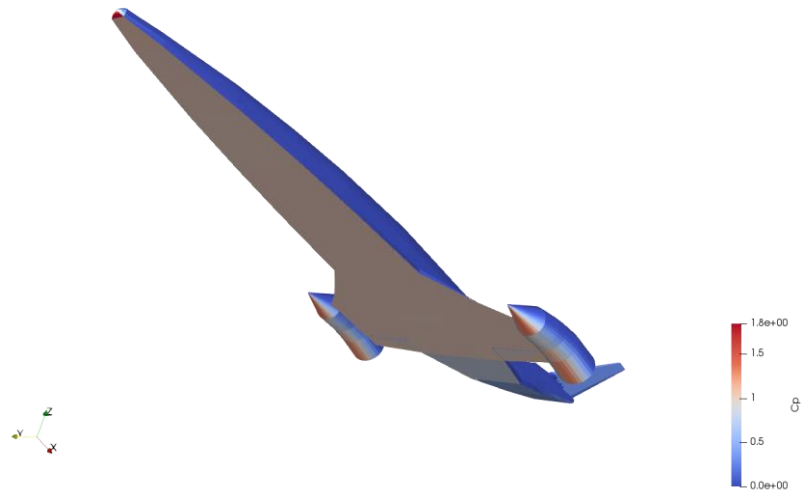


Figure 64 - CFASTT-1 Test Trajectory ( $C_p$ )

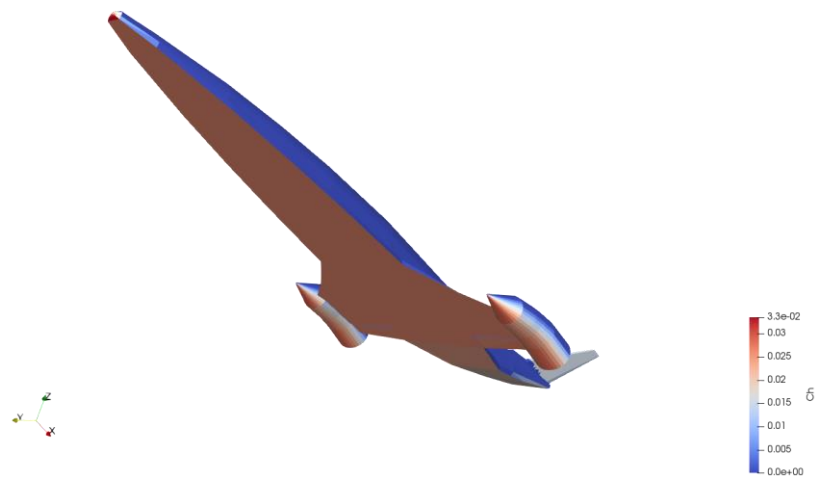


Figure 65 - CFASTT-1 Test Trajectory ( $Ch$ )

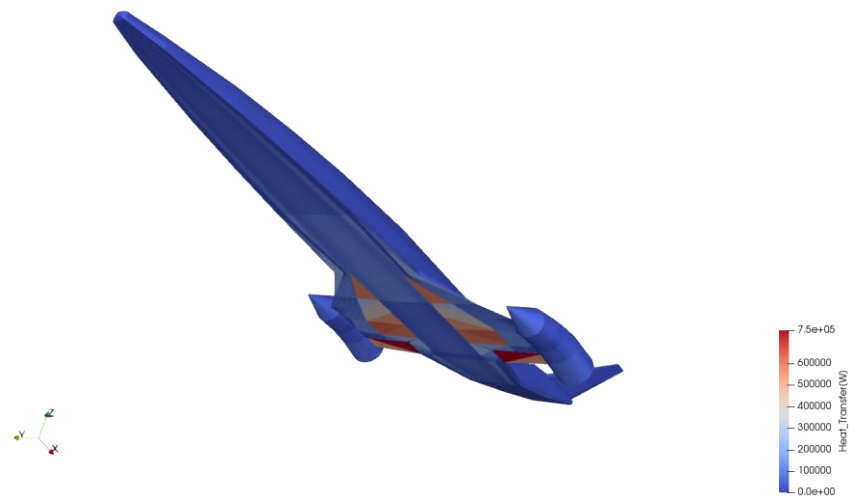


Figure 66 - CFASTT-1 Test Trajectory ( $Q$ )

## 13 Release Distribution

The code was chosen to include stable release distributions for both Windows and Linux operating systems, to satisfy the cross-platform functionality requirement.

As the code has been developed using the Microsoft Visual Studio IDE, publishing the program as an executable, contained within a relevant directory including all necessary input and output files/folders, header files and documentation. Source code has been made freely available for public access, using a file sharing repository within GitHub.

The Linux distribution has been developed through the use of the Linux subsystem in Windows 10, that gave access to a testing server for the program within the Linux environment in Visual Studio. As of March 2018, this work is as yet to be completed, but is due to be complete for the code submission in mid-April, agreed between the project team and the project stakeholders. The aim is to create a GCC compatible directory that will allow the PASTA command within the console.

## 14 Conclusions

### 14.1 Summary

The development of reusable space access vehicles, which offer fast, cheap and dependable access to space, will revolutionise global space industry.

Several high fidelity simulation methods for predicting aerodynamic and aerothermodynamic loads are currently used within the preliminary and detailed design phases of such vehicles. These methods, including DSMC and CFD, are however limited by their significant computational cost, and as such are largely impractical during preliminary design phases.

Low fidelity methods offer a reasonable simulation accuracy at a significantly reduced computational cost. For this reason, these methods offer the opportunity to significantly streamline preliminary design phases of future air-space transportation vehicles.

This report presents the development progress of PASTA 1.2, a low fidelity, local surface inclination program, based on the FOSTRAD 2.0 code developed at the University of Strathclyde.

PASTA 1.2 has been validated against high fidelity DSMC and CFD simulation data, experimental and flight test results, and additional low fidelity methods, for supersonic and hypersonic flow regimes.

PASTA 1.2 has been shown to offer a usable simulation accuracy at a computational expense of an order of magnitude reduced from DSMC and CFD methods, demonstrating the potential of PASTA 1.2 to be used within the preliminary design phase of future air-space transportation vehicles.

PASTA 1.2 has been tested against common hypersonic geometry configurations and test cases. Namely basic shapes, classical re-entry capsules and lifting body vehicles. Supersonic conditions have been tested against experimental data.

Based on the accuracy demonstrated by PASTA 1.2 compared to existing higher fidelity simulations and experimental test cases, PASTA 1.2 has been applied to a theoretical lifting body space access vehicle. This is presented as an example application of the completed program used within the concept feasibility and preliminary design phases of a future space access vehicle.

## 14.2 Discussion

While the aim of the project was to have three operational aerodynamic modules successfully implemented within the program, the code at the time of project completion will only contain supersonic and hypersonic functionality.

The supersonic module used within PASTA 1.2 contains a lower level implementation compared to the hypersonic module. This is primarily due to large amount of time required for research during the early stages of the project, including testing numerous potential formulations. Ultimately, an accurate set of results can be produced for supersonic aerodynamics of any geometry.

The implementation of a usable subsonic module within PASTA 1.2 has been unsuccessful. During the completion of the project, it was noticed that one team member would have little to present at meetings and could not answer question relating to his own progress. Attempts were made by the remaining team members to help, in the form of regular communication, up to date file sharing, research suggestions and advice. It was felt that the remaining team members provided as much help as they could, short of taking up the work themselves. This issue was brought to the stakeholder, then to higher levels of authority. It was seen that little

action could be taken, as this issue did not fully materialise until a relatively late stage of the project. In order to meet the requirements to any degree, this section of the project was reduced from the creation of code and a mathematical model to the description of methodology that could be used to eventually provide the required section. Additionally, PASTA 1.2 has been constructed to allow for the simple integration of an operational subsonics module in the future, discussed further in *section 14.3.1*.

The overall project management, including the fundamental delegation of project tasks, has been shown to be successful. Each requirement listed in *section 1.2*, with the exception of the details relating to the subsonic module, has been successfully met.

Conflicts and disagreements within the group were rare, owing to the compact nature of the project team and the potential for either a democratic solution, or a methodological approach to discussing and neutralising any issue that occurred during the completion of this project.

Time management was mostly a success, although there was a distinct rush to meet certain deadlines that could have been avoided with a more effective distribution of work throughout the duration of the project. Flexibility in the time allocated to the project week by week was a success, and meant that no other commitments were affected by the project.

Academically, the project has been a success in educating the group on software development, as well as project management techniques, more applicable to industry. The knowledge gained on programming languages will be invaluable in future occupations.

### 14.3 Future work

Despite the current demonstrated usability of PASTA 1.2 concerning the aerodynamic and aerothermodynamic simulation of space access vehicles, there exist a number of areas for improvement throughout the PASTA 1.2 code.

Little time has been spent optimising the code for computational efficiency. This was primarily due to the time constraints of the project. Future work could involve the systematic analysis of the code at the modular level, identifying bottlenecks and removing unnecessary computation.

This could be particularly useful within the Geometry module. As previously discussed, the HSR algorithms implemented within PASTA 1.2 represent the most significant resource drain of the program. Future work could involve either the improvement of the HSR implementation with respect to computational efficiency, or the complete replacement of the ray-tracing algorithm with an alternative method, such as a *rasterizing* implementation.

The code could be converted to run as a callable function, allowing the simulation to be integrated into higher level programs, such as trajectory optimisation schemes or multi-disciplinary design optimisation methods. This could be particularly useful when coupled with completely removing the HSR algorithms from the program, instead treating HSR as a separate callable function. This would allow a series of test cases (assuming no change to the geometry orientation with respect to the free stream velocity vector) to be run in a fraction of the time currently needed, as the HSR algorithm need only be run once in order to generate the HSR matrix.

It has been noted in *section 11.1* the occasional divergence of transitional regime estimations from higher fidelity simulation results for certain geometry. This will likely stem from the experimentally derived hard coded coefficient values used within the transitional bridging function. Further work could see the integration of an automatic calculation of these coefficients as a function of the specific considered geometry.

The supersonic module requires further work around the region of Mach 0.8 to 2, to ensure greater accuracy in results, as this is consistently an area with small errors, likely due to no current consideration of transonic effects. There is also no consideration of aerothermodynamic heating. It is likely the case however that the hypersonic formulation would apply to high supersonic regimes, and no thermal work is necessary for lower speeds.

### 14.3.1 Subsonic Implementation

During the course of the project, the integration of an operational subsonic module into PASTA 1.2 was not successful. In this section, an outline for how the module could be integrated in the future is discussed.

A numerical approach could be used to solve the Boundary Integral Equation outlined in *section 9.1*. The functional diagram which the code was intended to follow is shown in *figure 67*.

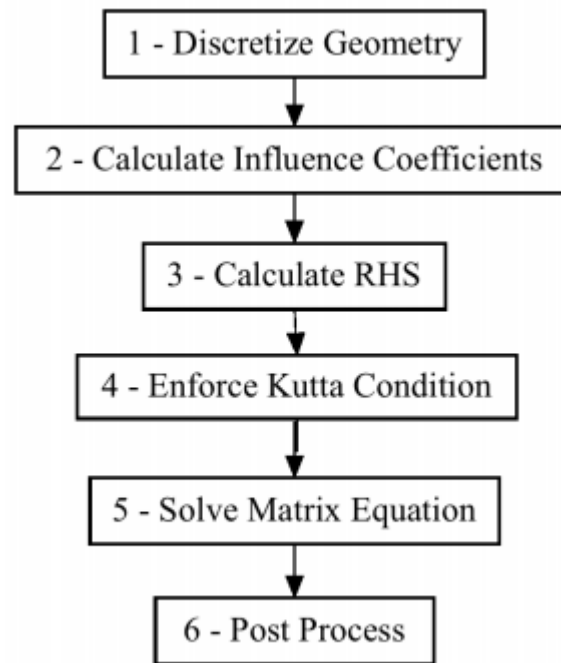


*Figure 67 – Functional Diagram for Subsonic Panel Code Implementation*

The geometry discretization will be handled by the PASTA 1.2 geometry module, detailed in *section 6*.

As described in *section 9.1*, the principle of superposition allows the BIE to be expressed as the sum of discrete singularity elements, both ‘point source’ and ‘doublet’. The influence that each of these singularity elements has on any point in the fluid domain can be expressed as an analytical function. These influences are commonly referred to as influence coefficients [23].

Satisfying the boundary conditions outlined in *section 9.1* on all the collocation points in the domain reduces the analysis problem to a system of linear algebraic equations [49].

$$A\mu - B\sigma + \phi_{\infty} = \phi_{cp} \quad (63)$$

$A$  is the doublet influence coefficient matrix:

$$A = \begin{bmatrix} a_{11} & \cdots & a_{1Pan} \\ \vdots & \ddots & \vdots \\ a_{Pan1} & \cdots & a_{PanPan} \end{bmatrix} \quad (64)$$

Where  $a$  is the influence coefficient of each doublet panel.

$B$  is the point source influence coefficient matrix;

$$B = \begin{bmatrix} b_{11} & \cdots & b_{1Pan} \\ \vdots & \ddots & \vdots \\ b_{Pan1} & \cdots & b_{PanPan} \end{bmatrix} \quad (65)$$

Where  $b$  is the influence coefficient of each point source panel.

$\mu$  (doublet) and  $\sigma$  (point source) represent the strengths of each singularity.

$$\boldsymbol{\mu} = \begin{bmatrix} \mu_1 \\ \vdots \\ \mu_{Pan} \end{bmatrix} \quad \boldsymbol{\sigma} = \begin{bmatrix} \sigma_1 \\ \vdots \\ \sigma_{Pan} \end{bmatrix} \quad (66)$$

To satisfy the Dirichlet boundary condition, the body's internal potential must be constant. By specifying that the interior potential,  $\phi_i$ , is equal to the freestream potential,  $\phi_\infty$ , the BIE is simplified. As the collocation points have been placed just interior to the body's surface, the potential at each collocation point must be equal to the free stream potential.

$$\phi_\infty = \phi_{cp} \quad (67)$$

Equation 63 can be simplified to:

$$A\boldsymbol{\mu} = B\boldsymbol{\sigma} \quad (68)$$

Each row vector in equation 68 satisfies a zero-normal flow boundary condition at each collocation point [48].

The components of the two influence coefficient matrices,  $a_{ij}$  and  $b_{ij}$ , respectively, describe the velocity potential influence at the  $i^{th}$  collocation point caused by a unit strength singularity element located at panel  $j$ .

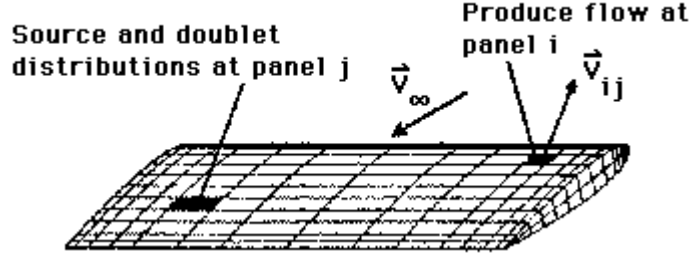


Figure 68 – Representation of the influence coefficients

In order to obtain a unique solution to *equation 68*, the problem must be reduced to determining the doublet strengths distributed over the body. As discussed in *section 9.1*, the point source singularity strengths can be described based on the free-stream velocity of the flow:

$$\sigma = n \cdot v_{\infty} \quad (69)$$

Therefore, the RHS of *equation 68* becomes:

$$RHS = \begin{bmatrix} b_{11} & \cdots & b_{1Pan} \\ \vdots & \ddots & \vdots \\ b_{Pan1} & \cdots & b_{PanPan} \end{bmatrix} \begin{bmatrix} n_{cpn} \cdot v_{\infty} \\ \cdots \\ n_{cpn} \cdot v_{\infty} \end{bmatrix} \quad (70)$$

Using this relation gives a new linear system:

$$A\mu = RHS \quad (71)$$

Which can be solved using a linear algebra technique. The choice of linear algebra technique is at the discretion of any future developer of the PASTA subsonic module.

For the integration of the singularities over the panel surfaces, there are a number of methods open to the developer. The intent for the PASTA subsonic module was to utilise constant strength singularity distributions for both the point source and doublet panels. This methodology was first described by Hess and Smith and has been used in subsonic panel codes since the mid-1960s [46]. The early methods performed each influence coefficient calculation in a panel centred reference frame before transforming it to the global reference frame. The method was reformulated by NASA, in 1987, during the development of the VSAERO panel method [65]. The updated formulation used vector product relations to avoid the computationally expensive reference frame translation.



Higher order singularity distributions were utilised in the past but are not commonly used today. The first code to utilise higher order singularity distributions was Hess II, developed in the 1980s. The second code from Hess used second order singularity distributions. At the time of development, this method offered developers more accurate results with coarser surface meshes at the cost of increase computational cost.

The automatic nature of the discretization process in modern engineering applications has reduced the need for higher order singularity distributions. Increased accuracy in modelling the flow can now be found by increasing the mesh density on the surface of the body. This allows for the constant strength singularity method, and the desirable computational simplicity it offers, to yield accurate results even when analysing 3D bodies [45].

Similarly, to the integration of the singularity elements, there are a number of methods available to the developer when enforcing the Kutta condition in the code. The method planned for use in the PASTA subsonic module, involved modelling the wake as doublet panels extending infinitely downstream from the trailing edge of the body (*figure 69*).

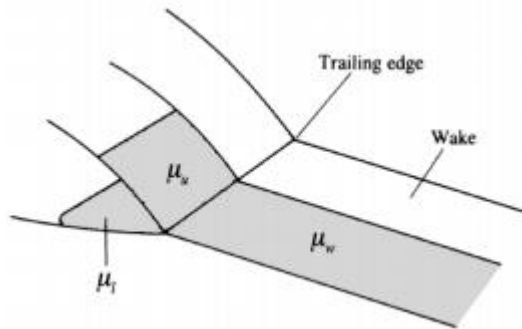


*Figure 69 – Doublet wake sheet for enforcement of Kutta condition*

Enforcement of the Kutta condition is achieved by transferring the difference in vorticity between the top and bottom panels to the wake panel [49]:

$$\mu_w = \mu_U - \mu_L \quad (72)$$

Satisfying this equation ensures that the vorticity at the trailing edge, which is the shared edge between the three panels, is equal to zero and thus the stagnation point is held at the trailing edge.

The post processing begins with the calculation of the velocity field. The velocity field is calculated by computing the surface derivative of the potential field which is distributed across the analysis surface. Early panel codes utilised a finite difference method to evaluate the derivative, this transferred to the viscous core method in the early 1990's with the development of PMARC and FPA [66] [67]. The intent for the PASTA subsonic module was to implement a constrained Hermite Taylor series least squares (CHTLS) method for calculating the derivatives. This method was successfully implemented in CPanel from California Polytechnic and was shown to reduce the nonphysical velocity influences which effect the accuracy of codes which use the viscous core method [45].

Knowing the local velocity at each panel on the analysis system, the pressure field can be formed by calculating the pressure coefficient on each  $i^{th}$  panel:

$$C_{pi} = \frac{p_i - p_\infty}{0.5(\rho_\infty v_\infty^2)} \quad (73)$$

From the pressure coefficient, each panel's force coefficient can be found:

$$C_{fi} = \frac{-C_{pi} A_i \mathbf{n}_i}{S_{ref}} \quad (74)$$

The total force coefficient for the entire body can then be found by summing the individual coefficient contributions across the entire analysis surface. The lift and drag coefficients are then calculated from the overall force coefficient via the body to wind coordinate transfer matrix defined within the main PASTA code.

## 15 References

- [1] R. Belbin, "Management Teams - Why they succeed or fail," London, Heinemann, 1981, pp. 88-90.
- [2] Association of Project Managers, "Introduction to Risk management," 2017. [Online]. Available: <https://www.apm.org.uk/body-of-knowledge/delivery/risk-management/>. [Accessed 19 March 2018].
- [3] E. Sanger and J. Bredt, "A Rocket Drive for Long Range Bombers," Technical Information Branch, Baur Navy Department, 1944.
- [4] M. Dobson, "An Historical and Applied Aerodynamic Study of the Wright Brothers Wind Tunnel Test Program and Application to Successful Manned Flight," USNA, 2005.
- [5] J. Anderson, Hypersonic and High Temperature Gas Dynamics 2nd Edition, AIAA, 2006.
- [6] G. Bird, "Molecular Gas Dynamics and the Direct Simulation of Gas Flows," Oxford Engineering Science Publications, 1994.
- [7] W. Wagner, "A Convergence Proof for Bird's Direct Simulation Monte Carlo Method for the Boltzmann Equation," *Journal of Statistical Physics*, vol. 66, 1992.
- [8] C. J. Roy, M. Gallis, T. Bartel and J. Payne, "Navier-Stokes and Direct Simulation Monte Carlo Predictions for Laminar Hypersonic Separation," *AIAA Journal*, vol. 41, no. 6, 2003.
- [9] M. Gallis, J. Torczynski, S. Plimpton and T. Koehler, "Direct Simulation Monte Carlo: The quest for speed," in *Proceedings of the 29th International symposium on rarefied gas dynamics*, 2014.
- [10] T. Schwartzentruber, L. Scalabrin and I. Boyd, "A Modular Particle-Continuum Numerical Method for Hypersonic Non-Equilibrium Gas Flows," *Journal of Computational Physics*, vol. 225, pp. 1159 - 1174, 2007.
- [11] S. Pantazis, "Hybrid continuum-particle simulations for vacuum flows," 2012.
- [12] L. Lees, "Hypersonic Flow," *Journal of Spacecraft and Rockets*, vol. 40, no. 5, pp. 241 - 276, 1955.
- [13] J. Dobarco-Otero, R. Smith, K. Bledsoe, R. DeLaune, W. Rochelle and L. Johnson, "The Object Re-Entry Survival Analysis Tool (ORSAT) - Version 6.0 and its Application to Spacecraft Entry".
- [14] T. Lips and B. Fritsche, "A comparison of commonly used re-entry analysis tools," *Acta Astronautica*, vol. 57, pp. 312 - 323, 2005.
- [15] H. K. Cheng, "Hypersonic shock-layer theory of the stagnation region at low Reynolds number," Cornell Aeronautical Laboratory, 1961.
- [16] L. O. Cropp, "Analytical methods used in predicting the reentry ablation of spherical and cylindrical bodies," Sandia Corporation, 1965.
- [17] G. Koppenwallner, B. Fritsche, T. Lips and H. Klinkrad, "SCARAB - A Multi-Disciplinary Code for Destruction Analysis of Spacecraft during Re-entry," in *Proceedings of the 5th European Symposium on Aerothermodynamics for Space Vehicles*, Cologne, Germany, 2005.

- [18] N. Kogan, "Rarefied Gas Dynamics Plenum Press," New York, 1969.
- [19] P. M. Mehta, E. Minisci, M. Vasile, A. C. Walker and M. Brown, "An Open source Hypersonic Aerodynamic and Aerothermodynamic Modeling Tool," 2015.
- [20] M. Baud, "Data Analysis, Mathematical Modeling," *Methods of Immunological Analysis*, vol. 1, pp. 656-671, 1993.
- [21] G. Benedetti, "Low-fidelity modelling for aerothermal characteristics of reentry objects," Glasgow, 2016.
- [22] M. Drela, "XFOIL: An analysis and design system for low Reynolds number airfoils.," in *Low Reynolds number aerodynamics*, Notre Dame, 1989.
- [23] D. Filkovic, "GRADUATE WORK," University of Zagreb, Zagreb, 2008.
- [24] L. Prechelt, "An empirical comparison of c, c++, java, perl, python, rexx and tcl," *IEEE Computer*, vol. 30, no. 10, pp. 23-29, 2000.
- [25] A. Lofthouse, "Nonequilibrium Hypersonic Aerothermodynamics using the Direct Simulation Monte Carlo and Navier-Stokes Models," University of Michigan, 2008.
- [26] NASA, "U.S. Standard Atmosphere 1976," NASA, Washington DC, 1976.
- [27] AIAA, "Guide to Reference and Standard Atmosphere Models," AIAA, 2010.
- [28] J. M. Picone, A. E. Hedin, D. P. Drob and A. C. Aikin, "NRLMSISE-00 empirical model of the atmosphere: Statistical comparisons and scientific issues," *Journal of Geophysical Research*, vol. 107, 2002.
- [29] W. Kahan, "Miscalculating Area and Angles of a Needle-like Triangle," University of California, Berkeley , 2014.
- [30] P. Mehta, G. Blanco Arnao, M. Bonetti and M. Vasile, "Computer Graphics for Space Debris," in *6th International Conference on Astrodynamics Tools and Techniques (ICATT)*, Darmstadt, 2016.
- [31] J. Moss and G. Bird, "Direct Simulation of Transitional Flow for Hypersonic Reentry Conditions," in *AIAA 22nd Aerospace Sciences Meeting*, Reno, Nevada, 1984.
- [32] W. Hayes and R. Probstein, "Free Molecular Transfer Theory," in *Applied mathematics and Mechanics*, New York, 1959, pp. 395 - 403.
- [33] S. Schaaf and P. Chambre, "Flow of Rarefied Gases," in *High Speed Aerodynamics and Jet Propulsion*, Princeton, NJ, Princeton University Press, 1958, pp. 1-55.
- [34] N. Kemp, P. Rose and R. Detra, "Laminar heat transfer around blunt bodies in dissociated air," *Journal of the Aerospace Sciences*, pp. 421-430, 1959.
- [35] J. Merrifield, J. Beck, G. Markelov, P. Leyland and R. Molina, "Aerothermal Heating Methodology in the Spacecraft Aerothermal Modeling (SAM)," 2014.
- [36] J. Merrifield, J. Beck, A. Pagan, G. J. Herdrich, O. Chazot and B. Bonvoisin, "Impact of Surface Catalcity on Demisability of Metallic Materials," in *Final Stardust Conference*, ESA, Noordwijk, The Netherlands, 2016.
- [37] A. Falchi, E. Minisci, M. Vasile, D. Rastelli and N. Bellini, "DSMC based correction factor for low fidelity hypersonic aerodynamics of re-entering objects and space debris," in *7th European Conference for Aeronautics and Aerospace Sciences (EUCASS)*, 2017.

- [38] R. W. Detra, N. H. Kemp and F. R. Riddell, "Addendum to Heat Transfer to Satellite Vehicles Reentering the Atmosphere," *Jet Propulsion*, vol. 27, no. 12, pp. 1256-1257, 1957.
- [39] Public Domain Aeronautical Software, "Computing the Wave Angle of an Attached Shock Wave," Public Domain Aeronautical Software, 9 July 2002. [Online]. Available: <http://www.pdas.com/oshock2.xml>. [Accessed 17 March 2018].
- [40] J. D. Anderson Jr, *Fundamentals of Aerodynamics*, McGraw-Hill, 1991.
- [41] H.-S. Dou and H.-Y. Teng, "Approximate Formula of Weak Oblique Shock Wave Angle," *AIAA Journal*, vol. 30, no. 3, pp. 837-839, 1992.
- [42] C. I. Criz and G. J. Sova, "Improved tangent-cone method for the Aerodynamic Preliminary Analysis System (APAS) version of the hypersonic arbitrary-body program," NASA, Langley, 1990.
- [43] C. I. Cruz and G. J. Sova, "Improved Tangent-Cone Method for the Aerodynamic Preliminary Analysis System (APAS) Version of the Hypersonic Arbitrary-Body Program," NASA, Hampton, 1990.
- [44] M. A. Epton and A. E. Magnus, "PAN AIR - Predicting Subsonic Or Supersonic Linear Potential Flows About Arbitrary Configurations Using A Higher Order Panel Method," 1990.
- [45] C. R. Satterwhite, "DEVELOPMENT OF CPANEL, AN UNSTRUCTURED PANEL CODE," California Polytechnic State University, 2015.
- [46] Virginia Tech, "[http://www.dept.aoe.vt.edu/~mason/Mason\\_f/CAtxtChap4.pdf](http://www.dept.aoe.vt.edu/~mason/Mason_f/CAtxtChap4.pdf)," [Online]. Available: [http://www.dept.aoe.vt.edu/~mason/Mason\\_f/CAtxtChap4.pdf](http://www.dept.aoe.vt.edu/~mason/Mason_f/CAtxtChap4.pdf). [Accessed Jan 2018].
- [47] L. L. Erikson, "Panel Methods - An Introduction," NASA, 1990.
- [48] A. Ramos, "DEVELOPMENT OF A MESHLESS METHOD TO SOLVE COMPRESSIBLE POTENTIAL FLOWS," California Polytechnic State University, 2010.
- [49] J. Katz and A. Plotkin, *Low-Speed Aerodynamics*, 2001.
- [50] H. Lamb, *Hydrodynamics*, Cambridge University Press, 1895.
- [51] A. Kuethe and J. Schetzer, *Foundations of Aerodynamics*, 1959.
- [52] "Paraview," [Online]. Available: <https://www.paraview.org/>.
- [53] V. Dogra, R. Wilmoth and J. Moss, "Aerothermodynamics of a 1.6-meter diameter Sphere in Hypersonic Rarefied Flow," *AIAA Journal*, 1992.
- [54] NASA, "What is Orion?," 25 March 2015. [Online]. Available: <https://www.nasa.gov/audience/forstudents/5-8/features/nasa-knows/what-is-orion-58.html>. [Accessed March 2018].
- [55] J. Burns, D. Kring, J. Hopkins, S. Norris, W. Lazio and J. Kasper, "A lunar L2-farside exploration and science mission concept with the orion multi-purpose crew vehicle and a teleoperated lander/rover," *Advances in Space Research*, vol. 52, pp. 306-320, 2013.
- [56] J. Moss, B. Katie and F. Greene, "Orion Aerodynamics for Hypersonic Free Molecular to Continuum Conditions," in *14th AIAA/AHI International Space Planes and Hypersonic Systems and Technologies Conference*, Canberra, Australia, 2006.

- [57] T. Sharp, "Space Shuttle: The First Reusable Spacecraft," 11 December 2017. [Online]. Available: <https://www.space.com/16726-space-shuttle.html>. [Accessed March 2018].
- [58] D. Rault, "Aerodynamics of the Shuttle Orbiter at High Altitudes," *Journal of Spacecraft and Rockets*, vol. 36, no. 6, 1994.
- [59] R. Blanchard and E. Hinson, "Rarefied Pitching Moment Coefficient Measurements of the Shuttle Orbiter," *ICAS*, 1988.
- [60] R. C. Blanchard, "Rarefied Flow Lift-To-Drag Measurements of the Shuttle Orbiter," NASA Langley Research Centre, Hampton, Virginia, 1986.
- [61] J. Moss and G. Bird, "Direct Simulation of Transitional Flow for Hypersonic Reentry Conditions," *AIAA*, 1984.
- [62] L. M. Spearman and D. O. Braswell, "Aerodynamics of a sphere and an oblate spheroid for Mach numbers from 0.6 to 10.5 including some effects of test conditions," NASA, Hampton, 1993.
- [63] R. Wuilbereq, "Multi-Disciplinary Modeling of Future Space Access Vehicles," University of Strathclyde, Glasgow, 2015.
- [64] F. Toso, A. Riccardi, E. Minisci and C. Maddock, "Optimisation of Ascent and Descent Trajectories for Lifting Body Space Access Vehicles," in *66th International Astronautical Congress*, Jerusalem, Israel, 2015.
- [65] NASA, "VSAERO User Manual," 1982.
- [66] D. L. Ashby, M. R. Dudley, I. K. Steve, L. Brwone and J. Katz, "Potential Flow Theory and Operation Guide for the Panel Code PMARC," 1991.
- [67] Continuum Dynamics, "Fast Panel Methods for Configurational Aerodynamic," [Online]. Available: <http://continuum-dynamics.com/lib-pro-fpa.html>. [Accessed Feb 2018].
- [68] J. A. Fay and F. R. Riddell, "Theory of Stagnation Point Heat Transfer in Dissociated Air," *Journal of the Aeronautical Sciences*, vol. 25, no. 2, pp. 73-85, 1958.
- [69] H. Legge, "Hypersonic approximations for heat transfer and shear stress applied to continuum and rarefied plume impingement," 1987.
- [70] E. R. Van Driest, "The Problem of Aerodynamic Heating," *Aero. Eng. Rev.*, vol. 15, no. 10, pp. 26-41, 1956.